

The space charge effects on the intra-bunch motion under large chromaticity at the Main Ring in the Japan Proton Accelerator Research Complex

Nobuyuki Yoshimura,^{1,*} Takeshi Toyama,² and Yoshihiro Shobuda²

¹*Department of Physics, Kyoto University, Kyoto 606-8502, Japan*

²*J-PARC Center, JAEA & KEK, 2-4 Shirakata, Tokaimura, Nakagun, Ibaraki 319-1195, Japan*

In general, optimizing chromaticity and transverse feedback parameters is important in suppressing beam instabilities for stable operation in high-intensity proton machines. Meanwhile, space charge effects impact the intra-bunch motion of the proton bunch within a large chromaticity region in the machines, such as the Main Ring (MR) in the Japan Proton Accelerator Research Complex (J-PARC). To address this issue, the decoherence and recoherence of the transverse motion of the particles comprising the proton bunch are investigated. The analysis reveals that the space charge effects have a significant influence on the recoherence period through the chromaticity. Nevertheless, the relationship between the maximum frequency and the chromaticity is not affected by the space charge effects. These findings are demonstrated with particle tracking simulations including the direct, indirect-space charge effects and the impedance source of the J-PARC MR.

I. INTRODUCTION

High-intensity proton beams are essential for a wide range of experiments, from high-energy physics to life and material sciences. Notable examples include CERN Super Proton Synchrotron (SPS), Fermilab Main Injector (MI), and Alternating Gradient Synchrotron (AGS) at Brookhaven National Laboratory (BNL), which have all been instrumental in advancing high-energy physics research. These facilities produce high-intensity proton beams for experiments in neutrino physics, high-energy physics, and hadron collider experiments.

The Japan Proton Accelerator Research Complex (J-PARC) Main Ring (MR) synchrotron [1–6] stands out as a leader in neutrino physics research and is essential for the development of the T2K experiment [7–10] and the future Hyper-Kamiokande experiment [11]. The high-intensity proton beam and the stable operation of the J-PARC MR contribute to increasing the statistics and improving the accuracy of measurements of neutrino oscillation parameters. The operational average beam power of the J-PARC MR is approximately 800 kW as of 2024 under the number of protons per pulse (ppp) of 2.3×10^{14} with 8 bunches, a MR cycle of 1.36 s, and an extraction energy of 30 GeV.

To further improve the performance of the accelerator toward an intensity frontier, it is important to manipulate the intra-bunch motions of the beam adequately. While enlarging chromaticity is a standard method to suppress beam instabilities, head-tail modes [12–14] could be excited by the impedances due to wakefields in the ring. An upgrade of the transverse intra-bunch feedback (IBFB) [15–25] is currently underway to achieve operation at 1.3 MW. This paper aims to clarify the behavior of head-tail modes with the high-intensity beams caused by the combined effects of the chromaticity, impedance, and space charge to achieve stable operation.

One pioneering work was done to investigate the effects of the intra-bunch motion in SIS-18 at GSI Darmstadt [26–32]. However, the parameter region they explored is quite restricted, because the chromatic phase χ_b defined as

$$\chi_b = 2\pi \frac{\xi}{\eta C} z_b, \quad (1)$$

is lower than 5, where $\xi = \Delta\nu_\beta/\Delta\delta$ is the chromaticity, z_b is the full bunch length, η is the slippage factor, and C is the circumference of the ring, ν_β is the bare betatron tune, and δ is the longitudinal momentum deviation. Among the head-tail modes excited by the transverse bunch displacement during the injection process, the only lower modes $m \leq 3$ survive after the injection. Furthermore, the space charge parameter q_{sc} [26–30] defined as

$$q_{sc} = \frac{|\Delta\nu_{inc}|}{\nu_s}, \quad (2)$$

with the incoherent tune shift from the direct space charge $\Delta\nu_{inc}$ and the synchrotron tune ν_s , is lower than 10.

For machines aiming for higher intensities, such as the MR, more extensive work is indispensable because the chromatic phase χ_b could change in wider regions to around 50 to suppress the beam instabilities, and the space

* yoshimura.nobuyuki.76w@st.kyoto-u.ac.jp

charge parameter q_{sc} could become higher than 50. Then we present a more comprehensive study of the effects of space charge on particle motion within the bunch across the wider parameter range, using theoretical analysis, simulations, and experimental measurements at the MR.

We also estimate the effect of longitudinal and transverse impedances on the intra-bunch motion in the MR. In the process, we establish a framework for incorporating the long-range resistive wall impedance into simulation codes by accounting for the chamber thickness. Finally, we demonstrate that the impedance do not influence intra-bunch motion both theoretically and simulationally unless the beam instability occurs.

The primary objective of this study is to understand the fundamental aspects of the intra-bunch motion under large chromaticity in high-intensity proton rings. Specifically, we explore the impact of direct and indirect space charge effects on the head-tail modes through the chromaticity within the wider parameter region when no beam instability is present by choosing suitable machine parameters.

To gain deeper insight into the complex factors of intra-bunch dynamics, reconciling simulation and experimental results is essential. However, full 3-dimensional simulations are often impractical as a primary approach due to their time-consuming and overly complex nature. To address this issue, we have originally developed a simplified particle tracking simulation code that models the time evolution of transverse dipole moments and space charge effects. This code tracks particles in two dimensions —horizontal and longitudinal— using a linear approximation. This simplification enables us to better understand the combined effects of head-tail modes, chromaticity, and space charge.

To validate this code, we provide a robust foundation for handling direct and indirect space charge effects from a fundamental perspective. During this derivation process, we clarify the limits of the theory's applicability to the direct and indirect space charge effects within the linear approximation. For a benchmark test, the simulation results are compared with theoretical predictions addressing Gaussian beams in a harmonic potential with weak space charge forces, extended from the airbag square-well (ABS) model originally developed by Blaskiewicz [14]. Ultimately, we demonstrate that the simplified simulation tools are valuable for characterizing and understanding experimental measurements dealing with the high-intensity beams.

This paper is structured as follows: In Sec. II, we introduce the basics of the algorithm without space charge effects. In Sec. III, we review the theoretical decoherence model without space charge to understand the characteristics of intra-bunch motion. In Sec. IV, we establish a robust foundation for incorporating space charge effects into the code. In Sec. V, we address the transverse resistive wall impedance. In Sec. VI, we partially generalize the ABS theoretical model to account for Gaussian beams in a harmonic potential, incorporating both weak direct and indirect space charge effects. In Sec. VII, we provide a comprehensive analysis of intra-bunch motion by comparing the simulation with the theoretical results. In Sec. VIII, we examine the effects of space charge on intra-bunch motion through chromaticity and RF voltage in the time domain in preparation for comparison with the experimental measurements. In Sec. IX, the measured data are analyzed and compared with the simulation results. Finally, the paper is summarized in Sec. X.

II. BASIC ALGORITHM

In this section, let us focus solely on implementing basic kinematics into our code, neglecting the space charge and wakefield effects. To simplify the situation, the simulation only deals with 1D transverse (horizontal) + 1D longitudinal motion, by tracking macroparticle motions in discrete time steps. In this paper, only the storage mode, not the acceleration mode, from the injection period is considered to highlight the feature of the space charge effect on the intra-bunch motion in the following sections after generalizing this algorithm.

The horizontal coordinates x is defined as the position relative to that of the synchronous particle, and $x' = dx/ds$ is the derivative of x with respect to s , path length along the design trajectory. The horizontal motion terms are calculated as

$$x_{n+1,i} = \cos(\phi_{n,i})x_{n,i} + \beta_x \sin(\phi_{n,i})x'_{n,i}, \quad (3)$$

$$x'_{n+1,i} = -\frac{1}{\beta_x} \sin(\phi_{n,i})x_{n,i} + \cos(\phi_{n,i})x'_{n,i}, \quad (4)$$

where i is the macroparticle number index, n is the simulation step number index, $x_{n,i}$ is the horizontal position, $x'_{n,i}$ is the horizontal position derivative with respect to $s = \beta c \hat{T}_n$, \hat{T}_n is the n -th time, the betatron phase advance is

$$\phi_{n,i} = 2\pi (\nu_\beta + \xi \delta_{n,i}) \frac{\Delta T}{T_0}, \quad (5)$$

$\Delta T = \hat{T}_{n+1} - \hat{T}_n$, $\delta_{n,i}$ is the longitudinal momentum derivative from the synchronous particle, the bare betatron tune $\nu_\beta = 21.35$, the circumference $C = 1567.5$ m, the slippage factor $\eta = -0.0578$ for a total energy $E_0 = 3.938$ GeV with Lorentz- $\beta = 0.971$ and Lorentz- $\gamma = 4.198$, the revolution period $T_0 = C/\beta c = 5.384$ μs , and $\beta_x = C/2\pi\nu_\beta$ is the average value of the beta function along the MR.

For the transverse phase space distribution, we adopt a Gaussian distribution with $\sigma_x = 7.5$ mm and $\sigma_{x'} = 0.64$ mrad as its initial condition. The condition for this simulation reflects the condition of the MR because the beams injected into the ring typically have an unnormalized rms emittance of $\epsilon_x = 4.8\pi$ mm mrad. The horizontal offset position at injection is $X_0 = 0.01$ m.

The longitudinal coordinates z and δ are defined as the position and the momentum deviation relative to those of the synchronous particle, respectively. The longitudinal motion terms are calculated as

$$z_{n+1,i} = z_{n,i} - \eta C \delta_{n,i} \frac{\Delta T}{T_0}, \quad (6)$$

$$\delta_{n+1,i} = \delta_{n,i} - \frac{eV_{\text{RF}}}{\beta^2 E_0} \frac{2\pi h}{C} z_{n+1,i} \frac{\Delta T}{T_0}, \quad (7)$$

where $z_{n,i}$ is the longitudinal position, the electric charge $e = 1.6 \times 10^{-19}$ C, and the harmonic number $h = 9$. Unless otherwise specified, the RF voltage is $V_{\text{RF}} = 263$ kV in this paper.

The small-amplitude bare synchrotron tune ν_s is given by

$$\nu_s = \sqrt{\frac{eV_{\text{RF}} h |\eta|}{2\pi \beta^2 E_0}}, \quad (8)$$

which is 0.0024 by the given parameters. The synchrotron period is defined as $N_s = 1/\nu_s (= 410)$.

For the longitudinal phase space distribution, we adopt a Gaussian distribution with $\sigma_z = 10$ m and

$$\sigma_\delta = \frac{2\pi\nu_s}{|\eta|C} \sigma_z, \quad (9)$$

as its initial condition.

In this paper, the bunching factor is defined as

$$B_f = \frac{eN_B}{C\hat{\lambda}}, \quad (10)$$

where N_B is the bunch population, $\hat{\lambda}$ is the peak line density of electrical charges, featuring $B_f = 0.015$ in this simulation.

Particularly under the square-well potential in the airbag model (ABS model), which is used for the theoretical analysis in the following sections, Eq. (7) is replaced by

$$\delta_{n+1,i} = \begin{cases} \delta_{n,i}, & \text{for } -\hat{z} \leq z_{n+1,i} \leq \hat{z}, \\ -\delta_{n,i}, & \text{for } z_{n+1,i} < -\hat{z}, \hat{z} < z_{n+1,i}, \end{cases} \quad (11)$$

to ensure the consistent longitudinal motion with the momentum deviation at a constant velocity in the region of $-\hat{z} < z < \hat{z}$ (\hat{z} is the half bunch length). We set $\hat{z} = \sqrt{\pi/2}\sigma_z = 12.5$ m to match the peak density of the uniform distribution and that of the Gaussian distribution for the same bunch intensity eN_B , and the momentum is distributed as $\delta = \pm\delta_0 = \pm 0.13\%$ to satisfy

$$\delta_0 = \frac{4\nu_s}{|\eta|C} \hat{z}, \quad (12)$$

to guarantee the same synchrotron period as that of the harmonic potential.

The transverse centroid of the entire bunch \bar{x}_n is defined as

$$\bar{x}_n = \frac{1}{N_{\text{particle}}} \sum_i x_{n,i}, \quad (13)$$

where N_{particle} is the number of macroparticles in the bunch.

Subsequently, let us divide the ring with the segment length σ_Δ where k -th segment is identified with $z^{(k)} = -C/2h + k\sigma_\Delta$ in the interval $[-C/2h, C/2h]$, and investigate the intra-bunch frequency by calculating the dipole moment $\Delta^{(k)}$ and the charge density $\lambda^{(k)}$ for the k -th segment when the segment is filled with macroparticles comprising the bunch. The number of macroparticles $N^{(k)}$ in k -th segment is calculated as

$$N^{(k)} = \sum_i S_i^{(k)}, \quad (14)$$

where (k) and i specify the segment and macroparticle indices, respectively, and the shape function is introduced as follows [33, 34]

$$S_i^{(k)} = \begin{cases} 1 - \frac{|z_i - z^{(k)}|}{\sigma_\Delta}, & \text{for } z^{(k-1)} \leq z_i \leq z^{(k+1)}, \\ 0, & \text{for } z_i < z^{(k-1)}, z^{(k+1)} < z_i. \end{cases} \quad (15)$$

Finally, the dipole moment $\Delta^{(k)}$ and the charge density $\lambda^{(k)}$ of k -th segment are respectively described as

$$\Delta^{(k)} = \frac{q}{\sigma_\Delta} \sum_i x_i S_i^{(k)}, \quad (16)$$

$$\lambda^{(k)} = \frac{q}{\sigma_\Delta} \sum_i S_i^{(k)}, \quad (17)$$

with $q = eN_B/N_{\text{particle}}$ being the allocated charge for one macroparticle. Accordingly, the transverse centroid $x^{(k)}$ of k -th segment is given by

$$x^{(k)} = \frac{\Delta^{(k)}}{\lambda^{(k)}}. \quad (18)$$

In the following simulations concerning the transverse oscillation in the bunch, we will conduct tracking simulations with both the ABS model with Eqs. (6) and (11), and the harmonic potential bunch model with Eqs. (6) and (7). The horizontal chamber boundary is set to ± 0.065 m, while the longitudinal bucket size is $\pm C/2h$. We assume that any macroparticles outside this region should be lost.

III. TRANSVERSE LINEAR DECOHERENCE

In this section, to overview a typical behavior of intra-bunch motion, we review the linear decoherence model [30, 35], neglecting the space charge and wakefield effects, and assuming the tune shift is solely caused by the chromaticity. The longitudinal and transverse motions of particles within a bunch are correlated through the synchrotron motion. To explore how the chromaticity affects the motions of the particles comprising the bunch, we examine a situation where the particles with identical initial transverse offsets is injected into the ring, exciting the intra-bunch motions. In general, the disappearance of the coherent oscillation signal, observed as the beam circulates the ring, reflects the betatron phase spread caused by the chromaticity, (space charge, and wake effects).

The intra-bunch oscillation describes the behavior of the transverse centroid at the respective longitudinal position along the bunch for a specific turn in the ring, which is closely related to the decoherence signals of the bunch. The Fourier transform of this centroid position with respect to the longitudinal direction yields a frequency spectrum in the bunch. When this frequency spectrum becomes pronounced, it manifests the instability of the beam. Proper identification and analysis of intra-bunch oscillations are essential for determining the performance of the IBFB because it functions by detecting the frequency signals.

Following this model, we examine the transverse centroid $\bar{x}(n, z)$ for a group of particles with the same longitudinal position z in a given turn n . The initial condition is set as $\bar{x}(n=0, z) = X_0$ regardless of the longitudinal position of the particles, with an initial betatron phase of $\phi(n=0, z) = 0$. Assuming a Gaussian distribution ($\sigma_\delta = 2\pi\nu_s/|\eta|C \times \sigma_z$: Eq. (9)) in the synchrotron phase space, the transverse centroid $\bar{x}(n, z)$ for the respective parts of the bunch is calculated as (refer to Appendix A) [26]

$$\bar{x}(n, z) = X_0 \exp \left[-\frac{1}{2} \chi_\sigma^2 \sin^2(2\pi\nu_s n) \right] \exp \left[-\mathbf{i}(2\pi\nu_\beta n - 2\chi_\sigma \sin^2(\pi\nu_s n) \frac{z}{\sigma_z}) \right], \quad (19)$$

where \mathbf{i} is the imaginary unit, and the rms chromatic phase χ_σ for the bunched beam is defined as

$$\chi_\sigma = 2\pi \frac{\xi}{\eta C} \sigma_z = \frac{|\xi|}{\nu_s} \sigma_\delta. \quad (20)$$

Since the envelope amplitude term is $X_0 \exp(-\chi_\sigma^2 \sin^2(2\pi\nu_s n)/2)$ in Eq. (19), it is approximated as $X_0 \exp(-2(\pi\chi_\sigma\nu_s)^2 (n - mN_s/2)^2)$ up to the second order after expanded around $n = mN_s/2$ (m is an integer), regardless of the longitudinal positions z in the bunch. In other words, the higher the absolute chromaticity, the sharper the recoherence signals.

Since the intra-bunch frequency $f_{\text{int}}(n)$ can be interpreted as the betatron phase advance within the bunch per unit time, it can be defined as

$$\begin{aligned} f_{\text{int}}(n) &= \left| \frac{1}{2\pi} \frac{d}{dt} \left[2\pi\nu_\beta n - 4\pi \frac{\xi}{\eta C} z \sin^2(\pi\nu_s n) \right] \right| \\ &= \left| 2 \frac{\xi}{\eta C} \frac{dz}{dt} \sin^2(\pi\nu_s n) \right| \\ &= \left| 2f_0 \frac{\xi}{\eta} \sin^2(\pi\nu_s n) \right|, \end{aligned} \quad (21)$$

by recognizing the exponential factor in Eq. (19), where $f_0 = 1/T_0$ is the revolution frequency. The maximum value of $f_{\text{int}}(n)$ at the specified longitudinal position z in the bunch is given by

$$f_{\text{max}} = f_{\text{int}} \left(\frac{N_s}{2} \right) = \left| 2f_0 \frac{\xi}{\eta} \right|. \quad (22)$$

The intra-bunch frequency is proportional to ξ and independent of z in the linear decoherence model, which means any portion of the beam can oscillate at the maximum intra-bunch frequency f_{max} . Moreover, the maximum intra-bunch frequency is remarkably enhanced by increasing the chromaticity.

The transverse centroid of the entire bunch $X(n)$ is calculated by convolving Eq. (19) with a Gaussian distribution :

$$\rho_z(z) = \frac{1}{\sqrt{2\pi}\sigma_z} \exp\left(-\frac{z^2}{2\sigma_z^2}\right), \quad (23)$$

resulting in [35]

$$X(n) = X_0 \exp(-2\chi_\sigma^2 \sin^2(\pi\nu_s n)) \exp(-\mathbf{i}2\pi\nu_\beta n). \quad (24)$$

Thus, the amplitude of this betatron oscillation follows

$$A(n) = X_0 \exp(-2\chi_\sigma^2 \sin^2(\pi\nu_s n)). \quad (25)$$

As the chromaticity increases, the betatron phase spread widens through the chromatic phase, demonstrating that the transverse centroid amplitude decreases. That is the decoherence of particles comprising the bunch. However, after a synchrotron period from injection, $f_{\text{int}}(N_s) = 0$, the recoherence of particles emerges because of $A(N_s) = X_0$. It is noticeable that this recoherence phenomenon occurs with the synchrotron period only when the effect of the chromaticity is taken into consideration.

Similarly to Eq. (19), let us expand Eq. (25) around $n = mN_s$ (where m is an integer), resulting in $A(n) \simeq X_0 \exp(-2(\pi\chi_\sigma\nu_s)^2 (n - mN_s)^2)$ up to second order. The higher the absolute chromaticity, the sharper the recoherence signals. It is important to note that the period of the recoherence time for the entire bunch is N_s , although the dipole moments of the particles comprising the bunch align to create sharp signals with a period of $N_s/2$, as referenced in Eq. (19).

IV. FORMULATION OF THE SPACE CHARGE EFFECT

To investigate the space charge effects on the intra-bunch motion, this section formulates the effects, which are implemented into our tracking simulation, based on the Poisson equation. In this context, we will directly observe the direct and indirect space charge effects characterized by the incoherent tune shift $\Delta\nu_{\text{inc}}$ and coherent tune shift $\Delta\nu_{\text{coh}}$,

respectively, within the linear approximation, although most papers assume this characteristic without specifying any particular conditions required. We will find that this linear approximation helps manage the space charge effects efficiently when the transverse beam size is sufficiently smaller than the chamber radius.

In the case of a proton bunch like the MR, since the longitudinal bunch length is much larger than the transverse beam size, we simplify the three-dimensional beam to the two-dimensional one by slicing the beam perpendicularly to the longitudinal direction before treating the respective segments independently. This approach not only streamlines the computational process but also allows us to effectively capture the transverse dynamics of the bunch. Within each segment, we assume that the beam is represented with a charge line density $\lambda(z)$ in the longitudinal direction and a uniform-density elliptical beam on the transverse plane, following the Kapchinski-Vladimirskij (K-V) distribution [36]. We will proceed by separately addressing the elliptical chamber in open space and the one placed inside the bending magnet, simplified by parallel magnetic pole faces.

First, we consider the case of two-dimensional beam passing through the elliptical chamber in open space. Let us define the region I occupied by the beam on the transverse plane as

$$I(x, y) = \begin{cases} 1, & \text{for } D(x, y, \bar{x}) \leq 1, \\ 0, & \text{for } D(x, y, \bar{x}) > 1, \end{cases} \quad (26)$$

where

$$D(x, y, \bar{x}) = \frac{(x - \bar{x})^2}{a_x^2} + \frac{y^2}{a_y^2}, \quad (27)$$

\bar{x} is the horizontal centroid of each segment in the beam, a_x and a_y are the horizontal and vertical beam sizes, respectively.

The charge line density $\bar{\lambda}$ in the rest frame and the charge line density λ in the laboratory frame are related by

$$\lambda = \gamma \bar{\lambda}, \quad (28)$$

after the Lorentz transformation.

We assume an elliptical conductive chamber with the major horizontal axis $2h_{E_x} = 2f \cosh u_0$ and the minor vertical axis $2h_{E_y} = 2f \sinh u_0$, where the half distance between the two focal points is calculated as $f = \sqrt{h_{E_x}^2 - h_{E_y}^2}$ for the chamber of $h_{E_x} > h_{E_y}$.

When a point particle is located at (x_s, y_s) , the scalar potential $\bar{\Phi}$ in the rest frame is given by [37]

$$\bar{\Phi}(x, y, x_s, y_s) = -\frac{\bar{\lambda}}{4\pi\epsilon_0} \log \left| \frac{D_s^x C D_s - C_s D C - C_s C - C_s^x}{D_s C D_s^x - C_s^x D D + D_s D + D_s^x} \right|, \quad (29)$$

where ϵ_0 is vacuum permittivity,

$$\begin{aligned} S &= S(\zeta) = \text{sn}(u(\zeta), k), \\ C &= C(\zeta) = \text{cn}(u(\zeta), k), \\ D &= D(\zeta) = \text{dn}(u(\zeta), k), \end{aligned} \quad (30)$$

sn, cn, and dn are the Jacobian elliptic functions, $C_s = C(\zeta_s)$, $D_s = D(\zeta_s)$, $S^x = S(\bar{\zeta}) = \bar{S}$, $C^x = C(\bar{\zeta}) = \bar{C}$, $D^x = D(\bar{\zeta}) = \bar{D}$, $C_s^x = C(\bar{\zeta}_s) = \bar{C}_s$, $D_s^x = D(\bar{\zeta}_s) = \bar{D}_s$ [38], $\zeta = x + iy$, and the complex conjugate $\bar{\zeta}$.

Their arguments are calculated as

$$u(\zeta) = \frac{2K(k)}{\pi} \cos^{-1} \frac{\zeta}{f}, \quad (31)$$

by the complete elliptic integral of the first kind $K(k)$ [38]. The ‘‘modulus’’ k in Eqs. (30) and (31) is determined by $K(\sqrt{1-k^2})/K(k) = 2/\pi \tanh^{-1}(h_{E_y}/h_{E_x})$. From now on, we will simplify the description of $K(k)$ as K by omitting k in the argument of the complete elliptic integral of the first kind, for simplicity.

Once the scalar potential in the rest frame is obtained, the scalar potential Φ in the laboratory frame is calculated as

$$\Phi = \gamma \bar{\Phi}. \quad (32)$$

Accordingly, the horizontal component of the electric field E_x^0 excited by the point charge in the laboratory frame is expressed as

$$\begin{aligned}
E_x^0 &= -\frac{\partial\Phi}{\partial x} \\
&= \frac{\lambda}{4\pi\epsilon_0} \frac{KS}{\pi W} \left[\frac{D}{C-C_1} + \frac{D}{C-C_1^x} - \frac{Ck^2}{D+D_1} - \frac{Ck^2}{D+D_1^x} + \frac{DD_1-C_1Ck^2}{CD_1-C_1D} - \frac{DD_1^x-C_1^xCk^2}{CD_1^x-C_1^xD} \right] \\
&+ \frac{\lambda}{4\pi\epsilon_0} \frac{KS^x}{\pi W^x} \left[\frac{D^x}{C^x-C_1^x} + \frac{D^x}{C^x-C_1} - \frac{C^xk^2}{D^x+D_1^x} - \frac{C^xk^2}{D^x+D_1} + \frac{D^xD_1^x-C_1^xC^xk^2}{C^xD_1^x-C_1^xD^x} - \frac{D^xD_1-C_1C^xk^2}{C^xD_1-C_1D^x} \right],
\end{aligned} \tag{33}$$

where

$$W = W(\zeta) = \sqrt{f^2 - \zeta^2}, \tag{34}$$

and $W^x \equiv W(\bar{\zeta}) = \bar{W}$.

Subsequently, the electric fields by the elliptic uniform beam is calculated after superposing Eq. (33) on the beam cross-section as follows

$$\begin{aligned}
E_x &= \frac{1}{\pi a_x a_y} \iint dx_s dy_s E_x^0 I(x_s, y_s) \\
&= \frac{1}{\pi a_x a_y} \iint dx_s dy_s (E_{x,DS}^0 + E_{x,im}^0) I(x_s, y_s),
\end{aligned} \tag{35}$$

where $E_{x,DS}^0$ and $E_{x,im}^0$ are the direct and indirect space charge contributions from the point particle, respectively.

When the witness particles are on the horizontal axis ($y = 0$), $E_{x,DS}^0$ and $E_{x,im}^0$ are simplified as (refer to Appendix B)

$$E_{x,DS}^0 = \frac{\lambda}{2\pi\epsilon_0} \frac{x - x_s}{(x - x_s)^2 + y_s^2}, \tag{36}$$

$$\begin{aligned}
E_{x,im}^0 &= \frac{\lambda}{2\pi\epsilon_0} \left[\frac{KS}{\pi W} \left(\frac{D}{C-C_s} + \frac{D}{C-\bar{C}_s} - \frac{Ck^2}{D+D_s} - \frac{Ck^2}{D+\bar{D}_s} \right) - \frac{x - x_s}{(x - x_s)^2 + y_s^2} \right] \\
&\simeq \frac{\lambda}{2\pi\epsilon_0} \left(A_1 x_s + A_2 x + \frac{A_3}{3} x_s^3 - A_3 x_s y_s^2 + A_4 x_s^2 x - A_4 y_s^2 x + A_3 x_s x^2 \right),
\end{aligned} \tag{37}$$

in the first order approximation, where

$$\begin{aligned}
A_1 &= \frac{1}{6f^2} \left(1 - \frac{4(1-2k^2)K^2}{\pi^2} \right), \\
A_2 &= \frac{1}{6f^2} \left(2 - \frac{4(2-k^2)K^2}{\pi^2} \right), \\
A_3 &= \frac{1}{120f^4} \left(17 - \frac{40(1-2k^2)K^2}{\pi^2} - \frac{16(7+8k^2-8k^4)K^4}{\pi^4} \right), \\
A_4 &= \frac{1}{120f^4} \left(8 - \frac{16(8-8k^2-7k^4)K^4}{\pi^4} \right),
\end{aligned} \tag{38}$$

which respectively approach

$$\begin{aligned}
A_1 &\rightarrow \frac{1}{h_C^2}, \\
A_2 &\rightarrow 0, \\
A_3 &\rightarrow 0, \\
A_4 &\rightarrow \frac{1}{h_C^4},
\end{aligned} \tag{39}$$

equivalent to those of a cylindrical chamber with radius h_C , as h_{E_x} approaches $h_{E_y} = h_C$.

The superposition of the electric field on the elliptical beam distribution provides $E_{x,\text{DS}}$ due to the beam itself and $E_{x,\text{im}}$ due to the chamber boundary as follows,

$$\begin{aligned}
E_{x,\text{DS}} &= \frac{1}{\pi a_x a_y} \iint dx_s dy_s E_{x,\text{DS}}^0 I(x_s, y_s) \\
&= \frac{\lambda}{2\pi^2 \epsilon_0 a_x a_y} \int_{-a_x+\bar{x}}^{a_x+\bar{x}} dx_s \int_{-\frac{a_y}{a_x} \sqrt{a_x^2 - (x_s - \bar{x})^2}}^{\frac{a_y}{a_x} \sqrt{a_x^2 - (x_s - \bar{x})^2}} dy_s \frac{x - x_s}{(x - x_s)^2 + y_s^2} \\
&= \frac{\lambda}{\pi^2 \epsilon_0 a_x a_y} \int_{-a_x+\bar{x}}^{a_x+\bar{x}} dx_s \tan^{-1} \left(\frac{a_y \sqrt{a_x^2 - (x_s - \bar{x})^2}}{a_x (x - x_s)} \right) \\
&= \frac{\lambda}{\pi \epsilon_0} \frac{x - \bar{x}}{a_x (a_x + a_y)},
\end{aligned} \tag{40}$$

$$\begin{aligned}
E_{x,\text{im}} &= \frac{1}{\pi a_x a_y} \iint dx_s dy_s E_{x,\text{im}}^0 I(x_s, y_s) \\
&\simeq \frac{\lambda}{2\pi \epsilon_0} \left(A_1 \bar{x} + A_2 x + \frac{1}{4} (a_x^2 - a_y^2) (A_3 \bar{x} + A_4 x) + x \bar{x} (A_3 x + A_4 \bar{x}) + \frac{1}{12} A_3 \bar{x}^3 \right) \\
&\simeq \frac{\lambda}{2\pi \epsilon_0} (A_2 (x - \bar{x}) + (A_1 + A_2) \bar{x}) \\
&= \frac{\lambda}{\pi \epsilon_0} \left(\frac{\epsilon_1}{h_{E_y}^2} (x - \bar{x}) + \frac{\xi_1}{h_{E_y}^2} \bar{x} \right),
\end{aligned} \tag{41}$$

in the first order approximation, after the third term on the second line of Eq. (41) is neglected for a beam whose size is considerably smaller than the chamber size, as indicated by Eq. (39). As a result, the coefficients A_2 and $A_1 + A_2$ are respectively related to the well-known incoherent and coherent electric image coefficients ϵ_1 and ξ_1 for the elliptical chamber [39].

Since the vector potential A_z in the laboratory frame is obtained by

$$A_z = \frac{\beta}{c} \gamma \bar{\Phi}, \tag{42}$$

the electric F_x^{ele} and the magnetic F_x^{mag} contributions to the Lorentz force are respectively expressed with the scalar potential Φ as

$$F_x^{\text{ele}} = -e \nabla_x \Phi = e E_x, \tag{43}$$

$$F_x^{\text{mag}} = e \nabla_x A_z \beta c = -\beta^2 e E_x. \tag{44}$$

Finally, when an elliptic beam with a horizontal offset passes through the elliptic chamber placed in open space, the contributions to the direct space charge force from the electric field $F_{x,\text{DS}}^{\text{ele}}$, and the magnetic field $F_{x,\text{DS}}^{\text{mag}}$, as well as the contributions to the indirect space charge from the electric field $F_{x,\text{im}}^{\text{ele}}$, and the magnetic field $F_{x,\text{im}}^{\text{mag}}$, are summarized as

$$F_{x,\text{DS}}^{\text{ele}} = \frac{e\lambda}{\pi \epsilon_0} \frac{x - \bar{x}}{a_x (a_x + a_y)}, \tag{45}$$

$$F_{x,\text{DS}}^{\text{mag}} = -\beta^2 \frac{e\lambda}{\pi \epsilon_0} \frac{x - \bar{x}}{a_x (a_x + a_y)}, \tag{46}$$

$$F_{x,\text{im}}^{\text{ele}} = \frac{e\lambda}{\pi \epsilon_0} \left(\frac{\epsilon_1}{h_{E_y}^2} (x - \bar{x}) + \frac{\xi_1}{h_{E_y}^2} \bar{x} \right), \tag{47}$$

$$F_{x,\text{im}}^{\text{mag,AC}} = -\beta^2 \frac{e}{\pi \epsilon_0} \left(\lambda - \frac{e N_B}{C} \right) \left(\frac{\epsilon_1}{h_{E_y}^2} (x - \bar{x}) + \frac{\xi_1}{h_{E_y}^2} \bar{x} \right). \tag{48}$$

Here, the DC component of the beam is subtracted in Eq. (48), as illustrated by Laslett [39], because the magnetic field with the DC component can penetrate the metal chamber.

More generally, we deal with the ring composed of cylindrical and elliptical chambers, like the MR, by replacing the coherent electric image coefficients $\epsilon_1/h_{E_y}^2$ and $\xi_1/h_{E_y}^2$ in Eqs. (47) and (48) as

$$\frac{\epsilon_1}{h_{E_y}^2} \rightarrow F \frac{\epsilon_{1,E}}{h_{E_y}^2} + (1-F) \frac{\epsilon_{1,C}}{h_C^2} = F \frac{\epsilon_{1,E}}{h_{E_y}^2}, \quad (49)$$

$$\frac{\xi_1}{h_{E_y}^2} \rightarrow F \frac{\xi_{1,E}}{h_{E_y}^2} + (1-F) \frac{\xi_{1,C}}{h_C^2} = \mathcal{F} \frac{\xi_{1,C}}{h_C^2}, \quad (50)$$

where $\epsilon_{1,C} = 0$ and $\xi_{1,C} = 1/2$ are the Laslett parameters for the cylindrical chamber [39], and F is the filling factor of the elliptical chambers along the ring. In the case of the MR, $h_C = 0.065$ m; $F = 0.358$; $\epsilon_{1,E} = -0.10$ and $\xi_{1,E} = 0.25$, because of $2h_{E_x} = 2 \times 0.065$ m and $2h_{E_y} = 2 \times 0.050$ m, producing $\mathcal{F} = 0.94$. Finally, we modify Eqs. (47) and (48) as

$$F_{x,\text{im}}^{\text{ele}} = \frac{e\lambda}{\pi\epsilon_0} \left(F \frac{\epsilon_{1,E}}{h_{E_y}^2} (x - \bar{x}) + \mathcal{F} \frac{\xi_{1,C}}{h_C^2} \bar{x} \right), \quad (51)$$

$$F_{x,\text{im}}^{\text{mag,AC}} = -\beta^2 \frac{e}{\pi\epsilon_0} \left(\lambda - \frac{eN_B}{C} \right) \left(F \frac{\epsilon_{1,E}}{h_{E_y}^2} (x - \bar{x}) + \mathcal{F} \frac{\xi_{1,C}}{h_C^2} \bar{x} \right), \quad (52)$$

respectively.

Next, let us consider the chamber placed in the bending magnet to derive the DC component in the Lorentz force by presuming a coasting beam with line density eN_B/C with the horizontal centroid of the entire bunch X . In the case, we assume only the magnetic pole surfaces of parallel plates placed perpendicularly to the vertical axis with a distance of $2g$ as the boundary condition, neglecting the chamber boundary.

Because the vector potential A_z by a point charge located at (x_s, y_s) in the laboratory frame is given by [37]

$$A_z = -\frac{\beta}{c} \frac{1}{4\pi\epsilon_0} \frac{eN_B}{C} \log [(\cosh \kappa(x - x_s) - \cos \kappa(y - y_s))(\cosh \kappa(x - x_s) + \cos \kappa(y + y_s))], \quad (53)$$

where $\kappa = \pi/2g$, the corresponding Lorentz force $F_x^{\text{mag},0}$ is calculated as

$$\frac{F_x^{\text{mag},0}}{\beta^2 e} = \frac{\partial A_z}{\partial x} \frac{c}{\beta} = -\frac{1}{2\pi\epsilon_0} \frac{eN_B}{C} \frac{\kappa(\cosh \kappa(x - x_s) - \sin \kappa y \sin \kappa y_s) \sinh \kappa(x - x_s)}{(\cosh \kappa(x - x_s) - \cos \kappa(y - y_s))(\cosh \kappa(x - x_s) + \cos \kappa(y + y_s))}, \quad (54)$$

which is simplified as

$$\begin{aligned} \frac{F_{x,\text{im}}^{\text{mag},0}}{\beta^2 e} &= -\frac{1}{2\pi\epsilon_0} \frac{eN_B}{C} \left(\frac{\kappa \cosh \kappa(x - x_s) \sinh \kappa(x - x_s)}{(\cosh \kappa(x - x_s) - \cos \kappa y_s)(\cosh \kappa(x - x_s) + \cos \kappa y_s)} - \frac{x - x_s}{(x - x_s)^2 + y_s^2} \right) \\ &\simeq -\frac{1}{2\pi\epsilon_0} \frac{eN_B}{C} \left(-\frac{\kappa^2}{3} x_s + \frac{\kappa^2}{3} x + \frac{\kappa^4}{45} x_s^3 - \frac{\kappa^4}{15} x_s y_s^2 - \frac{\kappa^4}{15} x_s^2 x + \frac{\kappa^4}{15} y_s^2 x + \frac{\kappa^4}{15} x_s x^2 \right), \end{aligned} \quad (55)$$

on the horizontal axis ($y = 0$). Similar to deriving Eq. (41), the straightforward superposition of the magnetic field on the elliptical beam provides the contribution to the Lorentz force $F_{x,\text{im}}^{\text{mag,DC}}$ only from the magnetic boundary as

$$\begin{aligned} \frac{F_{x,\text{im}}^{\text{mag,DC}}}{\beta^2 e} &= \frac{1}{\pi a_x a_y} \iint dx_s dy_s \frac{F_{x,\text{im}}^{\text{mag},0}}{\beta^2 e} I(x_s, y_s) \\ &\simeq -\frac{1}{2\pi\epsilon_0} \frac{eN_B}{C} \left(\frac{\kappa^2}{3} (x - X) - \frac{\kappa^4}{60} (a_x^2 - a_y^2) (x - X) + \frac{\kappa^4}{15} x \bar{x} (x - X) + \frac{\kappa^4}{45} X^3 \right) \\ &\simeq -\frac{1}{\pi\epsilon_0} \frac{eN_B}{C} \frac{\pi^2}{24} \frac{1}{g^2} (x - X) \\ &= \frac{1}{\pi\epsilon_0} \frac{eN_B}{C} \left(\frac{\epsilon_2}{g^2} (x - X) + \frac{\xi_2}{g^2} X \right), \end{aligned} \quad (56)$$

where the higher-order terms are neglected by assuming the large magnetic pole surfaces. Again, the well-known incoherent and coherent magnetic image coefficients for the parallel plate boundary, ϵ_2 and ξ_2 appear in the Lorentz force. Note that the Laslett parameter $\xi_2 = 0$ in the horizontal direction when the parallel magnetic planes [39] are oriented perpendicular to the vertical axis.

Thus, the Lorentz force due to the magnetic image is given by

$$F_{x,\text{im}}^{\text{mag,DC}} = \beta^2 \frac{e}{\pi\epsilon_0} \frac{eN_B}{C} F_B \left(\frac{\epsilon_2}{g^2} (x - X) + \frac{\xi_2}{g^2} X \right), \quad (57)$$

where F_B is the filling factor of the bending magnet along the ring. In the case of the MR, the half-height of the ferromagnetic material g is equal to 0.053 m, and the filling factor $F_B = F$, because the elliptical chamber only occupies the bending region.

Finally, we can simplify the equation of motion by summing up Eqs. (45), (46), (51), (52), and (57) as

$$\begin{aligned} x'' &= \frac{1}{\gamma m_p c^2 \beta^2} \left(F_{x,\text{DS}}^{\text{ele}} + F_{x,\text{DS}}^{\text{mag}} + F_{x,\text{im}}^{\text{ele}} + F_{x,\text{im}}^{\text{mag,AC}} + F_{x,\text{im}}^{\text{mag,DC}} \right) \\ &= \frac{e}{\pi\epsilon_0 m_p c^2 \gamma \beta^2} \left[\left(\frac{\lambda}{\gamma^2} \frac{1}{a_x(a_x + a_y)} + \frac{\lambda}{\gamma^2} F \frac{\epsilon_{1,E}}{h_{E_y}^2} + \beta^2 \frac{eN_B}{C} F \frac{\epsilon_{1,E}}{h_{E_y}^2} \right) (x - \bar{x}) + \beta^2 \frac{eN_B}{C} F \frac{\epsilon_2}{g^2} (x - X) \right] \\ &\quad + \frac{e}{\pi\epsilon_0 m_p c^2 \gamma \beta^2} \left(\frac{\lambda}{\gamma^2} \mathcal{F} \frac{\xi_{1,C}}{h_C^2} + \beta^2 \frac{eN_B}{C} \mathcal{F} \frac{\xi_{1,C}}{h_C^2} \right) \bar{x}. \end{aligned} \quad (58)$$

Accordingly, the horizontal kick at the mesh grid point k by the space charge is implemented into the code as

$$\Delta x'_i = x'' c \beta \Delta T = -\frac{4\pi}{\beta_x} \left(\Delta\nu_{\text{inc}}^{(k)} (x_i - x^{(k)}) + \Delta\nu_{\text{coh}}^{(k)} x^{(k)} \right) \frac{\Delta T}{T_0}, \quad (59)$$

where $\Delta\nu_{\text{inc}}^{(k)}$ is the incoherent tune shift and $\Delta\nu_{\text{coh}}^{(k)}$ is the coherent tune shift. Here, the incoherent tune shift is approximated as

$$\Delta\nu_{\text{inc}}^{(k)} \simeq -\frac{r_p C^2}{2\pi^2 e \gamma^3 \beta^2 \nu_\beta} \frac{\lambda^{(k)}}{a_x^{(k)} (a_x^{(k)} + a_y)}, \quad (60)$$

where $r_p = e^2/4\pi\epsilon_0 m_p c^2 = 1.5 \times 10^{-18}$ m is the classical particle radius of the proton, by neglecting the contribution of terms proportional to ϵ_1 and ϵ_2 , because the beam size in the MR, which is typically $a_{x,y} \leq 0.015$ m, is considerably smaller than the typical chamber size : 0.065 m, and the coherent tune shift is summarized as

$$\Delta\nu_{\text{coh}}^{(k)} = -\frac{r_p C^2}{2\pi^2 e \gamma^3 \beta^2 \nu_\beta} \lambda^{(k)} \mathcal{F} \frac{\xi_{1,C}}{h_C^2} - \frac{N_B r_p C}{2\pi^2 \gamma \nu_\beta} \mathcal{F} \frac{\xi_{1,C}}{h_C^2}. \quad (61)$$

Note that the respective macroparticles must follow the symplectic transformation even when the space charge effects are incorporated into the code. This is summarized as

$$x_{n+1} = \cos \left(2\pi(\nu_\beta + \xi\delta_n) \frac{\Delta T}{T_0} \right) x_n + \beta_x \sin \left(2\pi(\nu_\beta + \xi\delta_n) \frac{\Delta T}{T_0} \right) x'_n, \quad (62)$$

$$\begin{aligned} x'_{n+1} &= -\frac{1}{\beta_x} \sin \left(2\pi(\nu_\beta + \xi\delta_n) \frac{\Delta T}{T_0} \right) x_n + \cos \left(2\pi(\nu_\beta + \xi\delta_n) \frac{\Delta T}{T_0} \right) x'_n \\ &\quad - \frac{4\pi}{\beta_x} \Delta\nu_{\text{inc}} \frac{\Delta T}{T_0} (x_{n+1} - \overline{x_{n+1}}) - \frac{4\pi}{\beta_x} \Delta\nu_{\text{coh}} \frac{\Delta T}{T_0} \overline{x_{n+1}}, \end{aligned} \quad (63)$$

after combining Eqs. (3), (4), (5), and (59). In other words, the third and fourth terms on the right-hand side of Eq. (63) must be proportional to x_{n+1} rather than x_n .

As for the beam parameters, a_y is fixed, because our code only tracks the horizontal motion of the particles. For the horizontal beam parameter a_x , it must be determined time step by step during the simulation process. In the tracking simulation, the transverse charge distribution is assumed to follow a Gaussian beam, as shown in

$$\rho(x, y) = \frac{\lambda}{2\pi\sigma_x\sigma_y} \exp \left(-\frac{(x - \bar{x})^2}{2\sigma_x^2} - \frac{y^2}{2\sigma_y^2} \right), \quad (64)$$

with the horizontal rms beam size σ_x and the vertical rms beam size σ_y , producing the line density λ after integrating over the transverse plane.

Now, we set $a_x = \sqrt{2}\sigma_x$ with $a_y = \sqrt{2}\sigma_y = 0.014$ m in Eq. (60) to reconcile the space charge calculation based on the elliptical distribution with that on the Gaussian distribution. This is because the peak densities of the elliptical beam with $a_x = a_y$ and the Gaussian beam with $\sigma_x = \sigma_y$ are identified as $\lambda/\pi a_x^2$ and $\lambda/2\pi\sigma_x^2$ respectively, for the same line density λ . In the case of the MR, the typical transverse beam sizes are given by $\sigma_x = 0.009$ m and $\sigma_y = 0.010$ m, which are almost symmetric in accordance with the assumption.

V. IMPLEMENTATION OF THE HORIZONTAL WAKE POTENTIAL INTO THE CODE

If the space charge force affects the recoherence time, the wakefields could potentially have an impact on it as well. Since the authors have identified that the effect of the longitudinal impedance on the decoherence time is negligible (the details are provided in Appendix C [40]), this section describes how to implement the horizontal wakefields due to the resistive wall chambers into the code to simulate the impedance source in the MR.

The horizontal resistive wall wake function $W_{T1}(s)$ is given by [41–44]

$$W_{T1}(s) = \frac{LD_{1x}(u_0)}{h_{E_y}^3} \frac{2cZ_0\rho}{\pi d_\omega} \sum_{n=0}^{\infty} \exp\left(-\frac{\pi^2\rho}{d_\omega^2} s \left(n + \frac{1}{2}\right)^2\right) \quad (65)$$

$$\approx \begin{cases} \frac{LD_{1x}(u_0)}{h_{E_y}^3} \frac{cZ_0\sqrt{\rho}}{\pi\sqrt{\pi}} \sqrt{\frac{1}{s}}, & \text{for } 0 < s < 500\text{m}, \\ \frac{LD_{1x}(u_0)}{h_{E_y}^3} \frac{2cZ_0\rho}{\pi d_\omega} \exp\left(-\frac{\pi^2\rho}{d_\omega^2} \frac{s}{4}\right), & \text{for } s > 500\text{m}, \end{cases}$$

for an elliptic chamber with the major horizontal axis $2h_{E_x} = 2f \cosh u_0$, the minor vertical axis $2h_{E_y} = 2f \sinh u_0$, ($f = \sqrt{h_{E_x}^2 - h_{E_y}^2}$), a finite thickness d_ω , a length L , SUS316L resistivity $\rho = 1.96 \times 10^{-9}$ m, and the impedance of free space $Z_0 = 120\pi\Omega$, where

$$D_{1x}(u_0) = \frac{\sinh^3 u_0}{4\pi} \int_0^{2\pi} dv \frac{Q_{1x}^2(v)}{\sqrt{\sinh^2 u_0 + \sin^2 v}}, \quad (66)$$

$$Q_{1x}(v) = 2 \sum_{m=0}^{\infty} (-1)^m (2m+1) \frac{\cos(2m+1)v}{\cosh(2m+1)u_0}. \quad (67)$$

The factor $D_{1x}(u_0)$ characterizes the asymmetry of the elliptic chamber and approaches one for a cylindrical chamber. Notice that the wake function $W_{T1}(s)$ is proportional to $LD_{1x}/h_{E_y}^3$. As the thickness d_ω goes to infinity, Eq. (65) becomes proportional to $1/\sqrt{s}$, which is typical behavior of the resistive wall impedance. In other words, we can make use of the damping effect due to the chamber thickness in Eq. (65) to calculate beam behavior affected by the resistive wall impedance.

In the MR, where the cylindrical chamber with an inner radius $h_C (= 0.065$ m) dominates, the thickness of the chamber is $d_\omega (= 0.002$ m). The bending magnet region, where the elliptical ducts with a major axis $2h_{E_x} (= 2 \times 0.065$ m) and a minor axis $2h_{E_y} (= 2 \times 0.050$ m), equivalent to $D_{1x} = 0.615$, are placed, occupies $F (= 0.358)$ of the total circumference of the ring. Hence, the total resistive wall impedance along the ring, including the effect of the elliptic chambers, is enhanced by the factor \mathcal{G} :

$$\mathcal{G} = FD_{1x} \frac{h_C^3}{h_{E_y}^3} + (1 - F) = 1.1, \quad (68)$$

compared to the case where the ring is assumed to be perfectly composed of cylindrical chambers. This indicates that the assumption that the resistive wall wake for the cylindrical chamber:

$$W_{T1}(s) = \frac{C}{h_C^3} \frac{2cZ_0\rho}{\pi d_\omega} \sum_{n=0}^{\infty} \exp\left(-\frac{\pi^2\rho}{d_\omega^2} s \left(n + \frac{1}{2}\right)^2\right), \quad (69)$$

perfectly occupies the MR, estimates the resistive wall impedance of the ring within about 10% accuracy, which is applied for our formulation.

The resistive wall impedance provides the kick on the witness particle in a similar way as the longitudinal wake case. Concretely, the horizontal dipole kick $kick_x^{(k)}$ at the mesh grid point k with a single-turn wake is calculated into the code as

$$kick_x^{(k)} = \sigma_{\Delta} \sum_j W_{T1}(z_j - z^{(k)}) \Delta^{(j)}, \quad (70)$$

where the dipole moment $\Delta^{(j)}$ of j -th segment is calculated as Eq. (16). Using this kick at each segment, the horizontal dipole kick $kick_{x,i}$ on i -th macroparticle between k -th and $(k+1)$ -th grid points are estimated as

$$kick_{x,i} = \left(1 - \frac{z_i - z^{(k)}}{\sigma_{\Delta}}\right) kick_x^{(k)} + \frac{z_i - z^{(k)}}{\sigma_{\Delta}} kick_x^{(k+1)}. \quad (71)$$

Finally, the horizontal dipole kick at each time step is provided as

$$\Delta x'_i = \frac{1}{E_0} kick_{x,i} \frac{\Delta T}{T_0}. \quad (72)$$

Taking into account the thickness of the chamber facilitates dealing with the multi-turn long-range effects on the beams with the rapid decay of the resistive wall impedance, according to Eq. (65). To see the convergence of the accumulated multi-turn wake, let us simply sum the resistive wall impedance up to N_{λ} , assuming the positions of beams exciting the wakes in the previous turns are identical, as

$$V(N_{\lambda}) = \sum_{l=1}^{N_{\lambda}} W_{T1}(lC). \quad (73)$$

Figure 1 shows Eq. (73) for different N_{λ} and the deviation of $V(N_{\lambda})$ from the analytical estimate of Eq. (73) with infinite N_{λ} , respectively. In the MR with circumference $C(=1567.5 \text{ m})$, the deviation reduces to nearly 0.1% after $N_{\lambda} = 4$ turns as already revealed in Ref. [44], because the thickness of the installed chamber is typically $d_{\omega}(=0.002 \text{ m})$. Therefore, we conclude that $N_{\lambda} = 4$ is sufficient to adequately incorporate the accumulation effects of the long-range wakefields in the code.

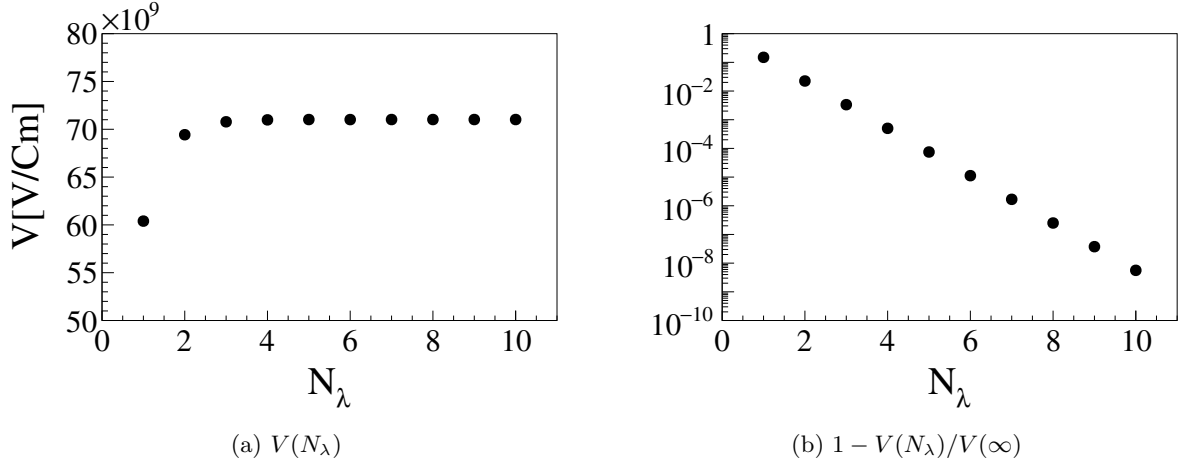


FIG. 1: Sum of multi-turn wakes for different N_{λ} (left) and the deviation from the analytical estimate with infinite N_{λ} (right).

More explicitly, the accumulated horizontal kicks are calculated as

$$\Delta x'_i = \frac{1}{E_0} kick_x \frac{\Delta T}{T_0}, \quad (74)$$

where

$$kick_x = \sum_{l=1}^4 W_{T1}(lC) \Delta_{n-l}, \quad (75)$$

and the dipole moment of the respective bunches is

$$\Delta_n = q \sum_i x_{n,i} = eN_B \bar{x}_n. \quad (76)$$

Here, the transverse centroid of the entire bunch \bar{x}_n in Eq. (76) is calculated by averaging the macroparticle positions in the bunch following Eq. (13).

As a result, the short-range (Eq. (72)) and long-range (Eq. (74)) wakes are simultaneously implemented into the code by making use of the feature of resistive wall impedance with chamber thickness.

VI. DEFINITION OF HEAD-TAIL MODES

The space charge intrinsic eigenmodes, head-tail modes, originally introduced by Blaskiewicz [14], are quite beneficial to interpret the following simulation results describing the intra-bunch motion, though the head-tail modes are assumed to be excited by wakes in most of the cases. In this section, we delineate the intra-bunch transverse motions with respect to the space charge intrinsic modes, based on the ABS model, and an airbag harmonic model (ABH model) which replaces the square-well potential in the original ABS model with a realistic harmonic potential for the longitudinal motions. Finally, the airbag distribution will be replaced by a Gaussian distribution under a weak space charge force as an approximation.

The derivation in detail is beneficial to understand the space charge intrinsic modes are dynamically excited by the synchrotron motions in the bunch, and qualitatively understand the measurements. The derived formula will be used as a tool for conducting benchmark tests of our simulation code in the following sections.

A. Head-tail modes in the ABS model with space charge effects

The horizontal motion of a beam particle in the beam obeys the equation of motion as [13].

$$\frac{d^2}{ds^2}x + \frac{4\pi^2}{C^2}(\nu_\beta + \delta\xi)^2x = \frac{F_{\text{beam}}(x, \bar{x})}{\gamma m_p c^2 \beta^2}, \quad (77)$$

where F_{beam} represents the space charge force and wakefields. When the effects of the wakefields can be neglected, Eq. (77) simplifies to

$$\frac{d^2}{dn^2}x + 4\pi^2(\nu_\beta + \delta\xi)^2x = -8\pi^2\nu_\beta(\Delta\nu_{\text{inc}}(x - \bar{x}) + \Delta\nu_{\text{coh}}\bar{x}), \quad (78)$$

after transforming the variable s to the turn number n by using the relation $s = Cn$.

This simplified equation of motion, as shown in Eq. (78), is realized with the validity of the linear approximation by referring to Eqs. (58), (60), and (61), noting that the transverse beam size must be significantly smaller than the chamber size. Here, we should also note that even an indirect space charge effect can be addressed through the coherent space charge tune shift in Eq. (78).

In the ABS model, Eqs. (6), (11), and (12) follow

$$\frac{dz}{dn} = -\eta C \delta, \quad (79)$$

$$\delta = \pm\delta_0 = \pm \frac{4\hat{z}\nu_s}{|\eta|C}. \quad (80)$$

Let us define the horizontal positions of particles with momentum deviation δ_0 and those with $-\delta_0$ as x_u and x_d , respectively. When $\eta < 0$, we obtain the total derivative with respect to n for x_u and x_d as follows

$$\frac{d}{dn}x_{u,d} = \frac{\partial}{\partial n}x_{u,d} \pm 4\hat{z}\nu_s \frac{\partial}{\partial z}x_{u,d}, \quad (81)$$

where the plus and minus signs in front of the second term correspond to the equations for x_u and x_d , respectively.

On the other hand, the equations of motion for particles Eq. (78) with positive momentum $\delta = \delta_0$ and negative momentum $\delta = -\delta_0$ are described as follows

$$\frac{d}{dn}x_{u,d} = -\mathbf{i}2\pi\nu_\beta x_{u,d} \mp \mathbf{i}2\pi\delta_0\xi x_{u,d} - \mathbf{i}2\pi\Delta\nu_{\text{inc}}(x_{u,d} - \bar{x}) - \mathbf{i}2\pi\Delta\nu_{\text{coh}}\bar{x}, \quad (82)$$

after neglecting the second-order terms for the coherent and incoherent tune shifts. Here, $\bar{x} = (x_u + x_d)/2$ denotes the transverse centroid of the beam. The minus and plus signs in front of the second term in Eq. (82) correspond to the equations for x_u and x_d , respectively.

By combining Eqs. (81) and (82), we obtain

$$4\hat{z}\nu_s \frac{\partial}{\partial z}y_{u,d} = \mp \frac{\partial}{\partial n}y_{u,d} \mp \mathbf{i}2\pi\Delta\nu_{\text{inc}}(y_{u,d} - \bar{y}) \mp \mathbf{i}2\pi\Delta\nu_{\text{coh}}\bar{y}, \quad (83)$$

for y_u and y_d after introducing

$$x_{u,d}(n, z) = \exp\left(\mathbf{i}\chi_{\text{ABS}}\frac{z}{\hat{z}} - \mathbf{i}2\pi\nu_\beta n\right)y_{u,d}(n, z). \quad (84)$$

Here, the minus and plus signs on the right-hand side correspond to the equations for y_u and y_d , respectively, $\bar{y} = (y_u + y_d)/2$, and the chromatic phase χ_{ABS} in the ABS model is defined by

$$\chi_{\text{ABS}} = 2\pi\frac{\xi}{\eta C}\hat{z}, \quad (85)$$

which differs from the definition for the Gaussian beam (refer to Eq. (20)).

To solve Eq. (83), let us assume that it can be separable for the variables z and n by introducing

$$\frac{\partial}{\partial n}y_{u,d} = -\mathbf{i}2\pi\Delta\nu_x y_{u,d}, \quad (86)$$

and solved as

$$y_{u,d}(n, z) = \exp(-\mathbf{i}2\pi\Delta\nu_x n)y_{u,d}(z). \quad (87)$$

Here, we assume that the eigenvalue $\Delta\nu_x$ is identical regardless of the particle's momentum deviation. In this case, the coherent tune shift is generated by the space charge force as $\nu_\beta \rightarrow \nu_\beta + \Delta\nu_x$, referring to Eq. (84).

Finally, Eq. (87) for y_u and y_d is respectively rewritten as

$$\nu_s \frac{d}{d\theta'}y_u(\theta') = -\mathbf{i}\left(\Delta\nu_x - \frac{\Delta\nu_{\text{inc}}}{2} - \frac{\Delta\nu_{\text{coh}}}{2}\right)y_u(\theta') - \mathbf{i}\left(\frac{\Delta\nu_{\text{inc}}}{2} - \frac{\Delta\nu_{\text{coh}}}{2}\right)y_d(\theta'), \quad (88)$$

$$\nu_s \frac{d}{d\theta'}y_d(\theta') = +\mathbf{i}\left(\Delta\nu_x - \frac{\Delta\nu_{\text{inc}}}{2} - \frac{\Delta\nu_{\text{coh}}}{2}\right)y_d(\theta') + \mathbf{i}\left(\frac{\Delta\nu_{\text{inc}}}{2} - \frac{\Delta\nu_{\text{coh}}}{2}\right)y_u(\theta'), \quad (89)$$

where $\theta' = -\pi/2 \times (z/\hat{z} - 1)$ with $(0 < \theta' < \pi)$.

(i) when $\Delta\nu_x \neq \Delta\nu_{\text{coh}}$, which deals with the higher space charge intrinsic modes, y_u and y_d are solved as

$$y_u(\theta') = A_\alpha \cos\left(\frac{\sqrt{(\Delta\nu_x - \Delta\nu_{\text{inc}})(\Delta\nu_x - \Delta\nu_{\text{coh}})}}{\nu_s}\theta'\right) + \mathbf{i}A_\beta \sin\left(\frac{\sqrt{(\Delta\nu_x - \Delta\nu_{\text{inc}})(\Delta\nu_x - \Delta\nu_{\text{coh}})}}{\nu_s}\theta'\right), \quad (90)$$

$$y_d(\theta') = \left(A_\alpha \frac{2\Delta\nu_x - \Delta\nu_{\text{inc}} - \Delta\nu_{\text{coh}}}{\Delta\nu_{\text{coh}} - \Delta\nu_{\text{inc}}} + A_\beta \frac{2\sqrt{(\Delta\nu_x - \Delta\nu_{\text{inc}})(\Delta\nu_x - \Delta\nu_{\text{coh}})}}{\Delta\nu_{\text{coh}} - \Delta\nu_{\text{inc}}}\right) \cos\left(\frac{\sqrt{(\Delta\nu_x - \Delta\nu_{\text{inc}})(\Delta\nu_x - \Delta\nu_{\text{coh}})}}{\nu_s}\theta'\right) + \mathbf{i}\left(A_\beta \frac{2\Delta\nu_x - \Delta\nu_{\text{inc}} - \Delta\nu_{\text{coh}}}{\Delta\nu_{\text{coh}} - \Delta\nu_{\text{inc}}} + A_\alpha \frac{2\sqrt{(\Delta\nu_x - \Delta\nu_{\text{inc}})(\Delta\nu_x - \Delta\nu_{\text{coh}})}}{\Delta\nu_{\text{coh}} - \Delta\nu_{\text{inc}}}\right) \sin\left(\frac{\sqrt{(\Delta\nu_x - \Delta\nu_{\text{inc}})(\Delta\nu_x - \Delta\nu_{\text{coh}})}}{\nu_s}\theta'\right), \quad (91)$$

with arbitrary coefficients A_α and A_β . During synchrotron motion in the square-well potential, the transverse positions do not change abruptly with an instantaneous change in momentum. Hence, the boundary conditions are imposed as

$$\begin{cases} y_u(\theta' = 0) = y_d(\theta' = 0), \\ y_u(\theta' = \pi) = y_d(\theta' = \pi), \end{cases} \quad (92)$$

which provides the eigenvalue $\Delta\nu_x$ as

$$\Delta\nu_{\pm,k} = \frac{\Delta\nu_{\text{inc}} + \Delta\nu_{\text{coh}}}{2} \pm \sqrt{\frac{(\Delta\nu_{\text{inc}} - \Delta\nu_{\text{coh}})^2}{4} + k^2\nu_s^2}, \quad (93)$$

with the condition :

$$A_\alpha = -\frac{k\nu_s}{\Delta\nu_{\pm,k} - \Delta\nu_{\text{coh}}} A_\beta \equiv A_{\pm,k}, \quad (94)$$

where Eq. (93) satisfies $\sqrt{(\Delta\nu_x - \Delta\nu_{\text{inc}})(\Delta\nu_x - \Delta\nu_{\text{coh}})} = k\nu_s$. Notice that the amplitude $A_{\pm,k}$ is independently defined for the respective branches \pm in $\Delta\nu_{\pm,k}$ for the specified $k \in \mathbb{N} = \{1, 2, 3, \dots\}$, and Eq. (93) reproduces the result found in Ref. [14] as $\Delta\nu_{\text{coh}}$ approaches zero neglecting the indirect space charge effect. The case of $k = 0$ must be omitted up to now because $\Delta\nu_x = \Delta\nu_{\text{coh}}$ or $\Delta\nu_x = \Delta\nu_{\text{inc}}$ contradicts the present scope of the assumption.

The concrete calculations demonstrate that the indirect space charge effect is partially incorporated into $\Delta\nu_x$ by neglecting higher-order terms for both the coherent and incoherent tune shifts in the equations of motion: Eq. (82). Moreover, we find that the applicability of the space charge parameter q_{sc} , as mentioned in the introduction, is restricted to the region where the linear approximation for the space charge effect is valid: the beam size is much smaller than the chamber radius, and the indirect space charge effect is negligible.

In summary, $y_u(\theta')$ and $y_d(\theta')$ are provided by the set of $y_{u,\pm,k}(\theta')$ and $y_{d,\pm,k}(\theta')$, which are defined as

$$y_{u,\pm,k}(\theta') = A_{\pm,k} \left(\cos(k\theta') - \mathbf{i} \frac{\Delta\nu_{\pm,k} - \Delta\nu_{\text{coh}}}{k\nu_s} \sin(k\theta') \right), \quad (95)$$

$$y_{d,\pm,k}(\theta') = A_{\pm,k} \left(\cos(k\theta') + \mathbf{i} \frac{\Delta\nu_{\pm,k} - \Delta\nu_{\text{coh}}}{k\nu_s} \sin(k\theta') \right), \quad (96)$$

after Eqs. (93) and (94) are substituted into Eqs. (90) and (91).

(ii) when $\Delta\nu_x = \Delta\nu_{\text{coh}}$, the solution for Eqs. (88) and (89) is given by

$$y_{u,d}(z) = A_0, \quad (97)$$

where A_0 is constant. Referring to Eq. (93), this case expresses the $m = 0$ mode. Accordingly, let us include $(y_{u,0}, y_{d,0}, \Delta\nu_0)$ into the set of solutions for $(y_u, y_d, \Delta\nu_x)$. Note that $\Delta\nu_x$ has only one branch, unlike in Eq. (93).

Finally, referring to Eqs. (84) and (87), the superposition of these solutions provides the horizontal potions of particles with $+\delta_0$ and $-\delta_0$ as

$$\begin{aligned} x_u(n, z) &= \exp\left(\mathbf{i}\chi_{\text{ABS}} \frac{z}{\tilde{z}} - \mathbf{i}2\pi\nu_\beta n\right) A_0 \exp(-\mathbf{i}2\pi\Delta\nu_0 n) \\ &+ \exp\left(\mathbf{i}\chi_{\text{ABS}} \frac{z}{\tilde{z}} - \mathbf{i}2\pi\nu_\beta n\right) \sum_{\pm,k \in \mathbb{N}} A_{\pm,k} \exp(-\mathbf{i}2\pi\Delta\nu_{\pm,k} n) \left(\cos(k\theta') - \mathbf{i} \frac{\Delta\nu_{\pm,k} - \Delta\nu_{\text{coh}}}{k\nu_s} \sin(k\theta') \right), \end{aligned} \quad (98)$$

$$\begin{aligned} x_d(n, z) &= \exp\left(\mathbf{i}\chi_{\text{ABS}} \frac{z}{\tilde{z}} - \mathbf{i}2\pi\nu_\beta n\right) A_0 \exp(-\mathbf{i}2\pi\Delta\nu_0 n) \\ &+ \exp\left(\mathbf{i}\chi_{\text{ABS}} \frac{z}{\tilde{z}} - \mathbf{i}2\pi\nu_\beta n\right) \sum_{\pm,k \in \mathbb{N}} A_{\pm,k} \exp(-\mathbf{i}2\pi\Delta\nu_{\pm,k} n) \left(\cos(k\theta') + \mathbf{i} \frac{\Delta\nu_{\pm,k} - \Delta\nu_{\text{coh}}}{k\nu_s} \sin(k\theta') \right), \end{aligned} \quad (99)$$

which produces the transverse centroid of each segment in the bunch as

$$\begin{aligned} \bar{x}(n, \theta') &= \exp\left(\mathbf{i}\chi_{\text{ABS}} \frac{z}{\tilde{z}} - \mathbf{i}2\pi\nu_\beta n\right) A_0 \exp(-\mathbf{i}2\pi\Delta\nu_0 n) \\ &+ \exp\left(\mathbf{i}\chi_{\text{ABS}} \frac{z}{\tilde{z}} - \mathbf{i}2\pi\nu_\beta n\right) \sum_{k \in \mathbb{N}} A_{+,k} \exp(-\mathbf{i}2\pi\Delta\nu_{+,k} n) \cos(k\theta') \\ &+ \exp\left(\mathbf{i}\chi_{\text{ABS}} \frac{z}{\tilde{z}} - \mathbf{i}2\pi\nu_\beta n\right) \sum_{k \in \mathbb{N}} A_{-,k} \exp(-\mathbf{i}2\pi\Delta\nu_{-,k} n) \cos(k\theta') \\ &= X_0 \sum_{m \in \mathbb{Z}} a_{m,\text{ABS}} \exp\left(\mathbf{i}\chi_{\text{ABS}} \frac{z}{\tilde{z}} - \mathbf{i}2\pi\nu_m n\right) \cos(m\theta'), \end{aligned} \quad (100)$$

where

$$\begin{aligned} \nu_m &= \begin{cases} \nu_0 = \nu_\beta + \Delta\nu_0, \\ \nu_{\pm k} = \nu_\beta + \Delta\nu_{\pm,k}, \end{cases} \\ A_m &= \begin{cases} A_0, \\ A_{\pm k} = A_{\pm,k}, \end{cases} \\ a_{m,\text{ABS}} &= \frac{A_m}{X_0}, \end{aligned} \quad (101)$$

and $m \in \mathbb{Z}$ is an integer. Here, the expansion coefficient A_m is normalized to $a_{m,\text{ABS}}$ by dividing by the initial horizontal position of the beam $\bar{x}(n=0, z) = X_0$ (refer to Sec. III), where all macroparticles are aligned regardless of z ; and the movable region of mode m in the final expression of Eq. (100) is extended to the entire integer region by combining the minus branch with the original mode k . Equations (98)-(100) also cover the special case of $\Delta\nu_{\text{inc}} = \Delta\nu_{\text{coh}}$ after being derived independently for this case.

Finally, substituting $\theta' = -\pi/2 \times (z/\hat{z} - 1)$ into Eq. (100) allows us to expand of the transverse centroid of each segment in the bunch as

$$\begin{aligned} \bar{x}(n, z) &= X_0 \sum_{m \in \mathbb{Z}} a_{m,\text{ABS}} \exp\left(\mathbf{i}\chi_{\text{ABS}} \frac{z}{\hat{z}} - \mathbf{i}2\pi\nu_m n\right) \cos\left(m \frac{\pi}{2} \left(\frac{z}{\hat{z}} - 1\right)\right) \\ &= X_0 \sum_{m \in \mathbb{Z}} \tilde{a}_{m,\text{ABS}}(z) \exp(-\mathbf{i}2\pi\nu_m n), \end{aligned} \quad (102)$$

with the space charge intrinsic modes, the head-tail modes m . Here, the relative amplitude $\tilde{a}_{m,\text{ABS}}(z)$ in each segment is defined as

$$\tilde{a}_{m,\text{ABS}}(z) = a_{m,\text{ABS}} \exp\left(\mathbf{i}\chi_{\text{ABS}} \frac{z}{\hat{z}}\right) \cos\left(m \frac{\pi}{2} \left(\frac{z}{\hat{z}} - 1\right)\right). \quad (103)$$

B. Derivation of the oscillation amplitude with weak space charge force under the ABS model

In Eqs. (98)-(100), the amplitudes $A_{\pm,k}$, or A_m are still unknown factors. In general, determining these parameters becomes quite difficult when space charge effects are significant. However, when this effect is neglected or within the minor level, the amplitudes can be explicitly obtained by comparing Eqs. (98)-(100) with the horizontal positions derived independently, based on the linear decoherence scenario in Sec. III, after applied to the ABS model.

Let us examine the transverse centroid $\bar{x}(n, z)$ for a group of particles with the same longitudinal position z in a given turn n . As in Sec. III, the initial condition is set as $\bar{x}(n=0, z) = X_0$ regardless of the longitudinal position of the particles, with an initial betatron phase of $\phi(n=0, z) = 0$. The equation of motion for a single particle corresponding to Eqs. (6) and (11) is given by Eqs. (79) and (80).

Since the synchrotron phase is followed as $\theta = 2\pi\nu_s n + \theta_0$ with initial phase θ_0 , the equation of motion for a single particle is described as

$$\frac{dz}{d\theta} = \frac{dz}{dn} \frac{dn}{d\theta} = \mp \frac{2\hat{z}}{\pi}. \quad (104)$$

Therefore, each particle motion is followed as

$$z(n, \theta_0) = -\frac{2\hat{z}}{\pi} \cos^{-1}(\cos(\theta(n, \theta_0))) + \hat{z}, \quad (105)$$

$$\delta(n, \theta_0) = \delta_0 \text{sgn}(\sin(\theta(n, \theta_0))). \quad (106)$$

Given $z = z_0$ at $n = n_0$, there are two solutions $\theta_{0,u}(n_0, z_0)$ and $\theta_{0,d}(n_0, z_0)$ for the initial synchrotron phase θ_0 , as

$$\theta_{0,(u,d)}(n_0, z_0) = \mp \frac{\pi}{2\hat{z}} (z_0 - \hat{z}) - 2\pi\nu_s n_0. \quad (107)$$

Hence, the betatron phase advance $\phi_u(n_0, z_0)$ and $\phi_d(n_0, z_0)$ can be calculated for the respective $\theta_{0,(u,d)}(n_0, z_0)$ as

$$\begin{aligned}
\phi_{u,d}(n_0, z_0) &= 2\pi \int_0^{n_0} dn(\nu_\beta + \xi\delta(n, \theta_0)) \\
&= 2\pi\nu_\beta n_0 - 2\pi \frac{\xi}{\eta C} (z(n_0, \theta_0) - z(0, \theta_0)) \\
&= 2\pi\nu_\beta n_0 - 2\pi \frac{\xi}{\eta C} \left(z_0 - \hat{z} + \frac{2\hat{z}}{\pi} \cos^{-1}(\cos(\theta_{0,(u,d)}(z_0, s_0))) \right) \\
&= 2\pi\nu_\beta n_0 - \chi_{\text{ABS}} \left(\frac{z_0}{\hat{z}} - 1 + \frac{2}{\pi} \cos^{-1}(\cos(\mp \frac{\pi}{2} (\frac{z_0}{\hat{z}} - 1) - 2\pi\nu_s n_0)) \right).
\end{aligned} \tag{108}$$

Because of the transverse oscillation with initial condition $\bar{x}(n=0, z) = X_0$, the transverse positions of particles with $\pm\delta_0$ and the transverse centroid of each segment in the bunch are expressed as

$$\begin{aligned}
x_{u,d}(n, z) &= X_0 \exp(-\mathbf{i}\phi_{u,d}(n, z)) \\
&= X_0 \exp(-\mathbf{i}2\pi\nu_\beta n) \exp\left(\mathbf{i}\chi_{\text{ABS}} \left(\frac{z}{\hat{z}} - 1\right)\right) \exp\left[\mathbf{i}\frac{2}{\pi}\chi_{\text{ABS}} \cos^{-1}(\cos(\mp \frac{\pi}{2} (\frac{z}{\hat{z}} - 1) - 2\pi\nu_s n))\right],
\end{aligned} \tag{109}$$

$$\begin{aligned}
\bar{x}(n, z) &= \frac{1}{2} X_0 \exp(-\mathbf{i}2\pi\nu_\beta n) \exp\left(\mathbf{i}\chi_{\text{ABS}} \left(\frac{z}{\hat{z}} - 1\right)\right) \\
&\quad \times \left(\exp\left[\mathbf{i}\frac{2}{\pi}\chi_{\text{ABS}} \cos^{-1}(\cos(-\frac{\pi}{2} (\frac{z}{\hat{z}} - 1) - 2\pi\nu_s n))\right] \right. \\
&\quad \left. + \exp\left[\mathbf{i}\frac{2}{\pi}\chi_{\text{ABS}} \cos^{-1}(\cos(+\frac{\pi}{2} (\frac{z}{\hat{z}} - 1) - 2\pi\nu_s n))\right] \right),
\end{aligned} \tag{110}$$

respectively.

Now, let us equate Eq. (100), the result of the mode expansion method, to Eq. (110), the result of the betatron phase tracking method, producing

$$\begin{aligned}
&2 \sum_{m \in \mathbb{Z}} a_{m,\text{ABS}} \exp(\mathbf{i}\chi_{\text{ABS}}) \exp(-\mathbf{i}m\varphi) \cos(m\theta') \\
&= \exp\left[\mathbf{i}\frac{2}{\pi}\chi_{\text{ABS}} \cos^{-1}(\cos(+\theta' - \varphi))\right] + \exp\left[\mathbf{i}\frac{2}{\pi}\chi_{\text{ABS}} \cos^{-1}(\cos(-\theta' - \varphi))\right],
\end{aligned} \tag{111}$$

where $\theta' = -\pi/2 \times (z/\hat{z} - 1)$ with $(0 < \theta' < \pi)$, and $\varphi = 2\pi\nu_s n$.

After multiplying Eq. (111) by $\exp(\mathbf{i}m\varphi)$ and then integrating it over φ from 0 to 2π , the coefficient $a_{m,\text{ABS}}$ is expressed as

$$a_{m,\text{ABS}} = (-\mathbf{i})^m \frac{\chi_{\text{ABS}}}{\chi_{\text{ABS}}^2 - (m\frac{\pi}{2})^2} \sin\left(\chi_{\text{ABS}} - m\frac{\pi}{2}\right). \tag{112}$$

The transverse centroid of the entire bunch $X(n)$, the average value of Eq. (102) over the longitudinal positions of the bunch, is calculated as

$$X(n) = \int_{-\hat{z}}^{\hat{z}} \frac{dz}{2\hat{z}} \bar{x}(n, z) = X_0 \sum_{m \in \mathbb{Z}} |a_{m,\text{ABS}}|^2 \exp(-\mathbf{i}2\pi\nu_m n), \tag{113}$$

where the amplitude is determined by Eq. (112).

C. Head-tail modes in the ABH model with space charge effects

Next, let us consider the ABH model under any strength of space charge by replacing the square-well potential with a harmonic potential to more realistically describe the motion of particles in the bunch. Equation (7) instead of Eqs. (11) and (12) follow

$$\frac{d\delta}{dn} = \frac{(2\pi\nu_s)^2}{\eta C} z. \tag{114}$$

Rigorously, $\Delta\nu_{\text{inc}}$ and $\Delta\nu_{\text{coh}}$ are distributed along the longitudinal direction within the bunch. However, in this model, we simplify the analysis by neglecting the z -dependence of $\Delta\nu_{\text{inc}}$ and $\Delta\nu_{\text{coh}}$, assuming that the space charge effects near the center of the bunch are well described by the waterbag model and the effects are nearly uniform in the entire bunch.

Consequently, the equations corresponding to Eqs. (81) and (82) are given by

$$\frac{d}{dn}x_{u,d} = \frac{\partial}{\partial n}x_{u,d} - \eta C \delta_{u,d} \frac{\partial}{\partial z}x_{u,d}, \quad (115)$$

$$\frac{d}{dn}x_{u,d} = -\mathbf{i}2\pi\nu_{\beta}x_{u,d} - \mathbf{i}2\pi\delta_{u,d}\xi x_{u,d} - \mathbf{i}2\pi\Delta\nu_{\text{inc}}(x_{u,d} - \bar{x}) - \mathbf{i}2\pi\Delta\nu_{\text{coh}}\bar{x}, \quad (116)$$

where x_u and x_d represent the horizontal positions of particles with momentum deviations $\delta_u > 0$ and $\delta_d < 0$, respectively. By combining Eqs. (115) and (116), we obtain

$$-\eta C \delta_{u,d} \frac{\partial}{\partial z}y_{u,d} = -\frac{\partial}{\partial n}y_{u,d} - \mathbf{i}2\pi\Delta\nu_{\text{inc}}(y_{u,d} - \bar{y}) - \mathbf{i}2\pi\Delta\nu_{\text{coh}}\bar{y}, \quad (117)$$

for y_u and y_d after introducing

$$x_{u,d}(n, z) = \exp\left(\mathbf{i}\chi_{\text{ABH}}\frac{z}{\hat{z}} - \mathbf{i}2\pi\nu_{\beta}n\right)y_{u,d}(n, z), \quad (118)$$

replacing Eqs. (83) and (84) in the ABS model. Here, the chromatic phase χ_{ABH} is defined by

$$\chi_{\text{ABH}} = 2\pi\frac{\xi}{\eta C}\hat{z}, \quad (119)$$

which is equivalent to Eq. (85), because \hat{z} is the half bunch length at the ABH model.

When we discuss only the case of $\eta < 0$, the momentum deviations δ_u and δ_d are uniquely determined for z and are denoted by

$$\delta_{u,d} = \mp \frac{2\pi\nu_s}{\eta C}\sqrt{\hat{z}^2 - z^2}, \quad (120)$$

where the minus and plus signs correspond to δ_u and δ_d , respectively.

Here, by introducing $\theta' = \cos^{-1}(z/\hat{z})$ with $(0 \leq \theta' \leq \pi)$ and applying the formula for Eq. (117), we can obtain the same set of equations as Eqs. (88) and (89) in the ABS model.

Finally, the head-tail mode expansion formula for the transverse centroid of each segment in the bunch is expressed as

$$\bar{x}(n, z) = X_0 \sum_{m \in \mathbb{Z}} a_{m, \text{ABH}} \exp\left(\mathbf{i}\chi_{\text{ABH}}\frac{z}{\hat{z}} - \mathbf{i}2\pi\nu_m n\right) \cos\left(m \cos^{-1}\left(\frac{z}{\hat{z}}\right)\right), \quad (121)$$

in the ABH model, after just substituting $\theta' = \cos^{-1}(z/\hat{z})$ into Eq. (100). When ν_m is replaced by $\nu_{\beta} + m\nu_s$, the outcome reproduces the Formula (6.186) in the Chao's textbook [12], which was derived under the assumption that the space charge effects are negligible from the beginning. In this sense, Eq. (121) successfully generalizes the previous formula to incorporate the space charge effects.

D. Derivation of the oscillation amplitude with weak space charge force under the ABH model

In a similar manner explained in Sec. VIB, we need to derive $\bar{x}(n, z)$ to determine $a_{m, \text{ABH}}$ in the weak space charge limit, following the linear decoherence scenario under the harmonic potential. Since the synchrotron phase is followed as $\theta = 2\pi\nu_s n + \theta_0$ with initial phase θ_0 , the equations of motion given by Eqs. (79) and (114) are rewritten as

$$\frac{dz}{d\theta} = \frac{dz}{dn} \frac{dn}{d\theta} = -\frac{\eta C}{2\pi\nu_s} \delta, \quad (122)$$

$$\frac{d\delta}{d\theta} = \frac{d\delta}{dn} \frac{dn}{d\theta} = \frac{2\pi\nu_s}{\eta C} z, \quad (123)$$

Therefore, each particle motion is followed as

$$z(n, \theta_0) = \hat{z} \cos \theta(n, \theta_0), \quad (124)$$

$$\delta(n, \theta_0) = \frac{2\pi\nu_s}{\eta C} \hat{z} \sin \theta(n, \theta_0). \quad (125)$$

Given $z = z_0$ at $n = n_0$, there are two solutions $\theta_{0,u}(n_0, z_0)$ and $\theta_{0,d}(n_0, z_0)$ for the initial synchrotron phase θ_0 , as

$$\theta_{0,(u,d)}(n_0, z_0) = \pm \cos^{-1} \left(\frac{z_0}{\hat{z}} \right) - 2\pi\nu_s n_0. \quad (126)$$

Hence, the betatron phase advance $\phi_u(n_0, z_0)$ and $\phi_d(n_0, z_0)$ can be calculated for the respective $\theta_{0,(u,d)}(n_0, z_0)$ as

$$\phi_{u,d}(n, z) = 2\pi\nu_\beta n - \chi_{\text{ABH}} \left(\frac{z}{\hat{z}} - \cos(\pm \cos^{-1} \left(\frac{z}{\hat{z}} \right) - 2\pi\nu_s n) \right), \quad (127)$$

where the plus and minus signs on the right-hand side correspond to ϕ_u and ϕ_d , respectively.

Because of the transverse oscillation with initial condition $\bar{x}(n = 0, z) = X_0$, the transverse positions of particles with $\delta_{u,d}$ and the transverse centroid of each segment in the bunch are expressed as

$$x_{u,d}(n, z) = X_0 \exp(-i2\pi\nu_\beta n) \exp \left(i\chi_{\text{ABH}} \frac{z}{\hat{z}} \right) \exp \left[-i\chi_{\text{ABH}} \cos(\pm \cos^{-1} \left(\frac{z}{\hat{z}} \right) - 2\pi\nu_s n) \right], \quad (128)$$

$$\begin{aligned} \bar{x}(n, z) &= \frac{1}{2} X_0 \exp(-i2\pi\nu_\beta n) \exp \left(i\chi_{\text{ABH}} \frac{z}{\hat{z}} \right) \\ &\times \left(\exp \left[-i\chi_{\text{ABH}} \cos(+\cos^{-1} \left(\frac{z}{\hat{z}} \right) - 2\pi\nu_s n) \right] \right. \\ &\left. + \exp \left[-i\chi_{\text{ABH}} \cos(-\cos^{-1} \left(\frac{z}{\hat{z}} \right) - 2\pi\nu_s n) \right] \right), \end{aligned} \quad (129)$$

respectively.

After equating Eq. (129) to Eq. (121), we obtain

$$\begin{aligned} &2 \sum_{m \in \mathbb{Z}} a_{m,\text{ABH}} \exp(-im\varphi) \cos(m\theta') \\ &= \exp[-i\chi_{\text{ABH}} \cos(+\theta' - \varphi)] + \exp[-i\chi_{\text{ABH}} \cos(-\theta' - \varphi)], \end{aligned} \quad (130)$$

corresponding to Eq. (111) in the ABS model, where $\theta' = \cos^{-1}(z/\hat{z})$ with $(0 < \theta' < \pi)$, and $\varphi = 2\pi\nu_s n$. In the end, the coefficient $a_{m,\text{ABH}}$ is expressed as

$$a_{m,\text{ABH}} = (-i)^m J_m(\chi_{\text{ABH}}), \quad (131)$$

where $J_m(x)$ is the Bessel function of the first kind [38]. If we compare Eq. (131) of the ABH model with Eq. (112) of the ABS model, we observe similar responses of the dominant head-tail modes to a given chromatic phase, χ_{ABH} or χ_{ABS} .

The transverse centroid of the entire bunch $X(n)$, the charge-density-weighted average value of Eq. (121) with respect to the airbag distribution over the longitudinal positions of the bunch produces, is calculated as

$$\begin{aligned} X(n) &= \int_{-\hat{z}}^{\hat{z}} \frac{dz}{\pi \sqrt{\hat{z}^2 - z^2}} \bar{x}(n, z) \\ &= X_0 \frac{1}{\pi} \sum_{m \in \mathbb{Z}} (-i)^m J_m(\chi_{\text{ABH}}) \exp(-i2\pi\nu_m n) \int_{-\hat{z}}^{\hat{z}} \frac{dz}{\sqrt{\hat{z}^2 - z^2}} \exp \left(i\chi_{\text{ABH}} \frac{z}{\hat{z}} \right) \cos \left(m \cos^{-1} \left(\frac{z}{\hat{z}} \right) \right) \\ &= X_0 \frac{1}{\pi} \sum_{m \in \mathbb{Z}} (-i)^m J_m(\chi_{\text{ABH}}) \exp(-i2\pi\nu_m n) \pi i^m J_m(\chi_{\text{ABH}}) \\ &= X_0 \sum_{m \in \mathbb{Z}} |a_{m,\text{ABH}}|^2 \exp(-i2\pi\nu_m n), \end{aligned} \quad (132)$$

where the amplitude is determined by Eq. (131).

E. Derivation of the oscillation amplitude for a Gaussian beam with weak space charge force

Now, we consider the transverse centroid of each segment $\bar{x}(n, z)$ in an entire Gaussian bunch by generalizing the ABH model. If the space charge effect is small and there is no interaction between the respective airbags, the calculation can proceed by convolving $\bar{x}(n, z, \delta)$, obtained by replacing \hat{z} in Eq. (121) with $\sqrt{z^2 + (\eta C/2\pi\nu_s)^2 \delta^2}$, with the Gaussian distribution in the momentum direction characterized by the momentum deviation σ_δ , as follows:

$$\bar{x}(n, z) = \int_{-\infty}^{\infty} d\delta \frac{1}{\sqrt{2\pi}\sigma_\delta} \exp\left(-\frac{\delta^2}{2\sigma_\delta^2}\right) \bar{x}(n, z, \delta) = X_0 \sum_{m \in \mathbb{Z}} \tilde{a}_{m,b}(z) \exp(-\mathbf{i}2\pi\nu_m n). \quad (133)$$

Since this result must be the same as Eq. (19) for the weak space charge limit, the relative amplitude $\tilde{a}_{m,b}(z)$ in each segment is calculated in two different ways as :

$$\begin{aligned} \tilde{a}_{m,b}(z) &= \exp\left(\mathbf{i}\chi_\sigma \frac{z}{\sigma_z}\right) (-\mathbf{i})^m \sum_{l=-\infty}^{\infty} J_{m+2l} \left[\chi_\sigma \frac{z}{\sigma_z}\right] (-1)^l \exp\left[-\frac{\chi_\sigma^2}{4}\right] I_l \left[\frac{\chi_\sigma^2}{4}\right] \\ &= \exp\left(\mathbf{i}\chi_\sigma \frac{z}{\sigma_z}\right) (-\mathbf{i})^m \frac{z}{\sqrt{2\pi}\sigma_z} \int_{-\frac{\pi}{2}}^{\frac{\pi}{2}} \frac{d\theta}{\cos^2 \theta} J_m \left[\chi_\sigma \frac{z}{\sigma_z} \frac{1}{\cos \theta}\right] \exp\left[-\frac{z^2}{2\sigma_z^2} \tan^2 \theta\right] \cos(m\theta). \end{aligned} \quad (134)$$

This formula will be compared with the simulation results for the benchmark test of our code in Sec. VII.

Formally, the transverse centroid of the entire bunch $X(n)$ should be calculated by averaging Eq. (133) with a charge-density weight over the longitudinal positions of the bunch, resulting in

$$X(n) = \int_{-\infty}^{\infty} dz \frac{1}{\sqrt{2\pi}\sigma_z} \exp\left(-\frac{z^2}{2\sigma_z^2}\right) \bar{x}(n, z) = X_0 \sum_{m \in \mathbb{Z}} |a_{m,b}|^2 \exp(-\mathbf{i}2\pi\nu_m n). \quad (135)$$

Since the straightforward calculation to derive $X(n)$ and $a_{m,b}$ is quite difficult, we bypass it by generalizing Eq. (132), treating \hat{z} as a variable, and integrating it with a Rayleigh distribution over \hat{z} , resulting in the expression for $X(n)$ as

$$\begin{aligned} X(n) &= \int_0^{\infty} d\hat{z} \frac{\hat{z}}{\sigma_z^2} \exp\left(-\frac{\hat{z}^2}{2\sigma_z^2}\right) X(n, \hat{z}) \\ &= X_0 \sum_{m \in \mathbb{Z}} \int_0^{\infty} d\hat{z} \frac{\hat{z}}{\sigma_z^2} \exp\left(-\frac{\hat{z}^2}{2\sigma_z^2}\right) J_m^2 \left(\chi_\sigma \frac{\hat{z}}{\sigma_z}\right) \exp(-\mathbf{i}2\pi\nu_m n) \\ &= X_0 \sum_{m \in \mathbb{Z}} \exp(-\chi_\sigma^2) I_m(\chi_\sigma^2) \exp(-\mathbf{i}2\pi\nu_m n), \end{aligned} \quad (136)$$

where $I_m(x)$ is the modified Bessel function of the first kind [38], and the chromatic phase satisfies $\chi_{\text{ABH}} = \chi_\sigma \hat{z}/\sigma_z$. This final result is identical to Eq. (24) after m is summed over. Here, we use $\nu_m = \nu_\beta + m\nu_s$, because the space charge is negligible.

The comparison between Eqs. (135) and (136) leads to

$$|a_{m,b}| = \sqrt{\exp(-\chi_\sigma^2) I_m(\chi_\sigma^2)}. \quad (137)$$

Though Eq. (131) features the dominant mode for the chromaticity ξ in the airbag model, they disappear in Eq. (137) and there is no longer the dominant mode for the specified chromaticity ξ in the low-intensity beam because the Gaussian bunches fill in the airbag distribution in the \hat{z} direction.

VII. RESPONSE TO CHROMATICITY AND BEAM INTENSITY IN TRACKING SIMULATION

The developed tracking simulation code in Secs. II, IV, and V enables us to investigate how the frequency (ν_m), and the amplitudes in the respective segments of the bunch ($\tilde{a}_m^{(k)}$) and in the entire bunch (a_m) of the head-tail modes are affected by the transverse wake and space charge effects on the intra-bunch motion unless instabilities are excited after choosing suitable machine parameters. The benchmark tests of the basic algorithm ignoring the space charge effect and the transverse wake are shown in Appendix D. Furthermore, the results of checking the reliability of the parameter settings in the simulation with the space charge effects are surveyed in Appendix E.

In this section, we will scan the beam intensity and chromaticity in the ABS model, or the Gaussian bunch model under the harmonic potential for the longitudinal distribution to realize the limit of the ABS model and understand the space charge effects on the Gaussian bunch. All simulations except Figs. 9 and 20 include the transverse wakefield effects, but the indirect space charge effects may be excluded depending on the specific issue under discussion.

The beam sizes assumed to be $\sigma_x = 0.009$ m with fixed $\sigma_y = 0.010$ m, (refer to the final paragraph in Sec. IV) and the peak charge density $\hat{\lambda}$ determined by Eq. (10) through the bunching factor ($B_f = 0.015$) produce the minimum incoherent tune shift in the bunch :

$$\Delta\nu_{\text{inc}} = -157 \times 10^{-4} \times N_B/10^{12}, \quad (138)$$

and the minimum coherent tune shift in the bunch :

$$\Delta\nu_{\text{coh}} = -7.4 \times 10^{-4} \times N_B/10^{12}, \quad (139)$$

for both potential models, after replacing $a_x^{(k)}$, a_y and $\lambda^{(k)}$ by $\sqrt{2}\sigma_x$, $\sqrt{2}\sigma_y$, and $\hat{\lambda}$ in Eqs. (60) and (61), respectively, though the simulation dynamically changes the horizontal and longitudinal beam sizes.

In both simulations, the tune spectrum, ν_m , and the absolute relative amplitude, $|a_m|$, of the centroid \bar{x}_n (Eq. (13)) for the entire bunch oscillation, along with the corresponding values ($\nu_m, |\tilde{a}_m^{(k)}|$) for the local segments specified by the centroid $x^{(k)}$ (Eq. (18)), are obtained by applying a Fast Fourier Transform (FFT) to the turn-by-turn bunch oscillations from the start of the simulation up to 10000 turns. The results of these simulations will be compared with the theoretical predictions.

A. The tracking simulation with weak space charge force in the ABS model

Now, let us investigate the frequency shifts of the excited betatron oscillation of the particles comprising the low-intensity bunch and the chromaticity dependence of the oscillation amplitudes. Equation (112) suggests that the higher-order head-tail modes can be excited by increasing the chromatic phase (χ_{ABS}) because the dominant mode m is specified as

$$m \simeq \pm \frac{2}{\pi} \chi_{\text{ABS}}, \quad (140)$$

when the space charge effects are small, where Eq. (85) based on the ABS model leads to

$$\chi_{\text{ABS}} = 2\pi \frac{\xi}{\eta C} \hat{z} = -0.87\xi, \quad (141)$$

in the MR.

Figure 2 shows the theoretical relative amplitude $|\tilde{a}_{m,\text{ABS}}(z)|$ calculated by Eq. (103) for various chromaticity ξ . Figure 3 shows the relative amplitude $|\tilde{a}_m^{(k)}|$ in each segment derived from the tracking simulation with the low-intensity $N_B = 1.0 \times 10^8$ protons per bunch (ppb) corresponding to the weak space charge case. In those figures, the black, red, green, blue, orange, magenta, cyan, dark green, purple, and gray denote the cases of $m = 0, 1, 2, \dots, 9$, respectively. The results of the theory and tracking simulation are in nice agreement at this intensity from these figures.

Figure 4 shows simulations of the head-tail tune spectra for the ABS model at $N_B = 1.0 \times 10^8$ ppb by scanning the chromaticity from 0 to -15 , revealing the higher head-tail modes are enhanced for higher chromaticity, as expected. Equations (140) and (141) provide a useful guideline for predicting which mode will be excited in the bunch for a given chromaticity.

Figure 5b represents the simulations of the relative amplitude $|a_m|$ for the entire bunch in the case of $N_B = 1.0 \times 10^8$ ppb, which are compared with the theoretical results (Eq. (112)) in Fig. 5a. The theoretical results fairly reproduce the tracking simulations for $N_B = 1.0 \times 10^8$ ppb, backing the reliability of the code with the weak space charge effects. The reduction in the peak value observed in the simulations at higher chromaticity, compared to theoretical results, is caused by the tune spread within the bunch.

B. The tracking simulation without indirect space charge force in the ABS model

This section deals with the high-intensity cases based on the ABS model without indirect space charge forces ($\Delta\nu_{\text{coh}} = 0$). Equation (93) theoretically suggests that the frequency differences identified by the head-tail modes decrease, as the beam intensity increases.

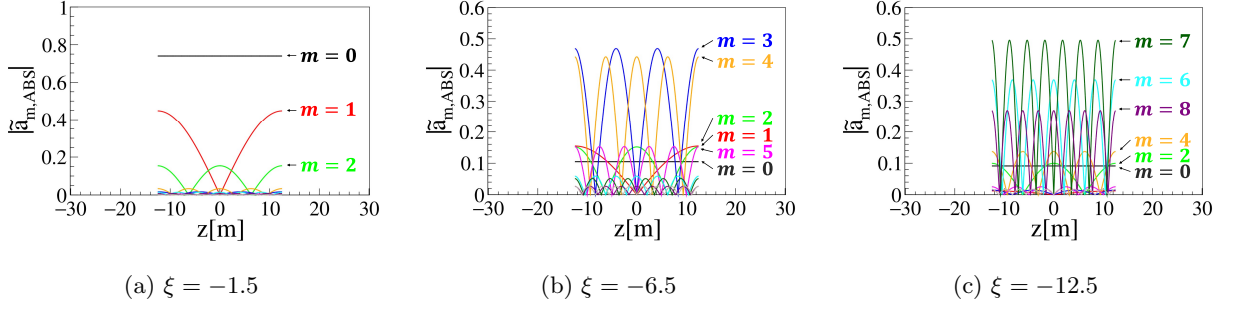


FIG. 2: Analytical results of relative amplitudes $|\tilde{a}_{m,\text{ABS}}(z)|$ calculated by Eq. (103) based on the ABS model with weak space charge force. Here, the black, red, green, blue, orange, magenta, cyan, dark green, purple, and gray denote the cases of $m = 0, 1, 2, \dots, 9$, respectively.

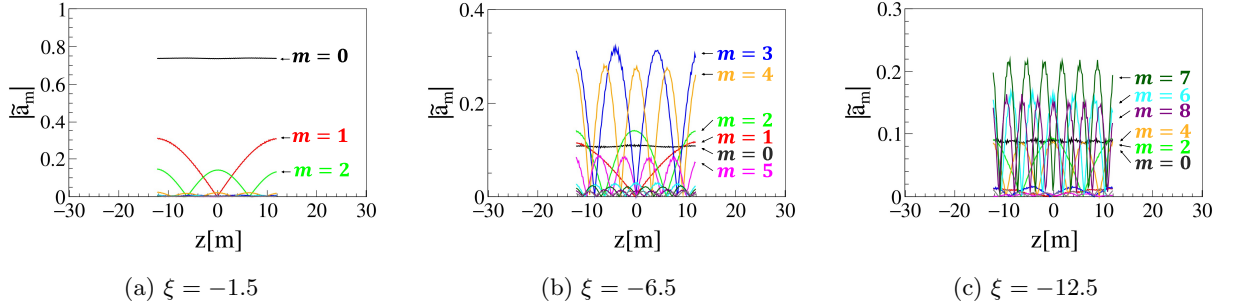


FIG. 3: Relative amplitudes $|\tilde{a}_m^{(k)}|$ in tracking simulation based on the ABS model with weak space charge force ($N_B = 1.0 \times 10^8$ ppb). Here, the black, red, green, blue, orange, magenta, cyan, dark green, purple, and gray denote the cases of $m = 0, 1, 2, \dots, 9$, respectively.

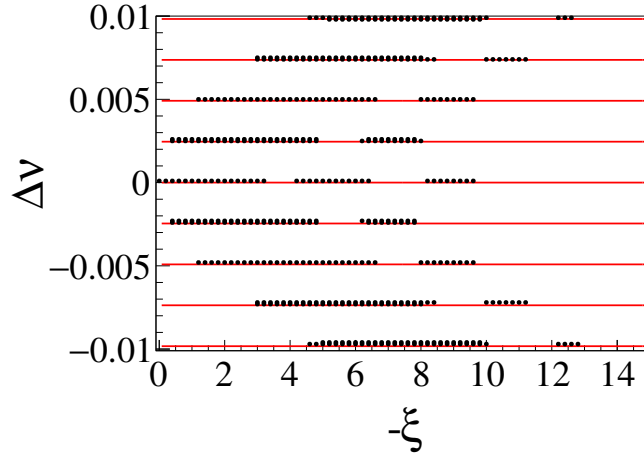


FIG. 4: Head-tail tune spectra in tracking simulation based on the ABS model with weak space charge force ($N_B = 1.0 \times 10^8$ ppb). The dots indicate only the results for $|a_m| > 0.1$. The red lines represent the frequency shifts calculated by Eq. (93) for each head-tail mode in the range of $-4 \leq m \leq 4$.

Figure 6 represents the simulations illustrating the beam intensity dependence of the tune shift for the respective head-tail modes with fixed chromaticity values of (a) $\xi = -1.5$, (b) $\xi = -6.5$, and (c) $\xi = -12.5$. The red lines represent the frequency shifts calculated by Eq. (93) for each head-tail mode from $m = -4$ to 12. The analytical results and the simulations are in good agreement, with the frequency shift degenerating toward high-intensity beams regardless of the chromaticity, following the ABS model, when only the direct space charge effects are taken into

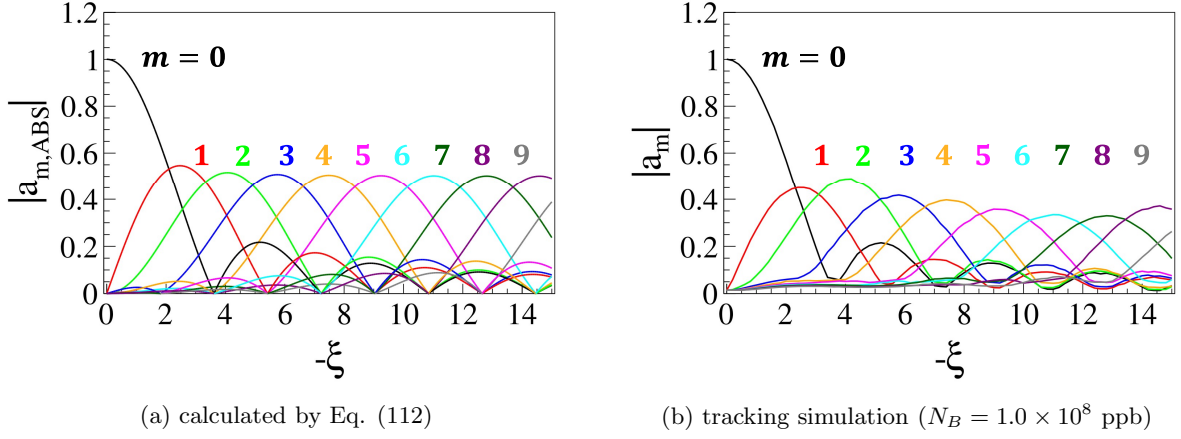


FIG. 5: Relative amplitudes $|a_m|$ calculated by Eq. (112) and tracking simulation based on the ABS model with weak space charge force ($N_B = 1.0 \times 10^8$ ppb). Here, the black, red, green, blue, orange, magenta, cyan, dark green, purple, and gray denote the cases of $m = 0, 1, 2, \dots, 9$, respectively.

account.

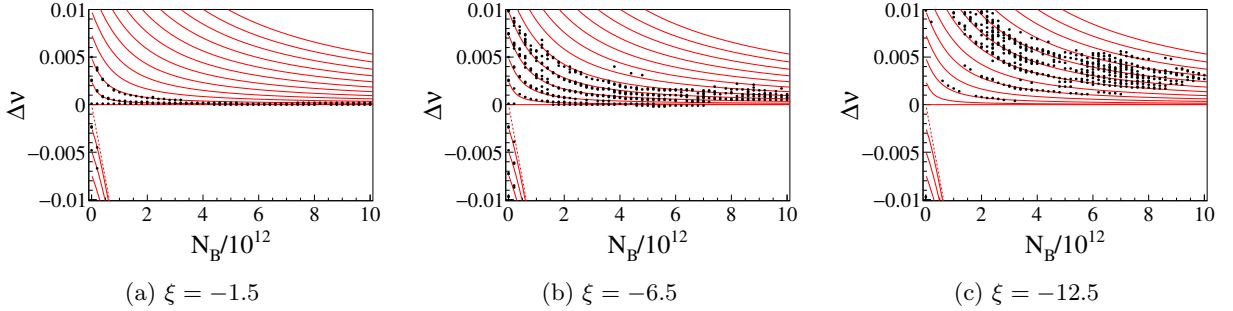


FIG. 6: Head-tail tune spectra in the ABS model without indirect space charge effects for various values of chromaticity : (a) $\xi = -1.5$, (b) $\xi = -6.5$, and (c) $\xi = -12.5$. The dots indicate only the results for $|a_m| > 0.1$. The red lines represent the frequency shifts calculated by Eq. (93) for each head-tail mode in the range of $-4 \leq m \leq 12$.

Note that Eq. (93) suggests that the coherent tune shifts do not depend on the chromaticity. Figure 7 shows the simulations of head-tail tune spectra in the ABS model for various beam intensities, where the analytical results calculated using Eq. (93) are superimposed on the horizontal lines, revealing the chromaticity dependence of the excited head-tail modes for (a) $N_B = 4.2 \times 10^{12}$ ppb and (b) $N_B = 8.6 \times 10^{12}$ ppb. The frequency shifts remain fixed for the respective beam intensities, even though the chromaticity changes. We can recognize that the higher modes are more strongly excited as the absolute value of the chromaticity increases similar to the weak space charge beams. For example, only modes 0 to 2 can be observed at $\xi = -1.5$, while the modes 3 to 6 appear to be observable at $\xi = -8.0$. The result indicates that Eqs. (140) and (141) are still valuable for estimating which mode is excited, even for the high-intensity beams with higher chromaticity, although only positive modes are excited in such cases. This excitation pattern, which is consistent with the previous studies [27–31], is reasonable because the coherent tune shift ($\Delta\nu_{\text{coh}} = 0$) must occur for the entire bunch in the high-intensity beams due to the space charge effects.

Figures 8a and 8b represent the simulations of the relative amplitudes of the entire bunch for $N_B = 4.2 \times 10^{12}$ ppb and 8.6×10^{12} ppb, respectively. In those figures, the black, red, green, blue, orange, magenta, cyan, dark green, dark blue, and gray denote the cases of $m = 0, 1, 2, \dots, 9$, respectively. The comparison between Figs. 5 and 8 demonstrates that the discrepancy between the theoretical results (which exclude space charge effects) and the simulations becomes more evident as the beam intensity increases, as expected.

Though the frequency shifts converge for the high-intensity beams, making it difficult to distinguish which mode is excited in the simulations, particularly at lower chromaticity where the lower modes are excited, we can identify the excited modes across varying chromaticity, up to the case of $N_B = 4.2 \times 10^{12}$ ppb, where the frequency differences among the respective modes are estimated as Eq. (93) for the given beam intensity.

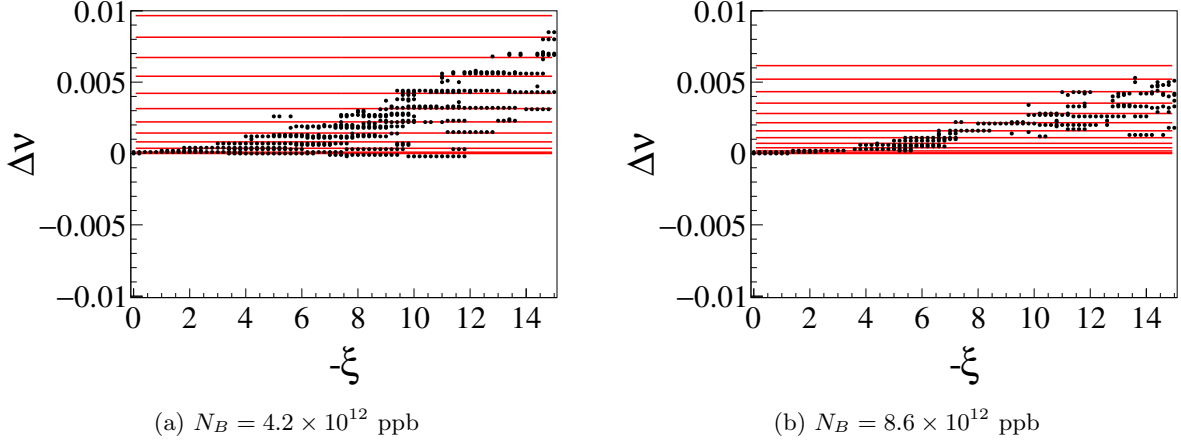


FIG. 7: Head-tail tune spectra in the ABS model without indirect space charge effects for various values of intensity : (a) $N_B = 4.2 \times 10^{12}$ ppb and (b) $N_B = 8.6 \times 10^{12}$ ppb. The dots indicate only the results for $|a_m| > 0.1$. The red lines represent the frequency shifts calculated by Eq. (93) for each head-tail mode in the range of $0 \leq m \leq 12$.

The simulation results demonstrate that the theory accurately predicts the tune shifts because the space charge effects are appropriately considered in the theory, while the amplitude cannot be done because of the lack of space charge effects. Hence, we conclude that we can evaluate the relative amplitude : a_m , of the respective modes from a theoretical perspective for a beam with $|\Delta\nu_{\text{inc}}| \ll \nu_s$ (refer to Eq. (93)). Otherwise, simulation studies are inevitable for an accurate estimate of the beam behaviors.

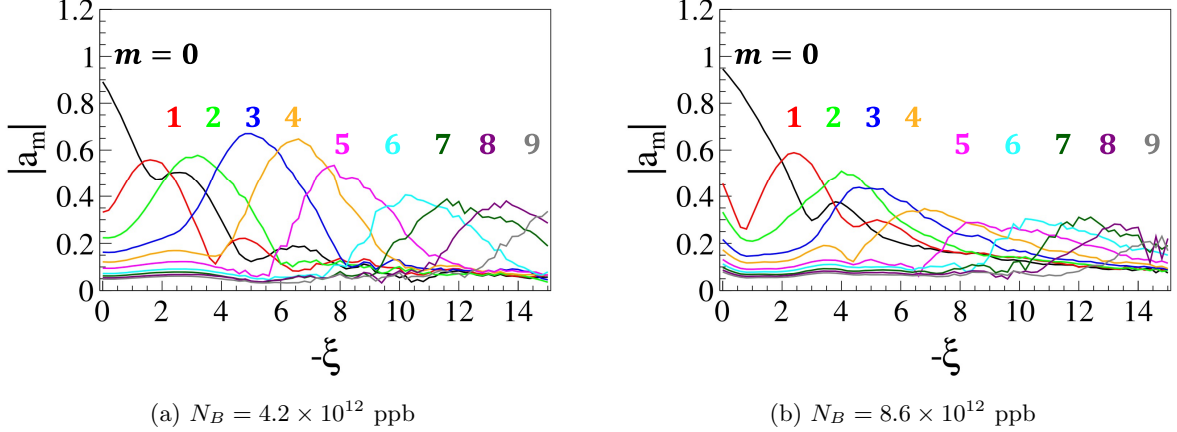


FIG. 8: Relative amplitudes $|a_m|$ based on the tracking simulation of the ABS model without indirect space charge effect. Here, the black, red, green, blue, orange, magenta, cyan, dark green, purple, and gray denote the cases of $m = 0, 1, 2, \dots, 9$, respectively.

Up to now, we have dealt with the simulations including the transverse resistive wall impedance discussed in Sec. V. The simulations suggest that resistive wall impedance does not significantly affect the intra-bunch motion when no beam instability occurs because some agreement can be observed between the analytical results, which consider only space charge effects, and the simulations that include the wakefields.

To clarify this expectation, let us conduct simulations, neglecting the resistive wall impedance. Figure 9 shows the simulation results excluding the wake effects for $\xi = -1.5$ and $\xi = -12.5$, which are nearly identical to the results in Figs. 6a and 6c.

A theoretical estimate of the tune shift due to wakefields offers insight to justify this negligence. The coherent tune shift is given by :

$$\Delta\nu_{\text{coh}} = \Delta\nu_{\text{single}} + \Delta\nu_{\text{mult}} = -0.24 \times 10^{-4} \times N_B/10^{12}, \quad (142)$$

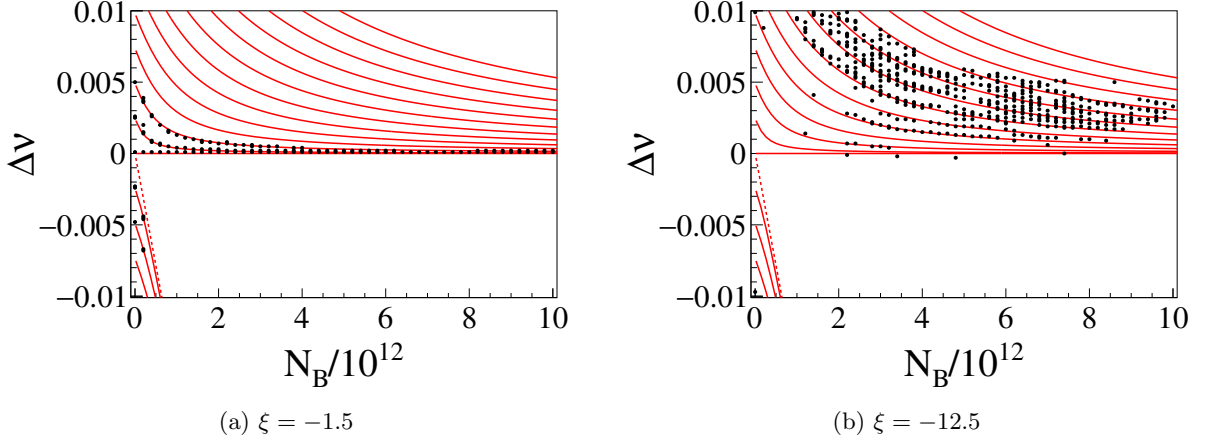


FIG. 9: Head-tail tune spectra in the ABS model without either indirect space charge effect or transverse wake for (a) $\xi = -1.5$ and (b) $\xi = -12.5$. The dots indicate only the results for $|a_m| > 0.1$. The red lines represent the frequency shifts calculated by Eq. (93) for each head-tail mode in the range of $-4 \leq m \leq 12$.

where the coherent tune shift for a Gaussian bunch caused by the single-turn wake is calculated as

$$\begin{aligned} \Delta\nu_{\text{single}} &= -i\mathcal{G} \frac{Cec}{16\pi^2 \sqrt{\pi} \sigma_z \nu_\beta \beta E_0} N_B Z_{\text{dip,eff}}(\omega_\xi) \\ &= (-0.24 - 0.24i) \times 10^{-4} \times N_B/10^{12}, \end{aligned} \quad (143)$$

and the coherent tune shift of the multi-turn is given by

$$\begin{aligned} \Delta\nu_{\text{mult}} &= -\mathcal{G} \frac{C^2 ec p}{4\pi^3 \nu_\beta \beta E_0 h_C^3 d_\omega} N_B \sum_{k=1}^{\infty} \sum_{n=0}^{\infty} e^{-\frac{\pi^2 \rho k C}{d_\omega^2 Z_0} (n+\frac{1}{2})^2 - i2\pi k \nu_\beta} \\ &= (0.016 + 0.018i) \times 10^{-4} \times N_B/10^{12}, \end{aligned} \quad (144)$$

with

$$Z_{\text{dip,eff}}(\omega) = \frac{\sum_{p=-\infty}^{\infty} Z_{T1}^D((p + \nu_\beta)\omega_0) h_0((p + \nu_\beta)\omega_0 - \omega)}{\sum_{p=-\infty}^{\infty} h_0((p + \nu_\beta)\omega_0 - \omega)}, \quad (145)$$

$$Z_{T1}^D(\omega) = Z_0(\text{sgn}(\omega) - i) \frac{C}{2\pi b^3} \delta, \quad (146)$$

$\omega_\xi = \omega_0 \xi / \eta$ (the definition of chromaticity in Ref. [12] differs from the one used in this paper), $h_0(\omega) = \exp(-\omega^2 \sigma_z^2 / c^2)$, and $\delta = \sqrt{2c\rho / Z_0 |\omega|}$.

When the resistive wall wake from Eq. (65) is used as the input parameter, Eq. (142) yields two orders of magnitude smaller than Eq. (139). Thus, we conclude that the theory, accounting only for the direct space charge effect, accurately explains the simulations for the ABS model with resistive wall impedance of the MR, provided no beam instability is triggered and the wakefield-induced tune shift is negligibly smaller than that caused by the space charge forces within the bunch.

C. The tracking simulation with indirect space charge force in the ABS model

Next, let us include the indirect space charge effects in the ABS model. Figure 10 illustrates the excited frequency modes for the same set of chromaticity as in Fig. 6, where the analytical lines given by Eq. (93) are overwritten from $m = -4$ to 12. We find that the indirect space charge effects cause the significant deformations in the tune shifts of the high-intensity beams. Similar to the case with only the direct space charge considered, as the beam intensity increases, the frequency shifts excited by the respective head-tail modes become degenerate. However, the indirect

space charge effect mitigates the mode degeneration of the tune shifts, making it more discernible, as explained by the analytical results in Eq. (93). Though only positive modes are excited in the high-intensity beams, this phenomenon is consistent with the previous simulations only including the direct space charge effect because the finite coherent tune shift ($\Delta\nu_{\text{coh}} \neq 0$) must occur for the entire bunch due to the indirect space charge effect. Even when the indirect space charge is included in simulations, the frequency shift due to the head-tail mode can be sufficiently explained by the theoretical ABS model including the space charge effects.

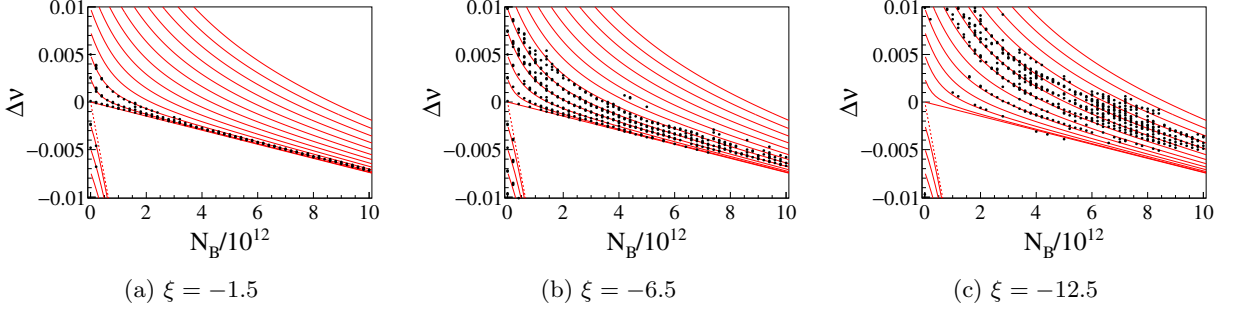


FIG. 10: Head-tail tune spectra in the ABS model with indirect space charge effect in addition to the direct space charge effects and the wakefields for various values of chromaticity : (a) $\xi = -1.5$, (b) $\xi = -6.5$, and (c) $\xi = -12.5$. The dots indicate only the results for $|a_m| > 0.1$. The red lines represent the frequency shifts calculated by Eq. (93) for each head-tail mode in the range of $-4 \leq m \leq 12$.

As for the chromaticity dependence, Fig. 11 illustrates the higher modes can be excited, by increasing the absolute value of the chromaticity, similar to the case, as shown in Fig. 6. For reference, the analytical results calculated using Eq. (93) are superimposed on the horizontal lines. We can confirm the theoretical prediction that the chromaticity dependence of the tune shift is negligible, even when the indirect space charge effect is considered.

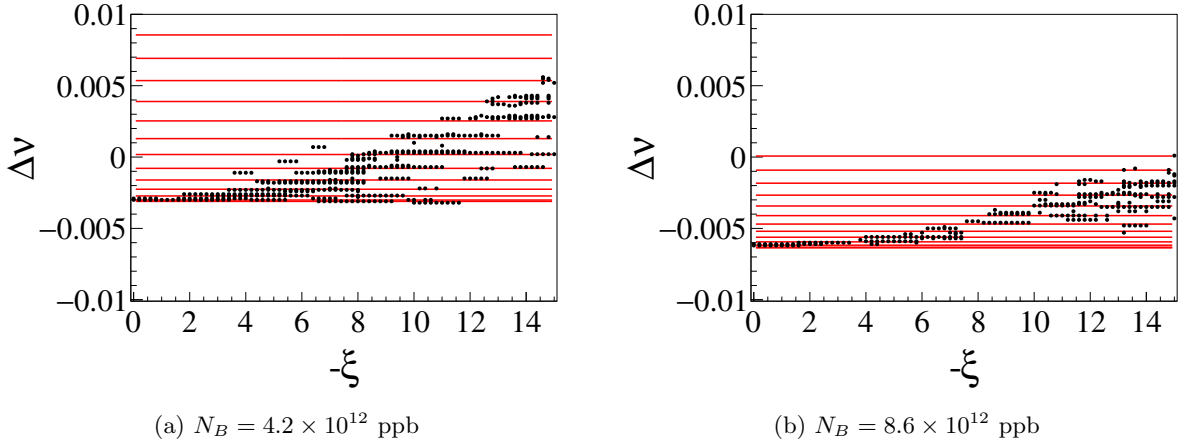


FIG. 11: Head-tail tune spectra in the ABS model with indirect space charge effect in addition to the direct space charge effects and the wakefields for various values of intensity : (a) $N_B = 4.2 \times 10^{12}$ ppb and (b) $N_B = 8.6 \times 10^{12}$ ppb. The dots indicate only the results for $|a_m| > 0.1$. The red lines represent the frequency shifts calculated by Eq. (93) for each head-tail mode in the range of $0 \leq m \leq 12$.

Similarly to the previous case, let us calculate the relative amplitude of the entire bunch. Figure 12 shows the results, including the indirect space charge effect as well as the direct space charge effect. Compared to Fig. 8, which accounts only for the direct space charge effect, there are few noticeable differences between the two. This suggests that when the linear approximations are valid for describing space charge effects, where the chamber radius is significantly larger than the transverse beam size, the relative amplitude remains unaffected by the indirect space charge force.

In conclusion, the theory based on the ABS model successfully predicts the tune shifts, the chromaticity dependence of the spectrum, and the detection of enhancement of modes (but partially) for specified chromaticities in the high-

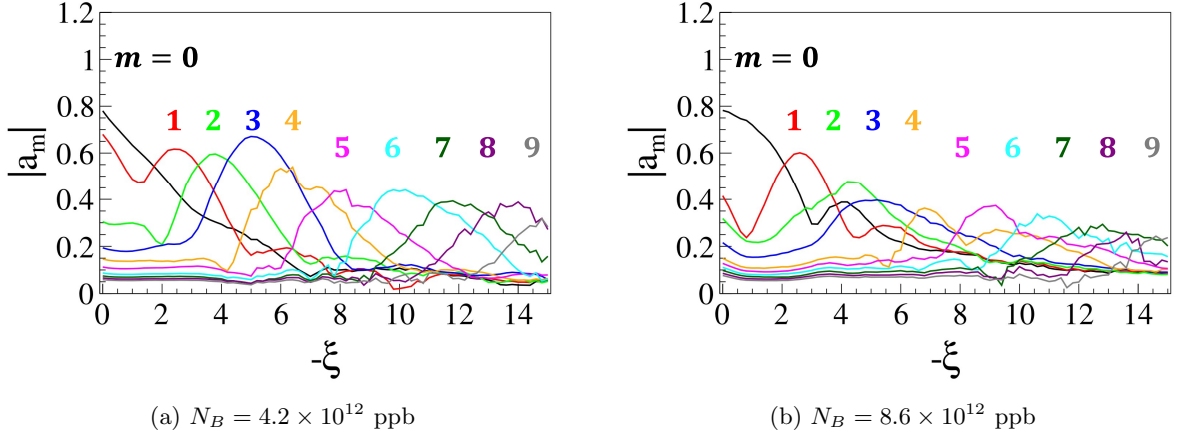


FIG. 12: Relative amplitudes $|a_m|$ derived from the tracking simulation of the ABS model with the indirect and direct space charge effects as well as the wakefield effects. Here, the black, red, green, blue, orange, magenta, cyan, dark green, purple, and gray denote the cases of $m = 0, 1, 2, \dots, 9$, respectively.

intensity beams where space charge effects are significant, provided the transverse beam size is much smaller than the chamber radius.

The theoretical results, which account for the weak space charge effects, predict the relative amplitude of the entire bunch when $|\Delta\nu_{\text{inc}}| \ll \nu_s$. However, for the high-intensity beams where $|\Delta\nu_{\text{inc}}| > \nu_s$, numerical simulations are necessary to obtain accurate results including the space charge forces.

D. The tracking simulation with weak space charge force for a Gaussian beam

To cope with a more realistic case, we start focusing on tracking simulations within a Gaussian bunch with weak space charge force under the harmonic potential model and analyze them in the same way as the ABS model.

Figure 13 shows the relative amplitude $|\tilde{a}_{m,b}(z)|$ calculated by Eq. (134) for various chromaticity ξ . Meanwhile, Fig. 14 shows the relative amplitude $|\tilde{a}_m^{(k)}|$ in each segment derived from the tracking simulation with the low-intensity $N_B = 1.0 \times 10^8$ ppb. In those figures, the black, red, green, blue, orange, magenta, cyan, dark green, purple, and gray denote the cases of $m = 0, 1, 2, \dots, 9$, respectively.

We observe that the oscillation amplitudes vary sharply with higher chromaticity for the respective head-tail modes in both the analytical and simulation results. This behavior can be readily understood by modifying Eq. (134) as

$$\tilde{a}_{m,b}(z) \simeq \exp\left(\mathbf{i}\chi_\sigma \frac{z}{\sigma_z}\right) (-\mathbf{i})^m \exp\left(-\frac{\chi_\sigma^2}{4}\right) I_{\frac{m}{2}}\left(\frac{\chi_\sigma^2}{4}\right) \cos\left(\chi_\sigma \frac{z}{\sigma_z} - m\frac{\pi}{2}\right), \quad (147)$$

as it highlights $|\tilde{a}_{m,b}(z)| \propto |\cos(\chi_\sigma z/\sigma_z - m\pi/2)|$, indicating that the oscillation frequency becomes more pronounced for a fixed head-tail mode as chromaticity increases through χ_σ .

The excellent agreement between the theory and the tracking simulation demonstrates the practical usefulness of the theory at the low-intensity. Conversely, it opens a window for investigating the high-intensity beams with strong space charge effects using our simulation tool.

Figure 15 represents the head-tail tune spectra of the harmonic potential model at $N_B = 1.0 \times 10^8$ ppb in the chromaticity range of 0 to -15 , revealing the chromaticity dependence of the excited head-tail modes. Unlike the ABS model (see Fig. 4), all modes are excited even in the high chromaticity region in the Gaussian bunch model.

Figure 16 compares the relative amplitude $|a_m|$ of the entire bunch for each mode in the case of $N_B = 1.0 \times 10^8$ ppb simulated by the code, with that calculated using the theory (Eq. (137)). The theoretical results fairly reproduce the tracking simulations for $N_B = 1.0 \times 10^8$ ppb because the relative amplitude is derived by assuming the space charge effects is negligible. Compared to Fig. 5, it is evident that all modes are excited in the higher chromaticity regions for the low-intensity beams, and the specific mode enhancement dependence on the chromaticity disappears in the Gaussian model, which is consistent with the results in Fig. 15.

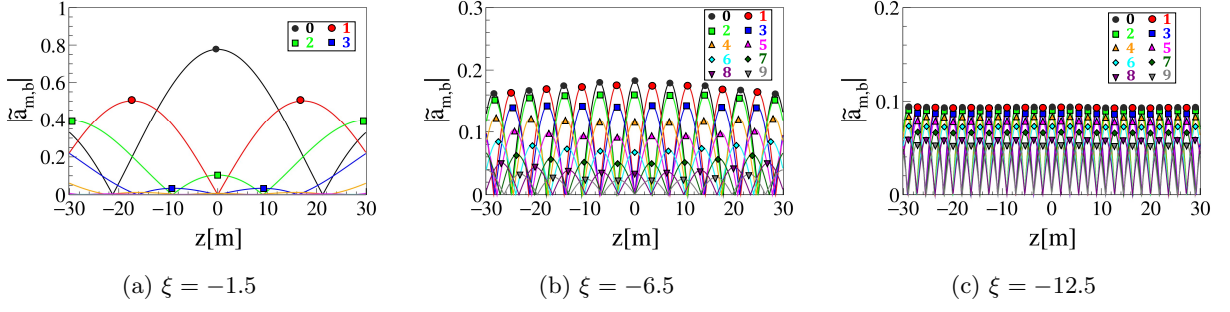


FIG. 13: Relative amplitudes $|\tilde{a}_{m,b}(z)|$ calculated by Eq. (134) based on the harmonic potential model with weak space charge force. Here, the black, red, green, blue, orange, magenta, cyan, dark green, purple, and gray denote the cases of $m = 0, 1, 2, \dots, 9$, respectively.

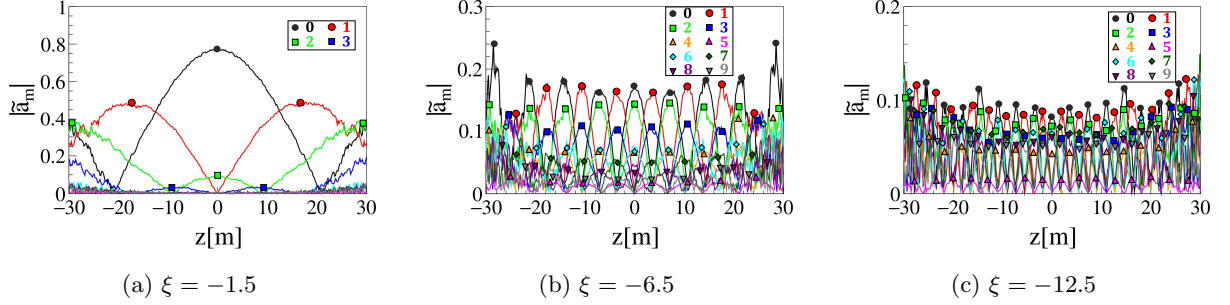


FIG. 14: Relative amplitudes $|\tilde{a}_m^{(k)}|$ in tracking simulation based on the harmonic potential model with weak space charge forces. Here, the black, red, green, blue, orange, magenta, cyan, dark green, purple, and gray denote the cases of $m = 0, 1, 2, \dots, 9$, respectively.

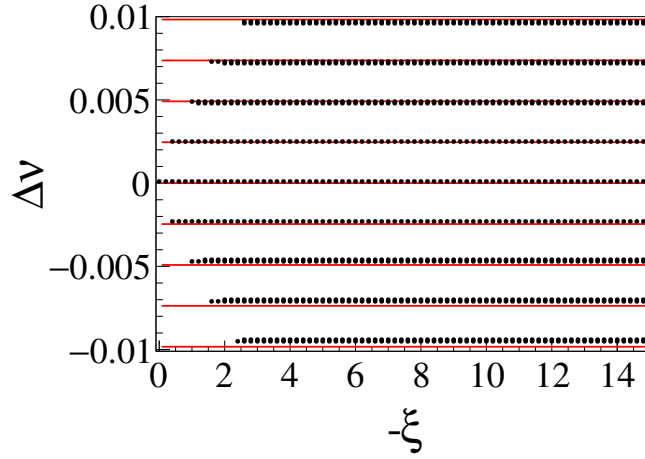


FIG. 15: Head-tail tune spectra in tracking simulation based on the harmonic potential model with weak space charge force. The dots indicate only the results for $|a_m| > 0.1$. The red lines represent the frequency shifts calculated by Eq. (93) for each head-tail mode in the range of $-4 \leq m \leq 4$.

E. The tracking simulation without indirect space charge force for the Gaussian beam

Next, we focus on tracking simulations of Gaussian beams within the harmonic potential model, only including the direct space charge effect. Figure 17 shows the simulations for the same set of chromaticity as in Fig. 6 with the ABS model. The theoretical results calculated using the ABS model: Eq. (93), with the average current matched to the

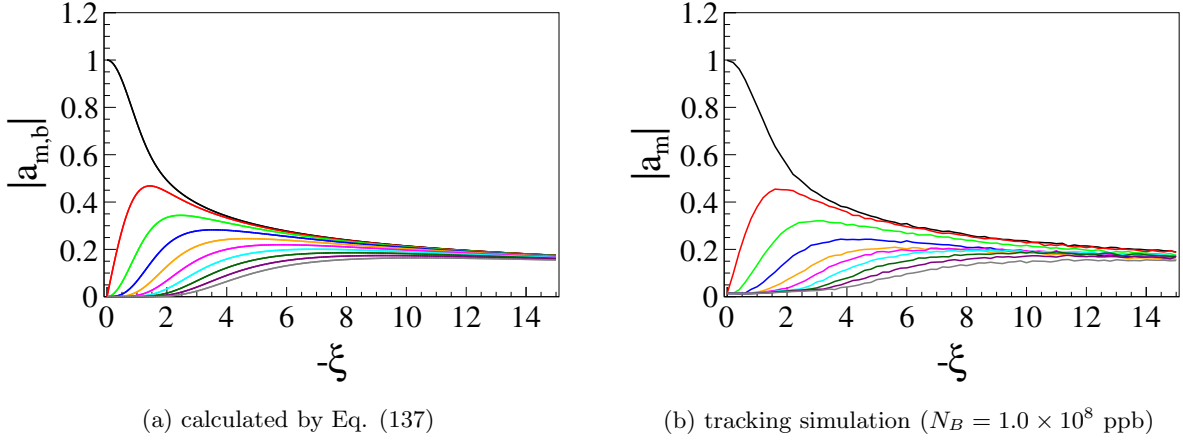


FIG. 16: Relative amplitudes $|a_m|$ calculated by Eq. (137) and tracking simulation of the harmonic potential model with weak space charge forces. Here, the black, red, green, blue, orange, magenta, cyan, dark green, purple, and gray denote the cases of $m = 0, 1, 2, \dots, 9$, respectively.

peak current of the Gaussian bunch, are superimposed as solid lines. As a result, it is confirmed that the ABS model can accurately describe the tune shift of the harmonic potential.

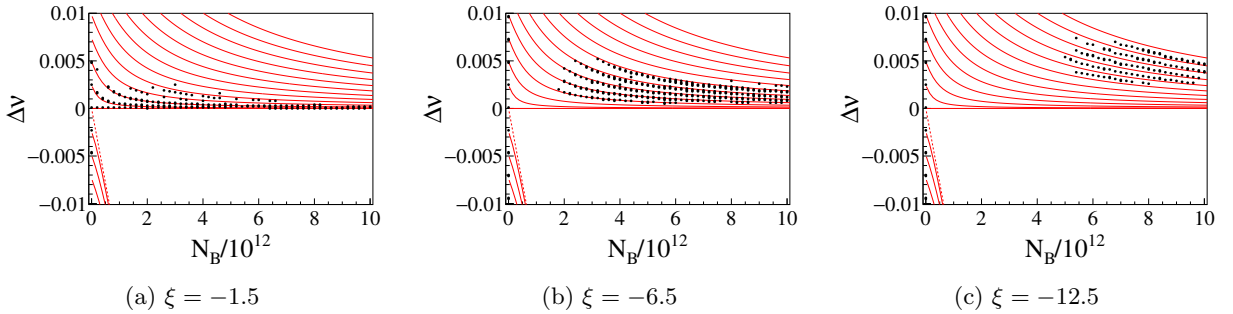


FIG. 17: Head-tail tune spectra in the harmonic potential model without indirect space charge effect for various values of chromaticity : (a) $\xi = -1.5$, (b) $\xi = -6.5$, and (c) $\xi = -12.5$. The dots indicate only the results for $|a_m| > 0.1$. The red lines represent the frequency shifts calculated by Eq. (93) for each head-tail mode in the range of $-4 \leq m \leq 12$.

Figure 18 shows the chromaticity dependence of the excited intra-bunch modes for the cases of (a) $N_B = 4.2 \times 10^{12}$ ppb and (b) $N_B = 8.6 \times 10^{12}$ ppb. For reference, the analytical results calculated using Eq. (93) are superimposed on the horizontal lines. The tune shift shows no chromaticity dependence, a feature also observed in the ABS depicted in Fig. 7. This behavior carries over to the Gaussian beam in a harmonic potential when the indirect space charge effect is disregarded. However, it is noteworthy that the excited modes are influenced by the choice of chromaticity for the high-intensity beams, contrary to the Gaussian beam with weak space charge forces. For example, only modes 0 to 3 can be excited at $\xi = -1.5$. On the other hand, the modes 4 to 9 appear to be observable at $\xi = -8.0$.

Figure 19 illustrates the relative amplitudes $|a_m|$ obtained by the tracking simulation, in which the harmonic potential model is implemented with the indirect space charge effect disregarded. When the beam intensity is $N_B = 8.6 \times 10^{12}$ ppb (as in Fig. 19b), the lower modes are degenerate, and the correct relative amplitudes for $m = 1, 2$ could not be obtained in the low chromaticity from the tracking simulation due to insufficient tune resolution. The comparison with the corresponding results for the ABS model, excluding the indirect space charge effects (see Fig. 8), shows that the excited modes tend to shift to the lower side of the chromaticity following Eq. (137), although the excitation pattern along the chromaticity remains almost the same between the two cases. This demonstrates the limitations of the ABS model in describing the Gaussian beam. Furthermore, while there are no peaks for the respective modes along the chromaticity axis in the weak space charge beam (refer to Fig. 16), peaks begin to appear as the space charge effect strengthens.

Similar to the ABS model, let us compare the theoretical results from Eq. (93) with the simulations in the harmonic

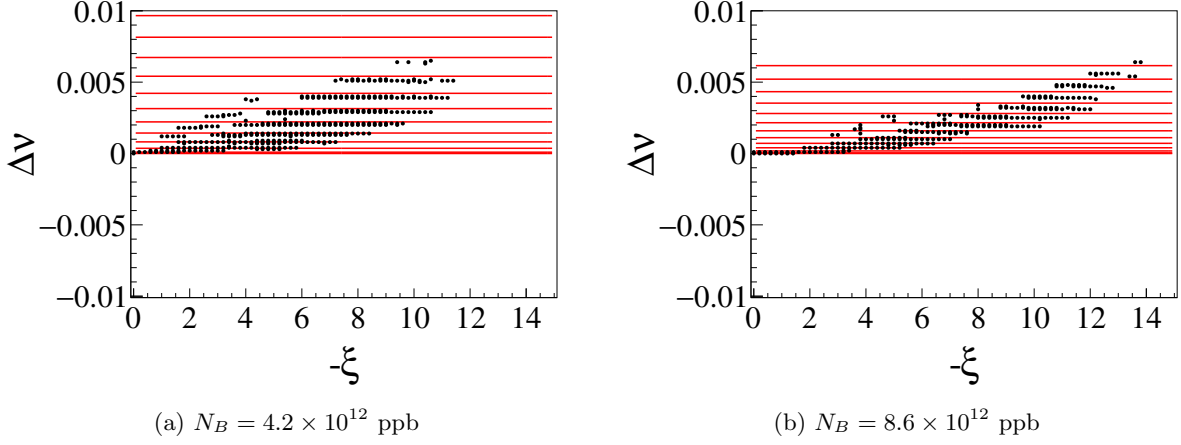


FIG. 18: Head-tail tune spectra in the harmonic potential model without indirect space charge effect for various values of intensity : (a) $N_B = 4.2 \times 10^{12}$ ppb and (b) $N_B = 8.6 \times 10^{12}$ ppb. The dots indicate only the results for $|a_m| > 0.1$. The red lines represent the frequency shifts calculated by Eq. (93) for each head-tail mode in the range of $0 \leq m \leq 12$.

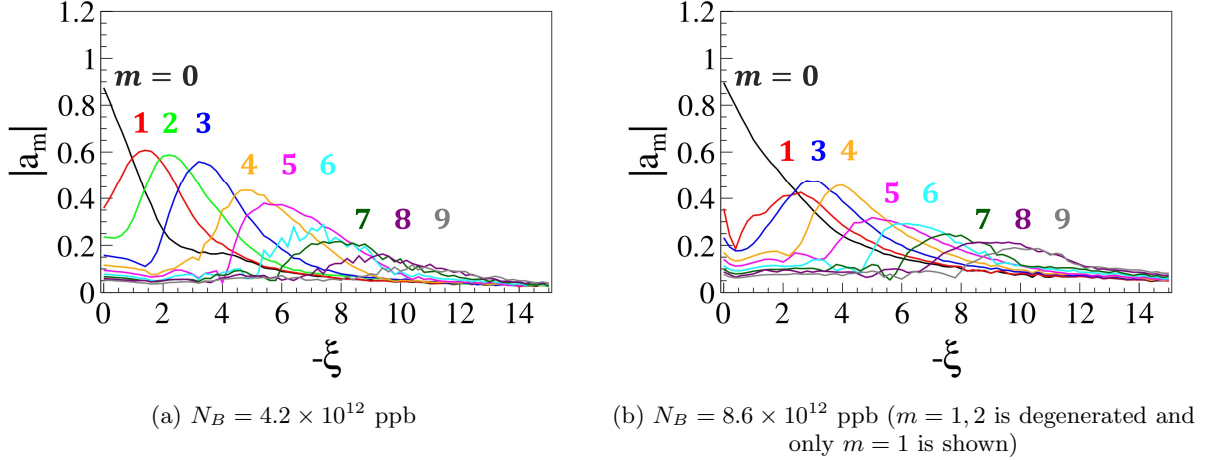


FIG. 19: Relative amplitudes $|a_m|$ tracking simulation of the harmonic potential model without indirect space charge effect. Here, the black, red, (green,) blue, orange, magenta, cyan, dark green, purple, and gray denote the cases of $m = 0, 1, (2,)3, \dots, 9$, respectively.

potential for $\xi = -1.5$ and $\xi = -12.5$. The results are shown in Fig. 20. The theoretical results dealing with only the direct space charge effects in the ABS model explain the tune shift up to $N_B = 1.0 \times 10^{13}$ ppb when no instability occurs and the tune shift due to transverse wakefields is negligible.

F. The tracking simulation with indirect space charge force for the Gaussian beam

Now, let us consider the Gaussian beam, including all space charge forces. Figure 21 shows the intensity dependence of the excited frequency shifts in the bunch for the same set of chromaticity values (ξ) as shown in Fig. 10, where the analytical results of Eq. (93), based on the ABS model, are superimposed. Due to the indirect space charge effects, even large head-tail modes are well separated in the high-intensity beams, even when the chromaticity is large, as observed in the ABS model. However, the degree of separation and the removal of degeneracy in the head-tail modes differ between the Gaussian beam and the ABS model from a quantitative point of view.

The overall behavior of the intensity dependence of the tune shifts can be understood using Eq. (93), which incorporates all space charge effects. However, achieving a perfect fit with the simulation for the Gaussian bunch

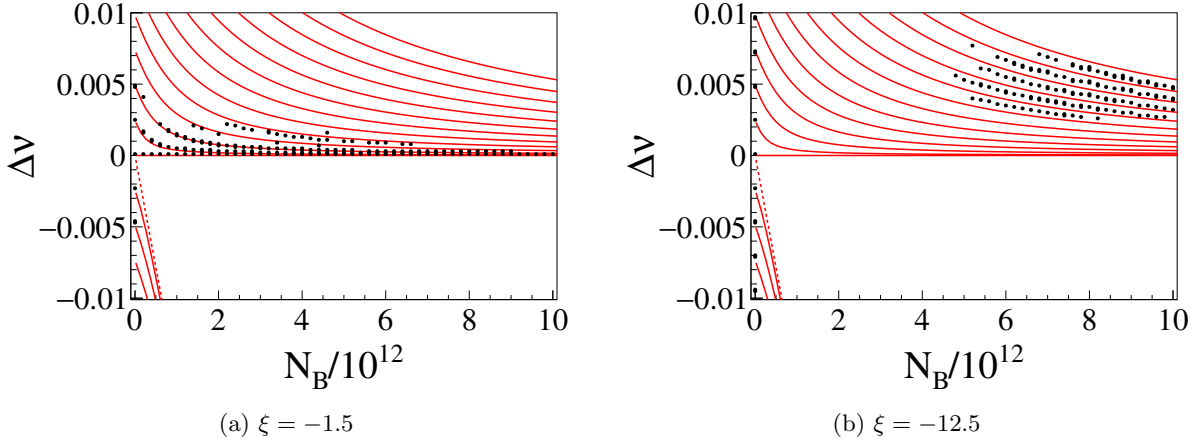


FIG. 20: Head-tail tune spectra in the harmonic potential model without indirect space charge effect and without transverse wake for various values of chromaticity : (a) $\xi = -1.5$ and (b) $\xi = -12.5$. The dots indicate only the results for $|a_m| > 0.1$. The red lines represent the frequency shifts calculated by Eq. (93) for each head-tail mode in the range of $-4 \leq m \leq 12$.

model is impossible because the analytical Eq. (93) is based on the ABS model, and we need to rely on simulation studies.

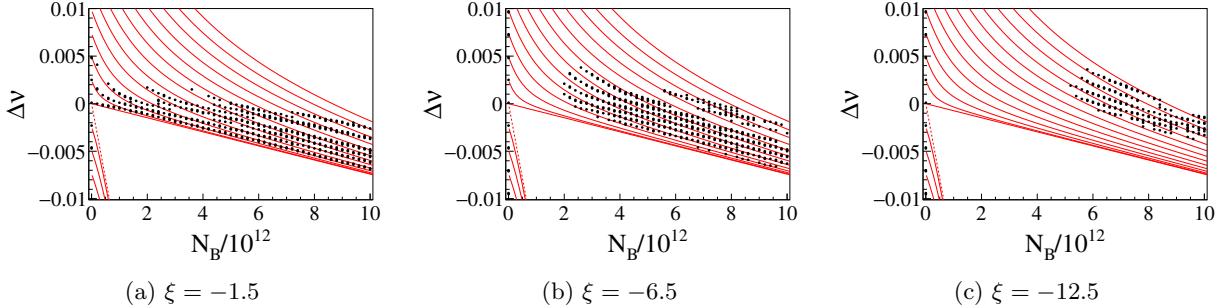


FIG. 21: Head-tail tune spectra in the harmonic potential model with indirect space charge effect for various values of chromaticity : (a) $\xi = -1.5$, (b) $\xi = -6.5$, and (c) $\xi = -12.5$. The dots indicate only the results for $|a_m| > 0.1$. The red lines represent the frequency shifts calculated by Eq. (93) for each head-tail mode in the range of $-4 \leq m \leq 12$.

Figure 22 illustrates the chromaticity dependence of the mode-dependent tune shifts for the high-intensity beams, particularly for (a) $N_B = 4.2 \times 10^{12}$ ppb and (b) $N_B = 8.6 \times 10^{12}$ ppb. The analytical results from Eq. (93) are overlaid on the lines in the figures. As shown in Fig. 22, the chromaticity dependence of the tune shifts diminishes for the respective beam intensities, as was already observed in Fig. 11 for the ABS model cases. Furthermore, we can identify the excitation of specific head-tail modes depending on the chromaticity. For example, only modes $m = 0$ to 5 are observable at $\xi = -1.5$, while modes $m = 4$ to 8 appear at $\xi = -8.0$.

Figure 23 depicts the simulations of the relative amplitudes for the respective head-tail modes for the cases of (a) $N_B = 4.2 \times 10^{12}$ ppb and (b) $N_B = 8.6 \times 10^{12}$ ppb, respectively. In these figures, the black, red, green, blue, orange, magenta, cyan, dark green, purple, and gray curves represent modes $m = 0, 1, 2, \dots, 9$, respectively. The occurrence of these specific excitations can be attributed to the emergence of peaks along the chromaticity axis for the high-intensity beams, as seen in Fig. 23. Similar behavior was also observed in Fig. 19, which includes only the direct space charge effects. The effects of the indirect space charge in Gaussian beams do not significantly alter the excitation pattern of the head-tail modes under the given chromaticity conditions, similar to the behavior observed in the ABS model.

Finally, Fig. 24 summarizes the head-tail frequency shifts from the simulations for four cases: (a) the ABS model without indirect space charge effects, (b) the ABS model including all space charge effects, (c) the harmonic potential model without indirect space charge effects, and (d) the harmonic potential model including all space charge effects.

These figures superimpose the peak positions of each spectrum from Figs. 6, 10, 17, and 21 with dots for the

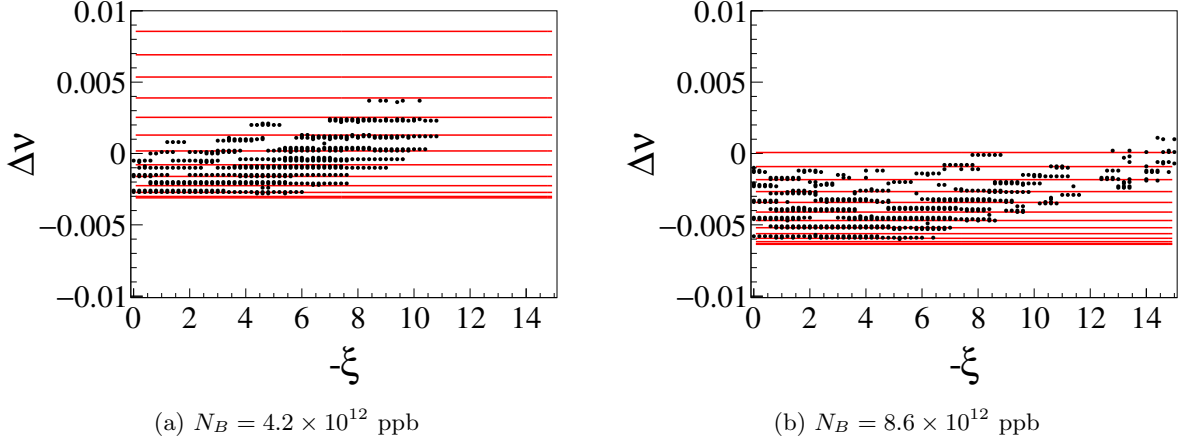


FIG. 22: Head-tail tune spectra in the harmonic potential model with indirect space charge effect for various values of intensity : (a) $N_B = 4.2 \times 10^{12}$ ppb and (b) $N_B = 8.6 \times 10^{12}$ ppb. The dots indicate only the results for $|a_m| > 0.1$. The red lines represent the frequency shifts calculated by Eq. (93) for each head-tail mode in the range of $0 \leq m \leq 12$.

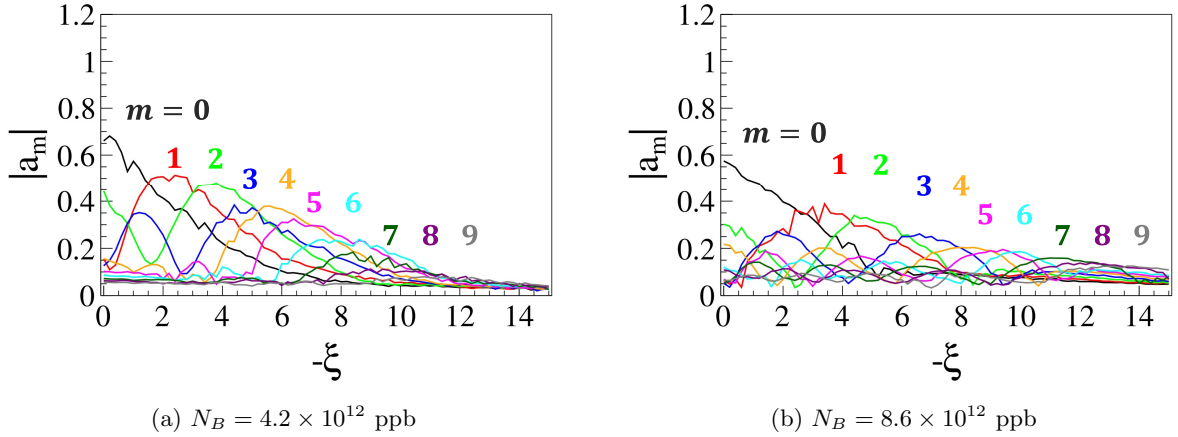


FIG. 23: Relative amplitudes $|a_m|$ tracking simulation of the harmonic potential model with indirect space charge effect. Here, the black, red, green, blue, orange, magenta, cyan, dark green, purple, and gray denote the cases of $m = 0, 1, 2, \dots, 9$, respectively.

chromaticity values $\xi = -1.5, -3.5, -5.5, -6.5, -8.0$, and -12.5 , because the frequency shifts due to the head-tail mode are independent of chromaticity, as previously demonstrated. Analytical results from Eq. (93) are overlaid in all panels by the solid lines.

The frequency shifts for the harmonic potential model including all space charge effects show the deviations from the analytical results. This discrepancy arises due to the limitations of the current theoretical model, as the formula is derived under the assumption of a square-well potential with an airbag beam, rather than a harmonic potential with a Gaussian bunch.

In conclusion, while Eq. (93) provides valuable qualitative insights into the head-tail mode-dependent tune shifts of a high-intensity Gaussian beam, simulation studies are crucial for quantitatively capturing these shifts. This is particularly important for analyzing the impact of the indirect space charge effects on the intensity-dependent tune shifts in the Gaussian beam and the selection of mode excitation patterns, influenced by the direct and indirect space charge effects, under the specified chromaticity.

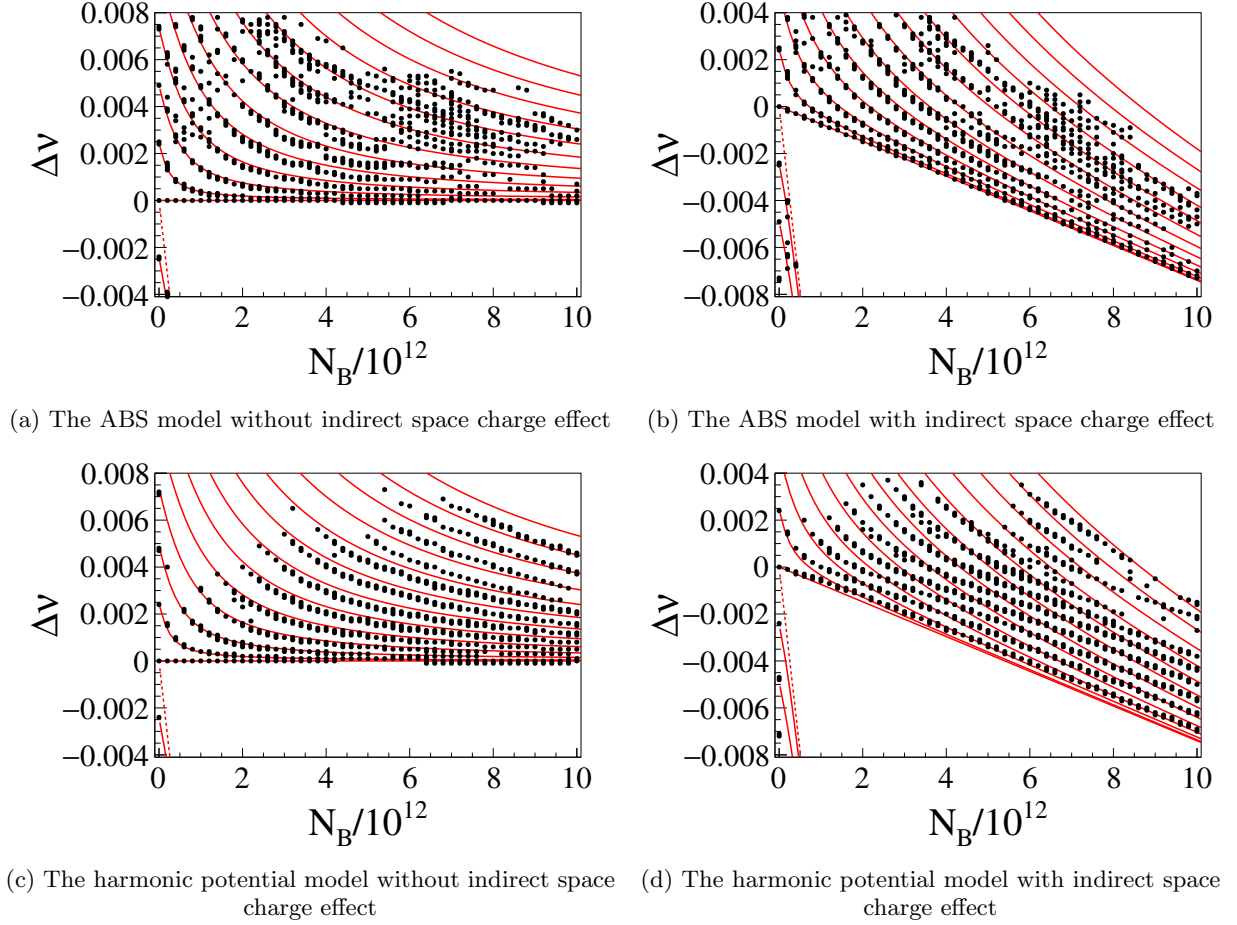


FIG. 24: The tune shift at which the head-tail tune spectrum reaches its maximum peak in the simulation of the beam intensity parameters in Figs. 6, 10, 17, and 21. The dots indicate only the results for $|a_m| > 0.1$. The red lines represent the frequency shifts calculated by Eq. (93) for each head-tail mode in the range of $-3 \leq m \leq 12$.

VIII. TRANSVERSE BUNCH MOTION IN THE TIME DOMAIN IN THE TRACKING SIMULATION

Now, we will observe how the bunch motions in the Gaussian bunch are affected in the time domain by the space charge effects through the chromaticity, the beam intensity, and the synchrotron period by the tracking simulation under the storage mode of the MR.

A. Typical results of the tracking simulation

Figure 25 shows typical results in the time domain of the tracking simulation for the case of strong space charge ($N_B = 8.6 \times 10^{12}$ ppb) with the chromaticity $\xi = -12.5$ and horizontal injection offset $X_0 = 0.01$ m. Figure 25a illustrates that the frequency components of the dipole moment $\Delta^{(k)}$, alternately exhibiting high and low-frequency components along the turn. Meanwhile, Fig. 25b depicts the oscillatory behavior of the horizontal centroid of the entire bunch, representing the decoherent and recoherent motions of the particles comprising the beam. The comparison between Figs. 25a and 25b reveal that when the average transverse position indicates decoherence at the N_f turn (or recoherence at the N_{AM} turn), the intra-bunch frequency in Fig. 25a reaches its maximum (f_{\max}) or minimum, respectively.

To proceed with the following analysis, it is necessary to rigorously define f_{\max} , N_f , and N_{AM} from an observation point of view. This is because the frequency components in Fig. 25a distribute with intensities, and some oscillation peaks can be observed in Fig. 25b, making it challenging to determine these parameters precisely. Since the high-frequency components of the dipole moment are more clearly identifiable in Fig. 25a, N_f is defined as the first turn

number at which the frequency component reaches its highest value with strongest signal (f_{\max}), sweeping from the injection point. Finally, the recoherence period is defined as twice the intra-bunch oscillation period: $N_{\text{AM}} = 2N_f$. In addition, to compare the recoherence period for different synchrotron periods, the normalized recoherence period N_{AM}/N_s is introduced. In the Fig. 25 case, we can determine the maximum intra-bunch frequency $f_{\max} = 84.1$ MHz, the intra-bunch oscillation period $N_f = 890$ turn, the recoherence period $N_{\text{AM}} = 1780$ turn, and the normalized recoherence period $N_{\text{AM}}/N_s = 4.3$, respectively.

Figure 25c reveals that the dipole moment $|\Delta^{(k)}\sigma_{\Delta}/q|$ characteristically meanders back and forth in the longitudinal direction, with this cycle being equal to N_{AM} .

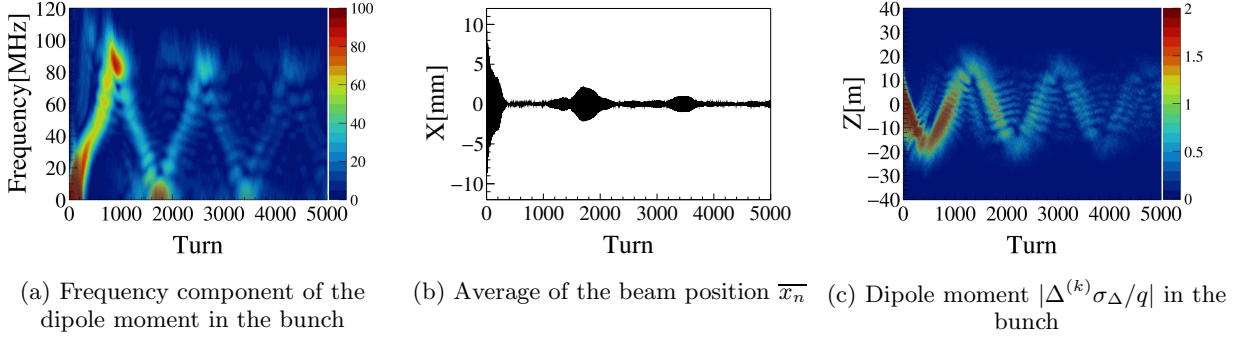


FIG. 25: Transverse bunch motion in the time domain for the chromaticity $\xi = -12.5$ and the beam intensity $N_B = 8.6 \times 10^{12}$ ppb.

B. Modeling of head-tail mode reflecting simulation

To understand the simulation results in Fig. 25, let us simplify the transverse centroid of each segment in the bunch as

$$\bar{x}(n, z) = X_0 \sum_{m=m_{\min}}^{m_{\max}} \tilde{a}_{m,sc}(z) \exp(-i2\pi\nu_m n), \quad (148)$$

where

$$\tilde{a}_{m,sc}(z) = (-i)^m \exp\left(i2\pi\frac{\xi}{\eta C}z\right) \cos\left(m\left(\tan^{-1}\left(\frac{\pi}{2}\frac{z}{\sigma_z}\right) - \frac{\pi}{2}\right)\right), \quad (149)$$

referring to Eq. (103). Here, the factor $\pi/2 \times z/\hat{z}$ is replaced with $\tan^{-1}(\pi/2 \times z/\sigma_z)$ in Eq. (149). The excitation modes specified by m_{\min} and m_{\max} in Eq. (148) are determined by the simulations.

Regarding the tune of the head-tail mode $m \geq 0$, it is assumed to be expressed as

$$\nu_m = \nu_0 + m\Delta\nu, \quad (150)$$

with equal intervals of the head-tail modes $\Delta\nu$, based on the simulation results of Fig. 24d.

Figure 26 shows the dipole moment:

$$\Delta(n, z) = \text{Re}[\bar{x}(n, z)]\rho_z(z), \quad (151)$$

its frequency component, and the average of the beam position $\overline{x_n}$ for the parameter set of $\xi = -12.5$, $m_{\min} = 5$, $m_{\max} = 9$, $\sigma_z = 10$ m, $\Delta\nu = 0.00057$, $\nu_0 = 21.35$, and $X_0 = 1$ mm. Comparing the results to the tracking simulation (Fig. 25), we can observe that the intra-bunch frequency transitions with an interval of N_f between high and low frequencies, the periodic motion occurs at a cycle of $N_{\text{AM}} = 1/\Delta\nu$, and the dipole moment meanders. The analytical model for the simulations reveals that the space charge effects characterize the motions of particles comprising the beam.

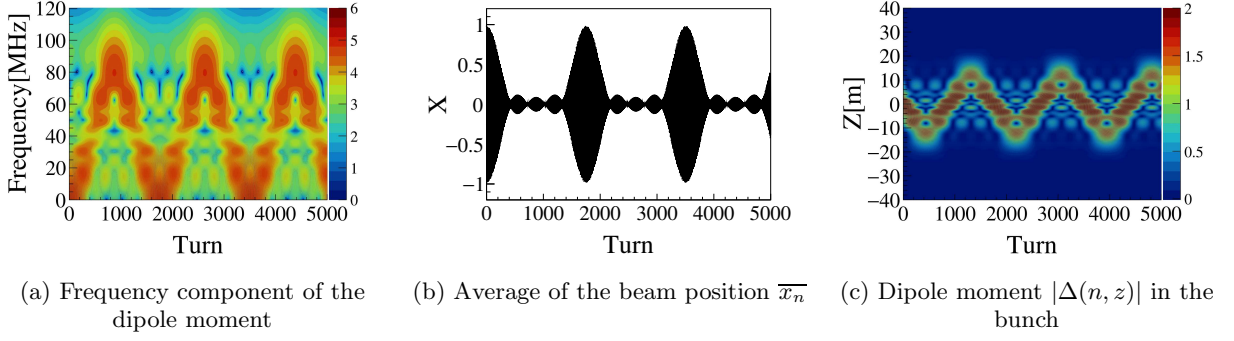


FIG. 26: Transverse bunch motion in the time domain under the condition of $\xi = -12.5$, $m_{\min} = 5$, $m_{\max} = 9$.

To analytically understand this phenomenon, we will extend the upper limit of head-tail mode in Eq. (148) to infinity with $m_{\min} = 0$. The transverse centroid of each segment is simplified as

$$\begin{aligned}
 & \bar{x}(n, z) / \exp(-i2\pi\nu_0 n) \\
 &= X_0 \exp\left(i2\pi \frac{\xi}{\eta C} z\right) \sum_{m=0}^{\infty} \exp\left(-im(2\pi\Delta\nu n + \frac{\pi}{2})\right) \cos\left(m\left(\tan^{-1}\left(\frac{\pi}{2} \frac{z}{\sigma_z}\right) - \frac{\pi}{2}\right)\right) \\
 &= X_0 \exp\left(i2\pi \frac{\xi}{\eta C} z\right) \frac{1}{2} \left(1 + \frac{1}{1 + \exp(i(\tan^{-1}(\frac{\pi}{2} \frac{z}{\sigma_z}) - 2\pi\Delta\nu n))} - \frac{1}{1 - \exp(i(\tan^{-1}(\frac{\pi}{2} \frac{z}{\sigma_z}) + 2\pi\Delta\nu n))}\right).
 \end{aligned} \tag{152}$$

The last term characterized by $\Delta\nu$ diverges around

$$z = \begin{cases} -\frac{2}{\pi}\sigma_z \tan(2\pi\Delta\nu n), & \text{for } 0 < n < \frac{1}{4}N_{AM}, \frac{3}{4}N_{AM} < n < N_{AM}, \\ +\frac{2}{\pi}\sigma_z \tan(2\pi\Delta\nu n), & \text{for } \frac{1}{4}N_{AM} < n < \frac{3}{4}N_{AM}, \end{cases} \tag{153}$$

in the range of $0 < n < N_{AM}$, explaining the meandering of the dipole moments along the turn numbers, owing to the space charge effects.

Referring to the derivation of Eq. (22), we focus on the phase component of Eq. (152) to analyze the dependence of the maximum intra-bunch frequency on chromaticity, including the effects of space charge. First, we calculate $\text{Arg}[\bar{x}(n, z) / \exp(-i2\pi\nu_0 n)]$ after substituting $n = N_{AM}/2$ into Eq. (152) for small z , resulting in

$$\begin{aligned}
 & \text{Arg}\left[\bar{x}\left(\frac{N_{AM}}{2}, z\right) / \exp\left(-i2\pi\nu_0 \frac{N_{AM}}{2}\right)\right] - 2\pi \frac{\xi}{\eta C} z \\
 &= \text{Arg}\left[\sum_{m=m_{\min}}^{m_{\max}} i^m \cos\left(m\left(\tan^{-1}\left(\frac{\pi}{2} \frac{z}{\sigma_z}\right) - \frac{\pi}{2}\right)\right)\right] \\
 &\simeq \text{Arg}\left[\sum_{\substack{m_{\min} \leq m \leq m_{\max} \\ m:\text{even}}} (+1) + i \sum_{\substack{m_{\min} \leq m \leq m_{\max} \\ m:\text{odd}}} m \frac{\pi}{2} \frac{z}{\sigma_z}\right].
 \end{aligned} \tag{154}$$

Here, the second term can be estimated by referring to the condition on $\text{Arg}[\bar{x}(n, z) / \exp(-i2\pi\nu_0 n)]$ at $n = 0$ for small z , which must be zero due to the very initial condition. As a result, this condition is explicitly expressed by

$$\begin{aligned}
 & \text{Arg}[\bar{x}(0, z) / \exp(-i2\pi\nu_0 0)] - 2\pi \frac{\xi}{\eta C} z \\
 &= \text{Arg}\left[\sum_{m=m_{\min}}^{m_{\max}} (-i)^m \cos\left(m\left(\tan^{-1}\left(\frac{\pi}{2} \frac{z}{\sigma_z}\right) - \frac{\pi}{2}\right)\right)\right] \\
 &\simeq \text{Arg}\left[\sum_{\substack{m_{\min} \leq m \leq m_{\max} \\ m:\text{even}}} (+1) - i \sum_{\substack{m_{\min} \leq m \leq m_{\max} \\ m:\text{odd}}} m \frac{\pi}{2} \frac{z}{\sigma_z}\right].
 \end{aligned} \tag{155}$$

By combining the complex conjugate of Eq. (155) with Eq. (154), we derive

$$\text{Arg} \left[\bar{x} \left(\frac{N_{\text{AM}}}{2}, z \right) / \exp \left(-i2\pi\nu_0 \frac{N_{\text{AM}}}{2} \right) \right] \simeq 4\pi \frac{\xi}{\eta C} z. \quad (156)$$

Finally, the maximum value of f_{int} at the center of the bunch is given by

$$f_{\text{max}} = f_{\text{int}} \left(\frac{N_{\text{AM}}}{2} \right) \simeq \left| \frac{1}{2\pi} \frac{d}{dt} \left[2\pi\nu_0 \frac{N_{\text{AM}}}{2} - 4\pi \frac{\xi}{\eta C} z \right] \right| = \left| 2f_0 \frac{\xi}{\eta} \right|, \quad (157)$$

which matches Eq. (22) in the absence of space charge effects. The validity of this approximate formula including the space charge effect will be discussed in Sec. VIII E.

In the end, the simulations featuring the meandering of the dipole moment, the maximum intra-bunch frequency, and the recoherence of the entire bunch frequency can be roughly understood by the analytical model for the given excited head-tail modes m_{min} and m_{max} under the chromaticity condition.

C. Synchrotron period dependence

Let us observe the synchrotron tune ν_s dependence on the frequency component of the dipole moment, the horizontal centroid of the entire bunch, and the dipole moment along the turn number by changing the RF voltage, following Eq. (8). First, we scan the RF voltages $V_{\text{RF}} = 80, 110, 140, 200, 263,$ and 400 kV, with fixed chromaticity, and the beam intensity. These RF voltages correspond to the synchrotron period $N_s = 760, 650, 570, 480, 410,$ and 340 turns, respectively. Figure 27 shows the transverse bunch motion in the time domain for $V_{\text{RF}} = 400, 263,$ and 110 kV with the chromaticity $\xi = -6.5$, and the beam intensity $N_B = 4.2 \times 10^{12}$ ppb. Following the procedure explained in Sec. VIII A, the maximum intra-bunch frequency f_{max} and the recoherence period N_{AM} can be determined to be $f_{\text{max}} = 43.5$ MHz, $N_{\text{AM}} = 1700$, for $V_{\text{RF}} = 400$ kV; $f_{\text{max}} = 39.6$ MHz, $N_{\text{AM}} = 1720$, for $V_{\text{RF}} = 263$ kV; and $f_{\text{max}} = 34.2$ MHz, $N_{\text{AM}} = 2940$, for $V_{\text{RF}} = 110$ kV.

Figure 28 shows the synchrotron period dependence of the maximum intra-bunch frequency f_{max} and the normalized recoherence period N_{AM}/N_s . No significant dependence on the synchrotron period is observed in the maximum intra-bunch frequency f_{max} . Moreover, when the space charge effect is stronger ($N_B = 4.2 \times 10^{12}$ and 8.6×10^{12} ppb), the normalized recoherence period stays within the region of $4N_s < N_{\text{AM}} < 5N_s$ even when the synchrotron period is changed. Meanwhile, when the space charge effect is moderate ($N_B = 2.4 \times 10^{12}$ ppb), the normalized recoherence period tends to increase as the synchrotron period increases.

This behavior of the recoherence period can be understood in terms of the head-tail modes analysis. Figure 29 shows the head-tail tune spectrum of the relative amplitude a_m , where the synchrotron period is scanned by changing the RF voltage in the tracking simulation. The vertical axis is the head-tail modes tune normalized by the synchrotron tune: $\Delta\nu/\nu_s$. In Figs. 29b and 29c (in the cases of the strong space charge effect with the respective beam intensities $N_B = 4.2 \times 10^{12}$ and 8.6×10^{12} ppb), we can see that the normalized frequency interval between adjacent head-tail modes is close to a constant of around $0.2 < \Delta\nu/\nu_s < 0.25$, even when the synchrotron period is changed. On the other hand, in Fig. 29a (in the case of the moderate space charge effect with the beam intensity $N_B = 2.4 \times 10^{12}$ ppb), the interval dynamically decreases from 0.5 to 0.25 as the synchrotron period increases. As a result, we can conclude that the normalized recoherence period saturates for the higher synchrotron tune due to the space charge effects.

D. Beam intensity dependence

Next, we observe the beam intensity dependence of intra-bunch motions for a fixed RF voltage $V_{\text{RF}} = 263$ kV and chromaticity. Figure 30 shows the simulations of the transverse bunch motion in the time domain for the beam intensity: $N_B = 1.0 \times 10^{12}, 2.4 \times 10^{12}, 4.2 \times 10^{12},$ and 8.6×10^{12} ppb with fixed chromaticity $\xi = -8.0$. After analyzing those data, the maximum intra-bunch frequency f_{max} and the recoherence period N_{AM} can be determined to be $f_{\text{max}} = 53.3$ MHz, $N_{\text{AM}} = 340$, for $N_B = 1.0 \times 10^{12}$ ppb; $f_{\text{max}} = 49.0$ MHz, $N_{\text{AM}} = 600$, for $N_B = 2.4 \times 10^{12}$ ppb; $f_{\text{max}} = 51.3$ MHz, $N_{\text{AM}} = 1040$, for $N_B = 4.2 \times 10^{12}$ ppb; and $f_{\text{max}} = 53.7$ MHz, $N_{\text{AM}} = 1860$, for $N_B = 8.6 \times 10^{12}$ ppb. When the space charge effect is negligible, the recoherence occurs at $N_{\text{AM}} = N_s$ seen in Fig. 43 in Appendix D. However, for the moderate beam intensity in Fig. 30e, the recoherence signals weaken due to the betatron tune spread caused by the space charge effects. In contrast, as the beam intensity increases significantly, the strong space charge effects bias the particle distributions within the beam, leading to the reemergence of recoherence, as illustrated in Figs. 30g and 30h.

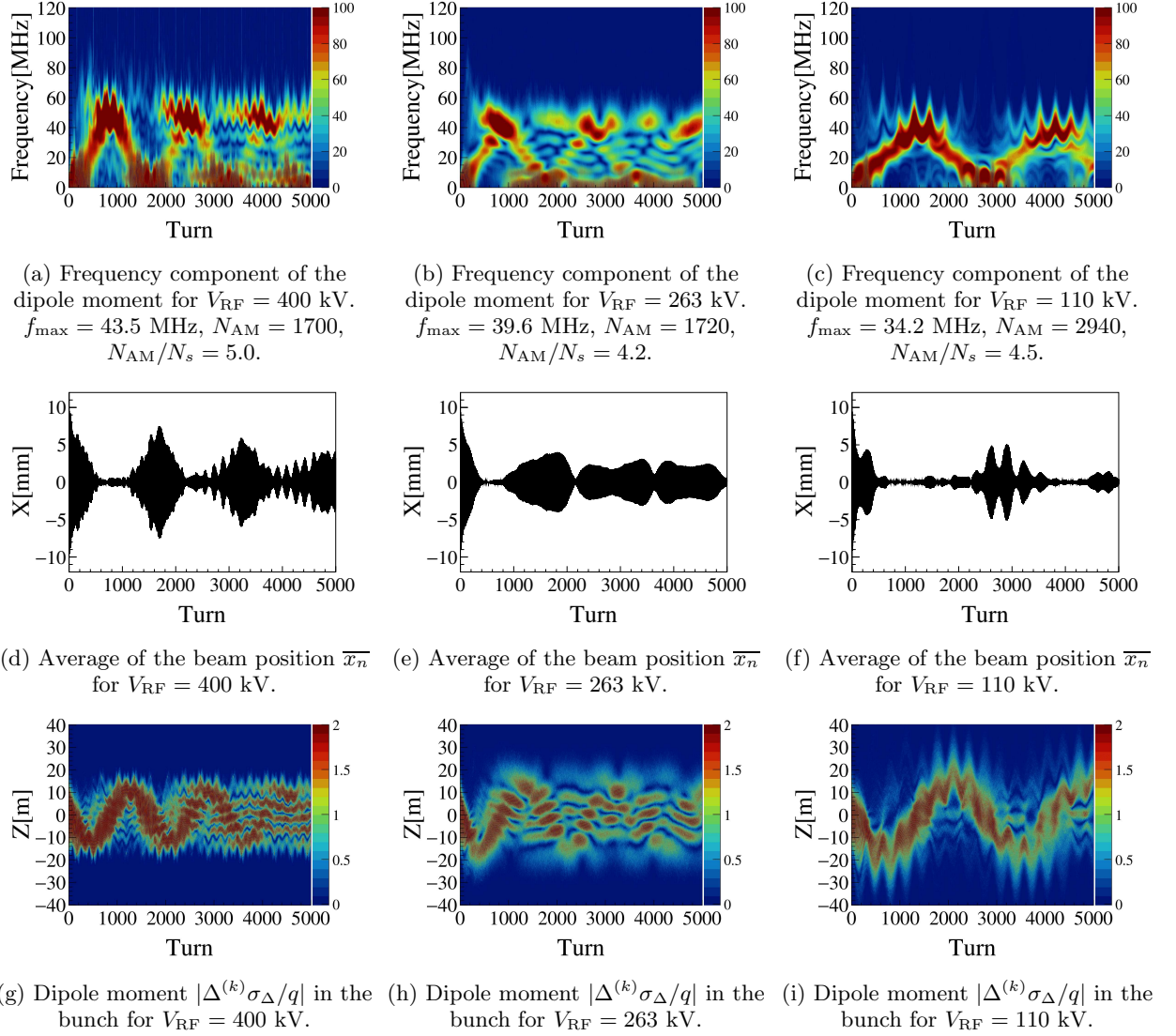


FIG. 27: Transverse bunch motion in the time domain for the RF voltages: $V_{\text{RF}} = 110, 263,$ and 400 kV with the chromaticity $\xi = -6.5$ and the beam intensity $N_B = 4.2 \times 10^{12}$ ppb.

Figure 31 shows the normalized recoherence period N_{AM}/N_s for the beam intensity. As the beam intensity increases, the normalized recoherence period tends to increase. This feature can be interpreted based on the tune spectrum results shown in Fig. 21, similar to the discussion in the previous subsection. When the separation of the excited tune shifts across different modes remains nearly identical within the given range of beam intensities, the normalized recoherence period becomes independent of the beam intensity.

For lower chromaticity, the lower head-tail modes are excited, and their degeneration levels rapidly saturate at high beam intensities. In contrast, for higher chromaticity, the higher head-tail modes are excited, and their degeneration levels do not saturate easily, even at high beam intensities.

As a result, achieving saturation of the normalized recoherence period for these beam intensity parameters requires a higher beam intensity in the higher chromaticity condition. In the end, the recoherence period is within $4N_s < N_{\text{AM}} < 5N_s$ for the high-intensity beams. In the MR, the recoherence period is expected to lengthen to $1600 < N_{\text{AM}} < 2000$ due to the space charge effects for a beam characterized by the equal intervals of the head-tail modes $\Delta\nu$, within the range of $0.0005 < \Delta\nu < 0.0006$, based on the simulation results of Fig. 24d.

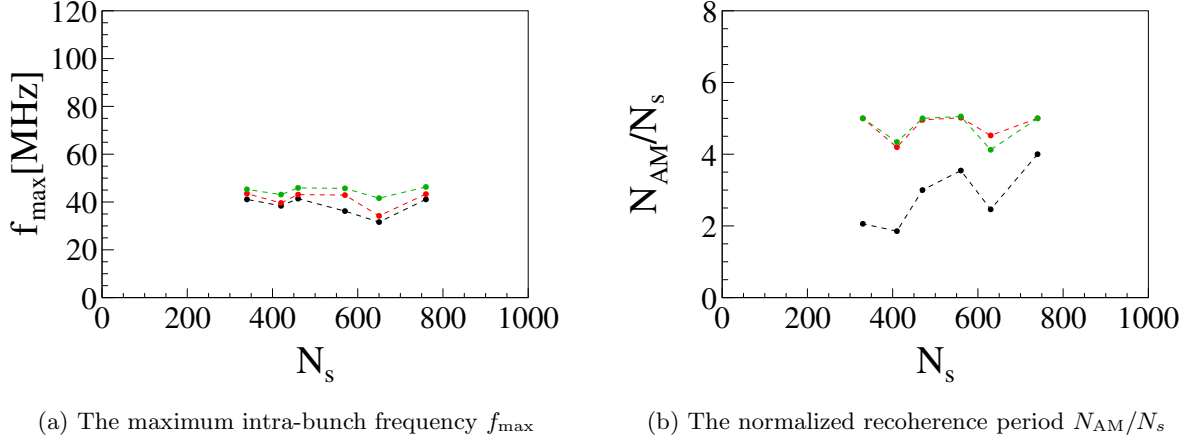


FIG. 28: The maximum intra-bunch frequency f_{\max} and the normalized recoherence period N_{AM}/N_s for the synchrotron period. Here, the black, red, and green denote the cases of $N_B = 2.4 \times 10^{12}$, 4.2×10^{12} , and 8.6×10^{12} ppb, respectively.

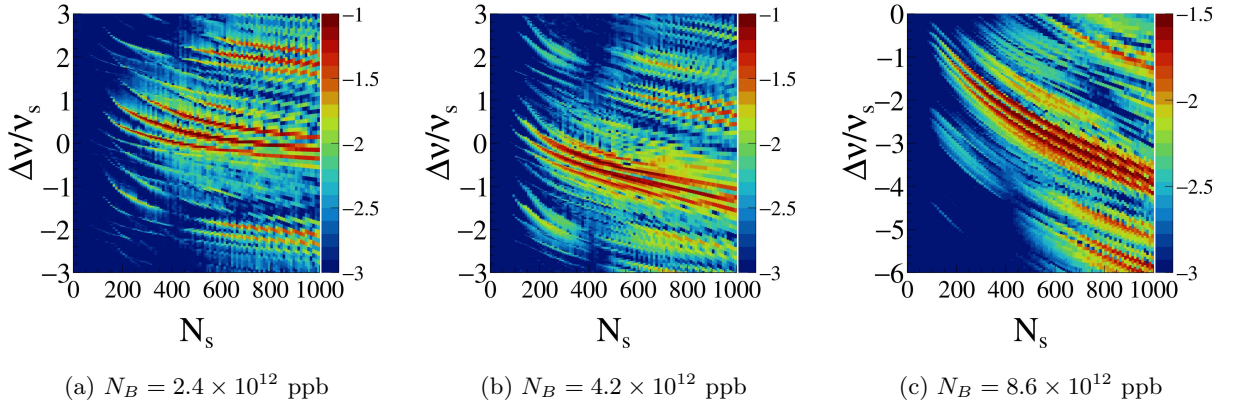


FIG. 29: The spectra of head-tail tune normalized with synchrotron tune $\Delta\nu/\nu_s$ for the synchrotron period obtained by analyzing $\log |a_m|$ of the harmonic model with the indirect space charge effect.

E. Chromaticity dependence

Finally, we simulate the case where the chromaticity is scanned for the parameters described in the previous subsection. Figure 32 shows the transverse bunch motion in the time domain for the chromaticity: $\xi = -1.5, -8.0$, and -12.5 with the fixed beam intensity $N_B = 4.2 \times 10^{12}$ ppb. After those data are analyzed, the maximum intra-bunch frequency f_{\max} and the recoherence period N_{AM} can be determined to be $f_{\max} = 9.5$ MHz, $N_{AM} = 1940$, for $\xi = -1.5$; $f_{\max} = 51.3$ MHz, $N_{AM} = 1040$, for $\xi = -8.0$; and $f_{\max} = 76.5$ MHz, $N_{AM} = 660$, for $\xi = -12.5$.

Figure 33 shows the maximum intra-bunch frequency f_{\max} for the chromaticity. Regardless of the space charge effect, it is clear that the maximum intra-bunch frequency follows $f_{\max} = 6.4|\xi|$ MHz (refer to Eq. (157), identical to Eq. (22) derived under the assumption of weak space charge effects.) and is proportional to the chromaticity.

IX. BEAM MEASUREMENTS

In this section, we examine the intra-bunch motion predicted by the tracking simulation in the previous section by changing the chromaticity, the synchrotron period, and the beam intensity in the storage mode of the MR from a measurement point of view. We analyze the horizontal centroid of the entire bunch, the dipole moment in the bunch, and its intra-bunch frequency for each turn, when beams are injected into the MR with the horizontal offset of about $X_0 = 5$ mm.

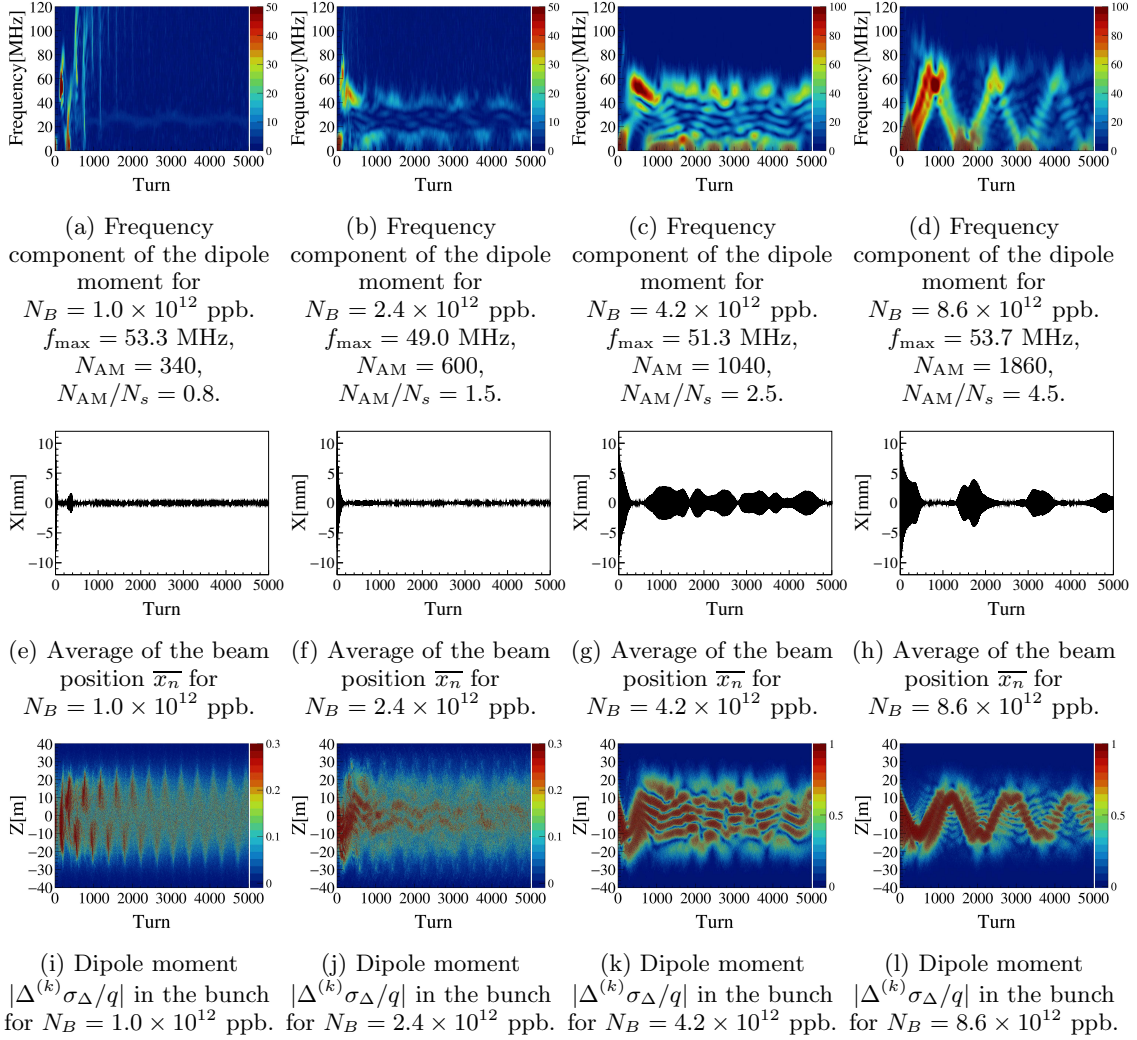


FIG. 30: Transverse bunch motion in the time domain for the beam intensity: $N_B = 1.0 \times 10^{12}, 2.4 \times 10^{12}, 4.2 \times 10^{12}$ and 8.6×10^{12} ppb with the chromaticity $\xi = -8.0$, and the RF voltage $V_{RF} = 263$ kV.

For the measurement, we use data with a 500 MHz sampling rate detected by the stripline beam position monitor comprising two pairs of triangle-shaped electrodes [45], installed in the MR to secure a wide-band frequency for the IBFB.

In our measurement, the horizontal dipole moments, $\Delta(z)$, consisting of the bunch, are obtained by integrating the difference signals from the horizontal pair of electrodes within the specified time. The horizontal centroid of the entire bunch \bar{x}_n is then calculated by summing all dipole moments in the bunch and multiplying the result by the sensitivity coefficient, 0.046 m, divided by the measured bunch current.

In the 3 GeV storage mode with a single bunch, when the repetition period is 1.36 s, the beam power corresponds to $0.35 \times N_B/10^{12}$ kW.

A. Conditions of measurements

First, we observe the synchrotron tune dependence by scanning the RF voltages $V_{RF} = 80, 110, 140, 200, 263$ kV, and 400 kV and the beam intensities $N_B = 2.4 \times 10^{12}, 4.2 \times 10^{12}$, and 8.6×10^{12} ppb with the fixed chromaticity $(\xi_x, \xi_y) = (-6.5, -7.4)$ and the betatron tune $(\nu_{\beta,x}, \nu_{\beta,y}) = (21.35, 21.41)$. Table I summarizes the number of measured shots for the analysis.

Next, we investigate the beam intensity and chromaticity dependences by scanning the protons per bunch $N_B = 1.0 \times 10^{12}, 2.4 \times 10^{12}, 4.2 \times 10^{12}$, and 8.6×10^{12} ppb; and the horizontal chromaticities $\xi_x = -1.5, -7.9$, and -12.5 ;

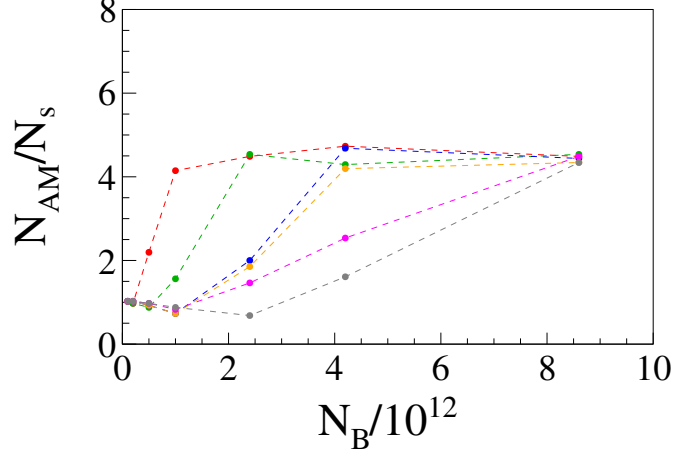


FIG. 31: The normalized recoherence period N_{AM}/N_s with several fixed chromaticities for different beam intensities. Here, the red, green, blue, orange, magenta, and gray denote the cases of $\xi = -1.5, -3.5, -5.5, -6.5, -8.0,$ and $-12.5,$ respectively.

TABLE I: Number of shots for the analysis of the synchrotron period dependence with the fixed chromaticity $(\xi_x, \xi_y) = (-6.5, -7.4)$ and the betatron tune $(\nu_{\beta,x}, \nu_{\beta,y}) = (21.35, 21.41)$.

$N_B[\text{ppb}]/10^{12}$	2.4	4.2	8.6
$N_s = 340$	3	3	3
$N_s = 410$	3	3	3
$N_s = 480$	-	3	3
$N_s = 570$	-	3	1
$N_s = 650$	-	4	1
$N_s = 760$	3	2	1

with the fixed vertical chromaticity $\xi_y = -15$, the betatron tune $(\nu_{\beta,x}, \nu_{\beta,y}) = (21.35, 21.41)$, and the RF voltage $V_{RF} = 263$ kV equivalent to the synchrotron period $N_s = 410$. For the above two conditions, the measured bunching factor at the injection time was $B_f = 0.017$ for the beam intensity $N_B \leq 4.2 \times 10^{12}$ ppb, and $B_f = 0.022$ for the beam intensity $N_B = 8.6 \times 10^{12}$ ppb.

As the other choice, we scan the beam intensities $N_B = 1.3 \times 10^{11}, 2.5 \times 10^{11}, 5.0 \times 10^{11}, 1.0 \times 10^{12}, 2.4 \times 10^{12},$ and 4.2×10^{12} ppb; and the chromaticities $(\xi_x, \xi_y) = (-5.7, -6.2)$ and $(-3.3, -4.4)$; with the fixed betatron tune $(\nu_x, \nu_y) = (22.30, 20.81)$ and the RF voltage $V_{RF} = 155$ kV, corresponding to the synchrotron period $N_s = 540$ turn. For this condition, the bunching factor at the injection timing was $B_f = 0.022$ for all beam intensities. Tables II and III summarize the number of shots for the analysis, respectively.

TABLE II: Number of shots for the analysis of the beam intensity and the chromaticity dependences with the fixed betatron tune $(\nu_{\beta,x}, \nu_{\beta,y}) = (21.35, 21.41)$, and the RF voltage $V_{RF} = 263$ kV.

$N_B[\text{ppb}]/10^{12}$	1.0	2.4	4.2	8.6
$\xi_x = -1.5$	30	30	30	-
$\xi_x = -7.9$	30	30	30	10
$\xi_x = -12.5$	30	30	30	-

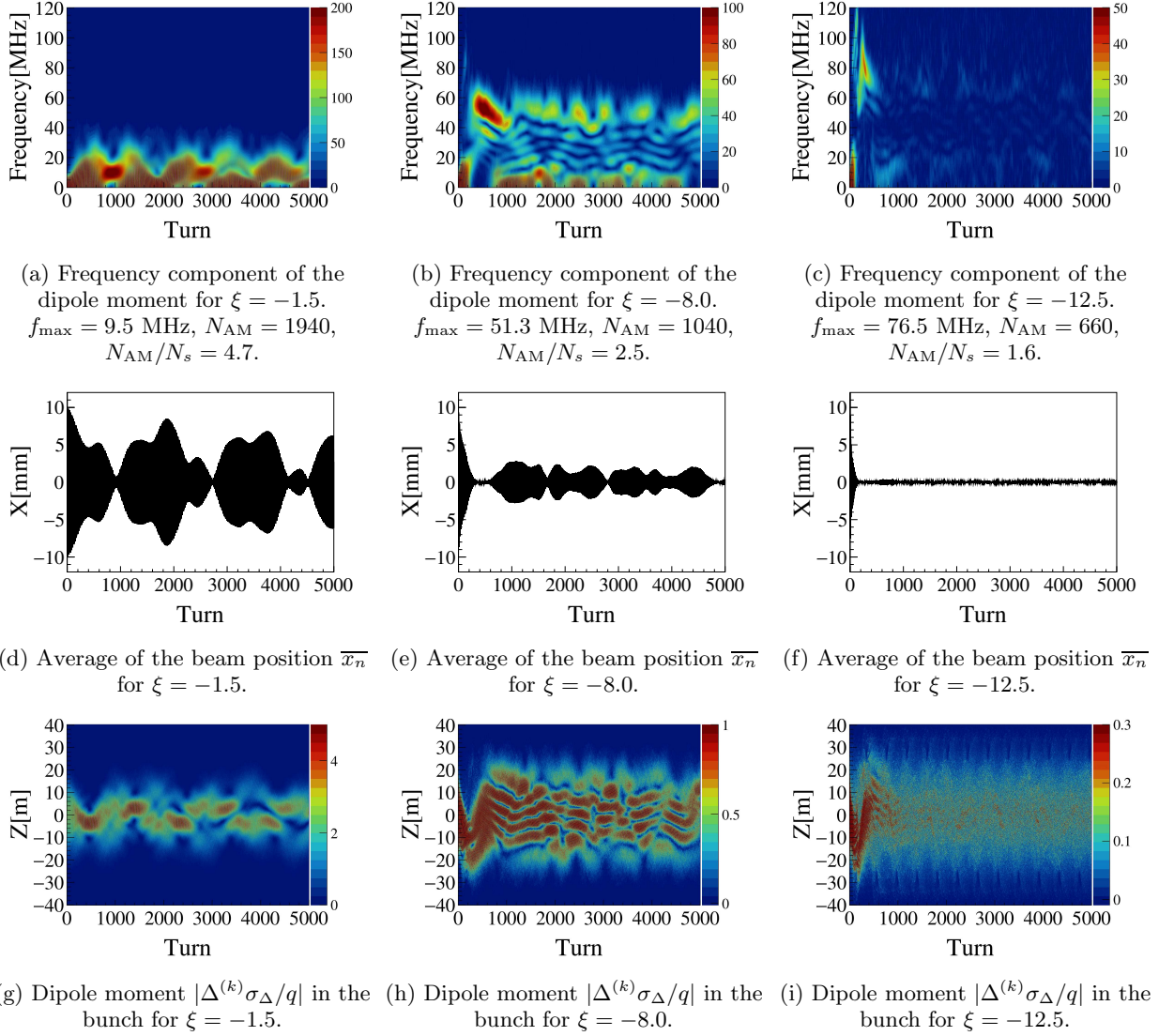


FIG. 32: Transverse bunch motion in the time domain for the chromaticity: $\xi = -1.5, -8.0$, and -12.5 with the beam intensity $N_B = 4.2 \times 10^{12}$ ppb and the RF voltage $V_{\text{RF}} = 263$ kV.

TABLE III: Number of shots for the analysis of the beam intensity and the chromaticity dependences with the fixed betatron tune $(\nu_x, \nu_y) = (22.30, 20.81)$, and the RF voltage $V_{\text{RF}} = 155$ kV.

$N_B[\text{ppb}]/10^{12}$	0.13	0.26	0.52	1.0	2.4	4.2
$\xi_x = -3.3$	3	3	3	3	3	-
$\xi_x = -5.7$	3	3	3	3	3	3

B. Analysis of beam measurements

1. Synchrotron period dependence

First, we observe the synchrotron tune ν_s dependence on the frequency component of the dipole moment, the horizontal centroid of the entire bunch, and the dipole moment along the turn number, based on the measured shots described in Table I. Figure 34 shows the transverse bunch motion in the time domain for $V_{\text{RF}} = 400, 263$ and 110 kV with the chromaticity $\xi = -6.5$ and the beam intensity $N_B = 4.2 \times 10^{12}$ ppb. This is the same parameter set as Fig.

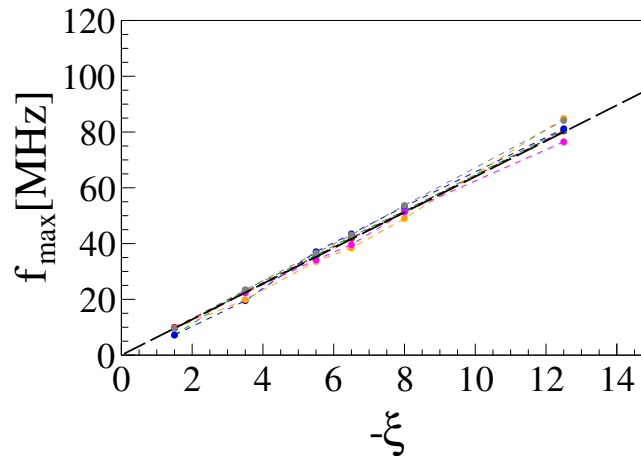


FIG. 33: The maximum intra-bunch frequency f_{\max} with fixed beam intensity for different chromaticities. Here, the black, red, green, blue, orange, magenta, and gray denote the cases of $N_B = 1.0 \times 10^{11}, 2.0 \times 10^{11}, 5.0 \times 10^{11}, 1.0 \times 10^{12}, 2.4 \times 10^{12}, 4.2 \times 10^{12},$ and 8.6×10^{12} ppb, respectively. The black dashed line is the result of Eq. (157).

27. The simulations effectively explain the major characteristics of the measurements, including the periodic behavior of the high-frequency components of the dipole moment and the lengthening of the recoherence period in the high-intensity beams. Following the procedure explained in Sec. VIII A, the maximum intra-bunch frequency f_{\max} and the recoherence period N_{AM} can be respectively determined to be $f_{\max} = 43.3$ MHz, $N_{\text{AM}} = 1600$, for $V_{\text{RF}} = 400$ kV; $f_{\max} = 45.3$ MHz, $N_{\text{AM}} = 2300$, for $V_{\text{RF}} = 263$ kV; and $f_{\max} = 39.8$ MHz, $N_{\text{AM}} = 3400$, for $V_{\text{RF}} = 110$ kV.

After the comprehensive analysis, Fig. 35 shows the synchrotron period dependence of the maximum intra-bunch frequency f_{\max} and the normalized recoherence period N_{AM}/N_s on the synchrotron period N_s . The results are quite consistent with the simulations in Fig. 28a and Eq. (157) indicating no synchrotron tune dependence of the maximum intra-bunch frequency.

For the normalized recoherence period, the simulations with the fixed initial condition for different beam intensities suggest that the normalized recoherence period saturates and is independent of the synchrotron period for high-intensity beams, as shown in Fig. 28b.

On the other hand, though the measured data reveals that the normalized recoherence period remains within the range $4N_s < N_{\text{AM}} < 7N_s$, and no significant dependence on the measured beam intensities is observed for the synchrotron period varying from approximately 300 to 800, the data for $N_B = 2.4 \times 10^{12}$ and 4.2×10^{12} ppb almost overlap, while the data for $N_B = 8.6 \times 10^{12}$ ppb deviates from the others, as shown in Fig. 35b.

These results indicate that the recoherence period already saturates in the mid-strength region of the space charge, suggesting that the current modeling of the indirect space charge, based on the simplified geometry of the MR, overestimates its effect on the intra-bunch motions. Meanwhile, the reason the normalized recoherence period falls below the saturated value for beams with mid-strength space charge is that the injected beam is broadened from the outset due to the large number of N_B . Note, $B_f = 0.017$ for $N_B \leq 4.2 \times 10^{12}$ ppb, but $B_f = 0.022$ for $N_B = 8.6 \times 10^{12}$ ppb in the measurements. Consequently, the effective space charge effect is mitigated in the bunch with $N_B = 8.6 \times 10^{12}$ ppb, leading to a shorter normalized recoherence period compared to the other results.

2. Beam intensity dependence

Now, we have experimentally confirmed that the synchrotron period doesn't have a strong effect on the maximum intra-bunch frequency and the normalized recoherence period N_{AM}/N_s . We handle data with different synchrotron periods (RF voltages) simultaneously, from now on. Accordingly, we will analyze the beam intensity and the chromaticity dependences after combining the results of Tables I, II, and III.

Figure 36 shows the measurements of the transverse bunch motion in the time domain for the beam intensity: $N_B = 1.0 \times 10^{12}, 2.4 \times 10^{12}, 4.2 \times 10^{12},$ and 8.6×10^{12} ppb with fixed chromaticity $\xi = -8.0$, displaying the low to high-intensity beam results in left to right columns. Just as in the simulation predictions, the recoherence signal becomes more visible when the beam intensity increases. After analyzing those data, the maximum intra-bunch

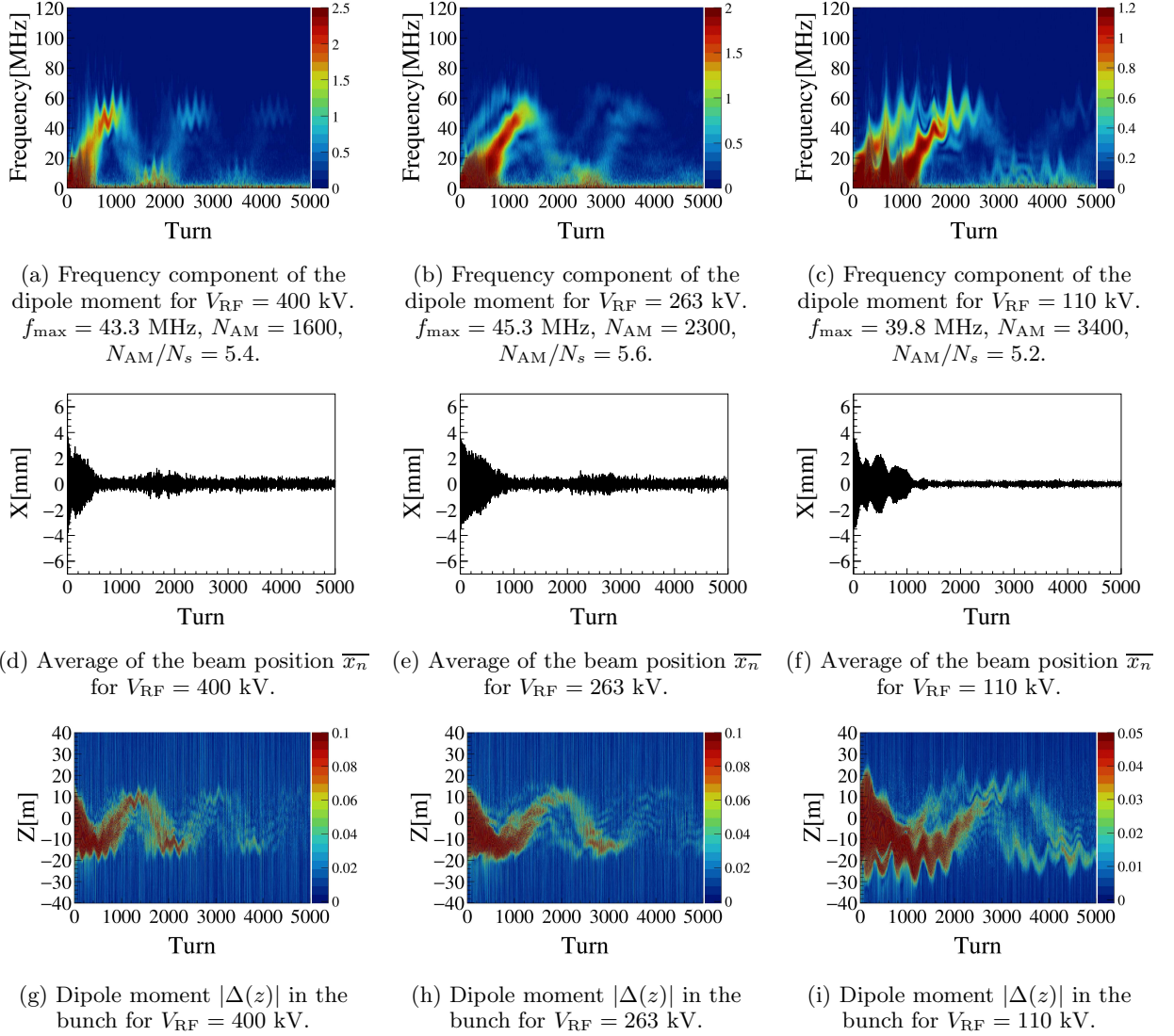


FIG. 34: Transverse bunch motion in the time domain for the RF voltages: $V_{\text{RF}} = 110, 263,$ and 400 kV with the chromaticity $\xi = -6.5$ and the beam intensity $N_B = 4.2 \times 10^{12}$ ppb.

frequency f_{max} and the recoherence period N_{AM} can be determined to be $f_{\text{max}} = 50.5$ MHz, $N_{\text{AM}} = 1300$, for $N_B = 1.0 \times 10^{12}$ ppb; $f_{\text{max}} = 52.2$ MHz, $N_{\text{AM}} = 2200$, for $N_B = 2.4 \times 10^{12}$ ppb; $f_{\text{max}} = 51.9$ MHz, $N_{\text{AM}} = 2100$, for $N_B = 4.2 \times 10^{12}$ ppb; and $f_{\text{max}} = 53.4$ MHz, $N_{\text{AM}} = 1700$, for $N_B = 8.6 \times 10^{12}$ ppb.

Figure 37 shows the normalized recoherence period for the beam intensity, corresponding to the simulations in Fig. 31. From a measurement perspective, it is challenging to identify N_f , where the highest frequency: f_{max} appears in the bunch with lower intensity under conditions of lower chromaticity like $\xi = -1.5$. From a theoretical viewpoint, this difficulty arises because multiple lower head-tail modes with different mode differences are simultaneously excited in the low-intensity beam at the lower chromaticity setting as explained in Sec. VII F. This makes it difficult to define the recoherence period, N_{AM} . As a result, we exclude the measurement point or the case of $N_B = 1.0 \times 10^{12}$ ppb with $\xi = -1.5$ in Fig. 37, deeming it unreliable.

As shown in Fig. 36, the recoherence period appears to be about $N_{\text{AM}} = N_s$ for the weak beam intensity $N_B = 0.13 \times 10^{12}$ ppb, close to the linear decoherence scenario. As the beam intensity increases, the normalized recoherence period begins to rise, saturates around $N_B = 2.4 \times 10^{12}$ ppb, and then tends to decrease for higher-intensity beams in the measurements.

More specifically, Fig. 37 shows that the saturation number of protons per bunch, at which the normalized recoherence period saturates, depends on the chromaticity. Overall, the saturation number of protons per bunch increases as the chromaticity becomes higher, consistent with the simulation results in Fig. 31.

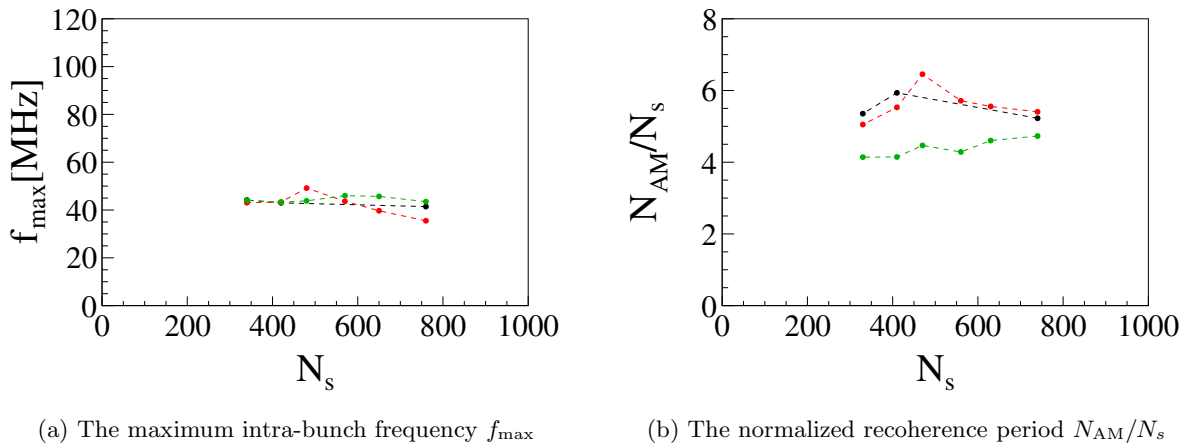


FIG. 35: The maximum intra-bunch frequency f_{\max} and the normalized recoherence period N_{AM}/N_s for the synchrotron period. Here, the black, red, and green denote the cases of $N_B = 2.4 \times 10^{12}$, 4.2×10^{12} , and 8.6×10^{12} ppb, respectively.

The measured decrease in the normalized recoherence period in the higher-intensity beams can be attributed to the same reason that explains the drop in normalized recoherence period for the case of $N_B = 8.6 \times 10^{12}$ ppb, as shown in Fig. 35b. The longitudinal emittances of the injection beam into the MR depend on the beam intensity, which enhances the bunching factor for $N_B = 8.6 \times 10^{12}$ ppb compared to $N_B = 4.2 \times 10^{12}$ ppb. This effect effectively weakens the space charge effect on the bunch, resulting in a shortening of the recoherence period compared to the recoherence period of intermediate-strength beams. As a result, the recoherence period is within the wider range of $4N_s < N_{AM} < 7N_s$ for the high-intensity and high-chromaticity beams in the measurements, unlike the simulations.

3. Chromaticity dependence

Finally, we observe the chromaticity dependence for the high-intensity beams by setting $\xi = -1.5, -8.0,$ and -12.5 with the fixed beam intensity $N_B = 4.2 \times 10^{12}$ ppb. Figure 38 shows the measured transverse bunch motion in the time domain. After those data are analyzed, the maximum intra-bunch frequency f_{\max} and the recoherence period N_{AM} can be determined to be $f_{\max} = 10$ MHz, $N_{AM} = 2200$, for $\xi = -1.5$; $f_{\max} = 51.9$ MHz, $N_{AM} = 2100$, for $\xi = -8.0$; and $f_{\max} = 81.3$ MHz, $N_{AM} = 1800$, for $\xi = -12.5$.

Figure 39 shows the maximum intra-bunch frequency f_{\max} dependence on the chromaticity. The black line represents the analytical result given by Eq. (157). The simulations shown in Fig. 39 are excellent in agreement with the measurements. Moreover, the maximum intra-bunch frequency follows the analytical result: $f_{\max} = 6.4|\xi|$ MHz (refer to Eq. (157) including the space charge effects, identical to Eq. (22) derived under the assumption of weak space charge effects). In the end, we find that the measurements confirm that space charge effects do not influence the relationship between the maximum intra-bunch frequency and chromaticity, as predicted by the simulations.

X. CONCLUSION

In this paper, we investigate the direct and indirect space charge effects on the intra-bunch motion across wider chromatic phase regions, by examining the dipole excitation in detail, using theoretical analysis, simulations, and experimental measurements. During the development of the simulation code, we clarify the limitations of applying the linear approximation to the space charge effects, namely that the beam size must be significantly smaller than the chamber radius. We find that neither the longitudinal nor the transverse impedance significantly influences the motions in the MR unless beam instability occurs.

Additionally, we reestablish the ABS theory to describe the space charge effects on the intra-bunch motion from a fundamental perspective and extend it to partially account for a more realistic Gaussian beam within a harmonic potential model. This theoretical framework allows us to better understand simulation features, including the extended recoherence time and the degeneration of head-tail modes in the high-intensity beams. The simulation code and

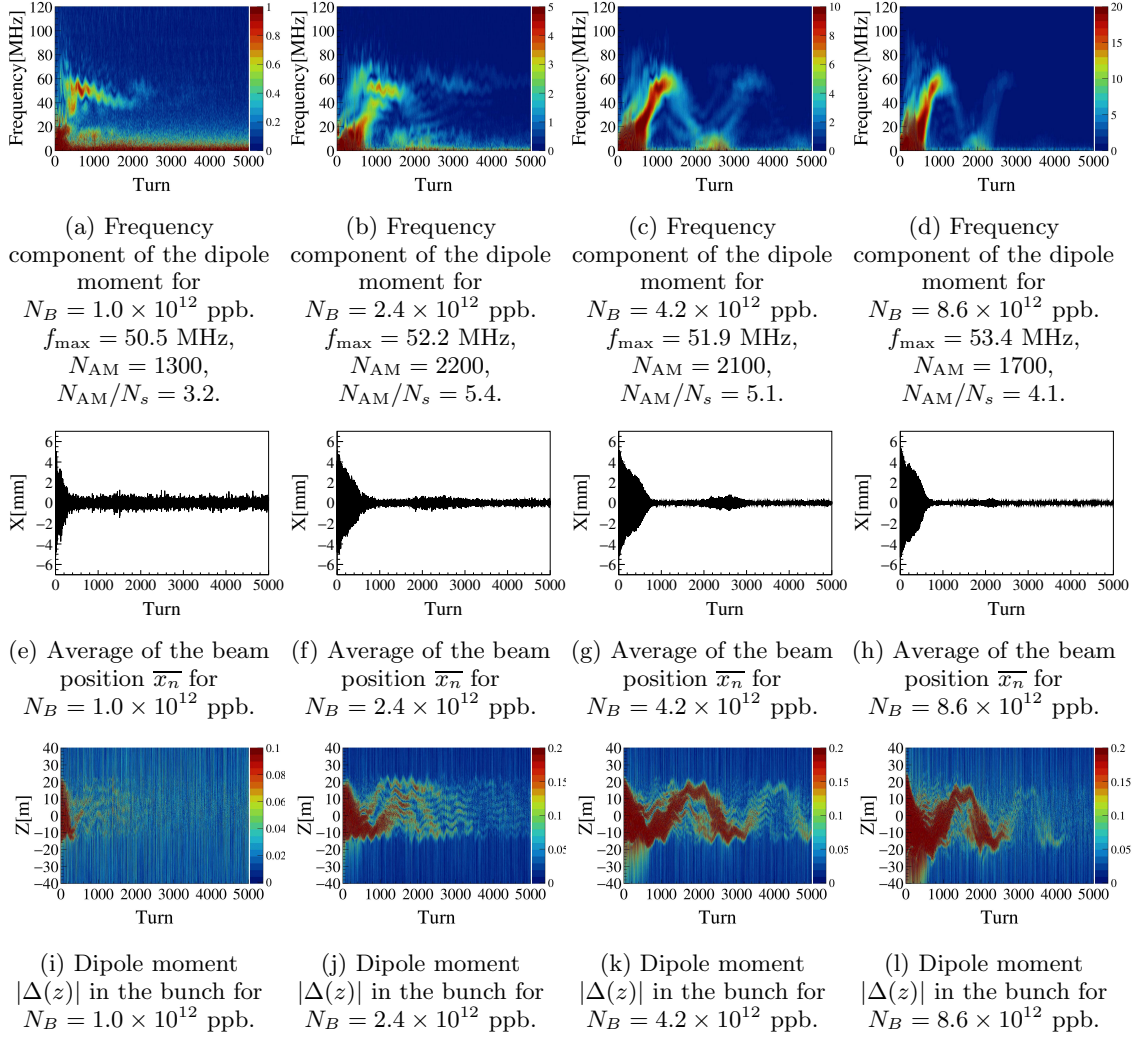


FIG. 36: Transverse bunch motion in the time domain for the beam intensity: $N_B = 1.0 \times 10^{12}$, 2.4×10^{12} , 4.2×10^{12} , and 8.6×10^{12} ppb with the chromaticity $\xi = -7.9$ and the RF voltage $V_{RF} = 263$ kV.

theory are compared in the weak space charge region, showing excellent agreement that supports the extension of the simulations to stronger space charge regions.

In the ABS model, the head-tail modes depend on the chromaticity setting. Higher head-tail modes are survived in regions of higher chromaticity, which aligns with experimental observations. However, in the simulations using a Gaussian beam with a harmonic potential, all head-tail modes are excited when the space charge effects are neglected. This discrepancy to the observation is resolved when the strong space charge effects are considered in the harmonic potential model, especially in higher chromaticity regions. Overall, the ABS model effectively describes simulations for Gaussian beams within a harmonic potential. As a result, we can understand the simulations based on the theory.

For the high-intensity beams, the recoherence time saturates, because the indirect space charge effects mitigate the degeneration of head-tail modes. In other words, the recoherence time becomes independent of beam intensity in higher chromaticity regions because the higher head-tail modes are excited and hard to degenerate.

Strictly speaking, it is challenging to precisely predict experimental outcomes because the longitudinal and transverse emittances of injection beams from upstream facilities vary with beam intensity. For instance, if the emittances are broadened from the outset, the space charge effects on intra-bunch motion are effectively mitigated during the storage mode in the ring, leading to a shortened recoherence time compared to the expected saturated value by the simulation. Nevertheless, the relationship between the maximum frequency in the bunch and the chromaticity remains unaffected by space charge effects.

In high-intensity proton rings such as the J-PARC MR, the space charge parameter is large and the chromatic phase has a broad range to suppress beam instability, so it is necessary to understand the basics of intra-bunch motion for

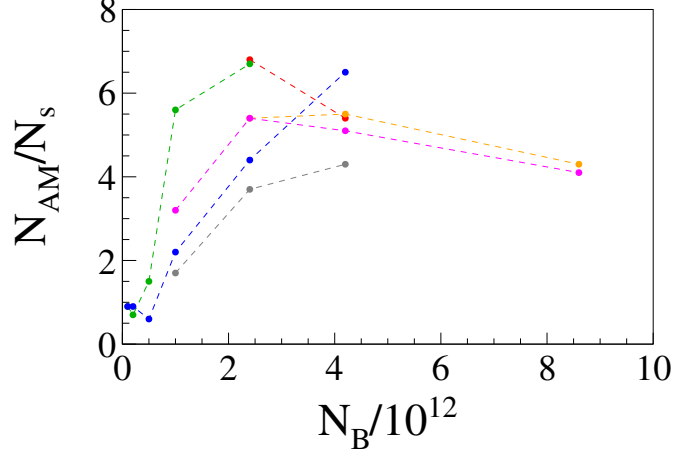


FIG. 37: The normalized recoherence period N_{AM}/N_s with several fixed chromaticities for different beam intensities. Here, the red, green, blue, orange, magenta, and gray denote the cases of $\xi = -1.5, -3.5, -5.5, -6.5, -8.0,$ and $-12.5,$ respectively.

stable operation. We find a phenomenon the high-frequency component rises gradually as the beam intensity becomes higher. If this characteristic is kept to the case when the beam instability occurs, it is quite beneficial to efficiently activate the IBFB. Therefore, the next goal is to use this simulation to investigate the mechanism of beam instability at high beam intensities to determine the optimal conditions for the IBFB when the beam instability is excited at the MR.

ACKNOWLEDGMENT

We would like to express special gratitude to Prof. T. Nakaya, who recommended the first author for research in accelerator science at the J-PARC as supervisor, for reading this paper critically and constructively. We thank Dr. A. Kobayashi and Mr. M. Okada from the monitor group for the adjustments to the BPM and data acquisition system and for many helpful discussions. The MR commissioning group, with Prof. Y. Sato and Dr. T. Yasui, is also acknowledged for coordinating beam conditions and the test schedule. We also thank Drs. F. Tamura, Y. Sugiyama, and H. Okita from the RF group for their help with RF matching conditions, and Prof. K. Ohmi for his involvement in setting the direction of this research at the early stage. Finally, we would like to thank all members of the J-PARC Center for their hospitality and help.

This work was supported by JSPS KAKENHI Grant Numbers JP23H05434 and JP18H05537, JST SPRING, Grant Number JPMJSP2110, and JST, the establishment of university fellowships towards the creation of science technology innovation, Grant Number JPMJFS2123.

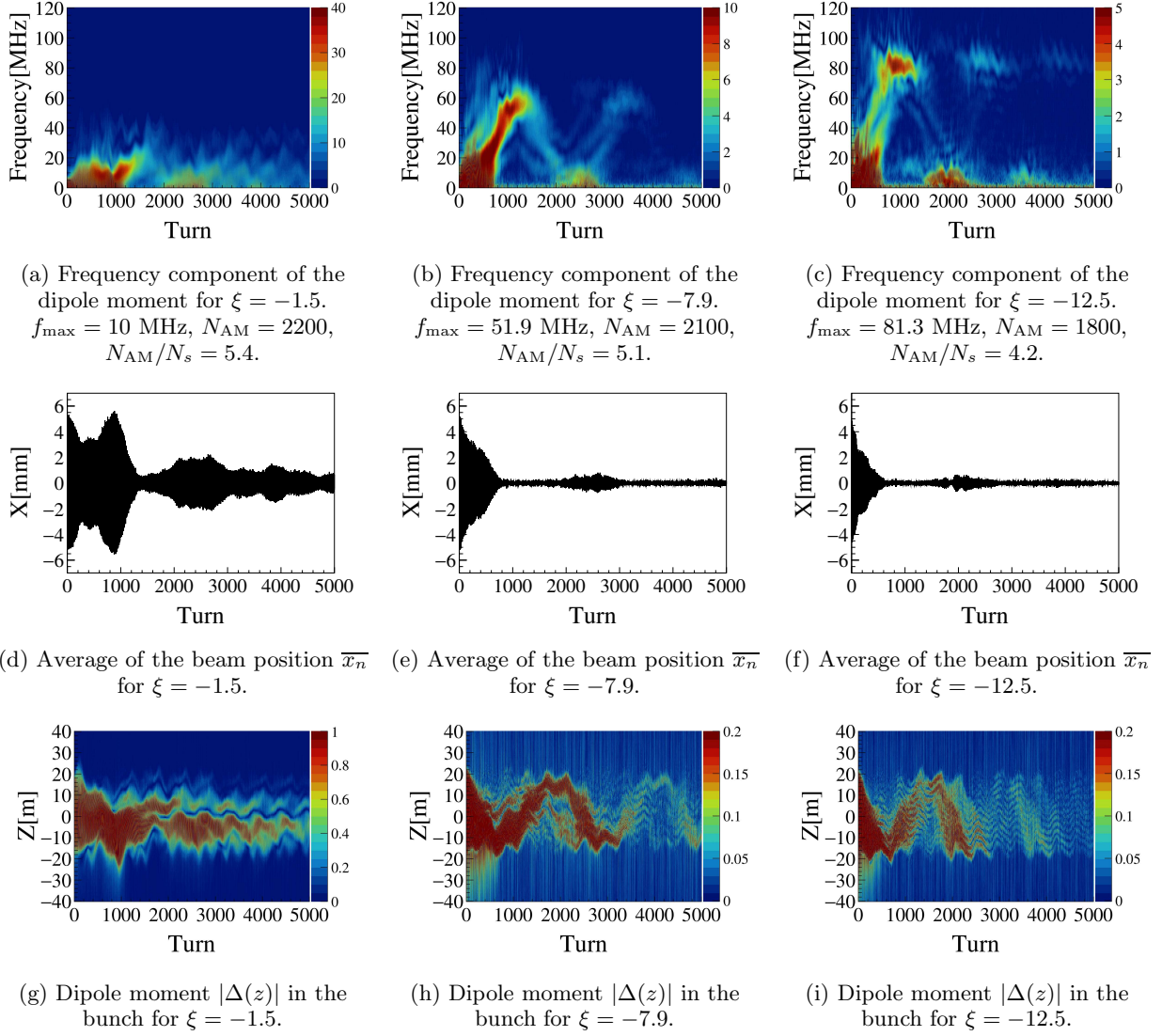


FIG. 38: Transverse bunch motion in the time domain for the chromaticity: $\xi = -1.5, -7.9$, and -12.5 with the beam intensity $N_B = 4.2 \times 10^{12}$ ppb and the RF voltage $V_{RF} = 263$ kV.

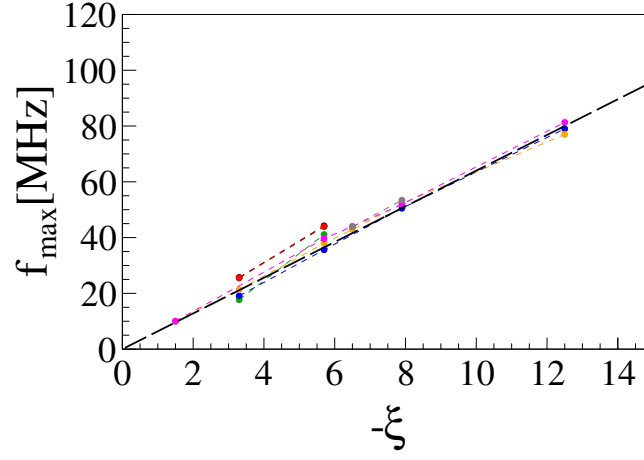


FIG. 39: The maximum intra-bunch frequency f_{\max} with several fixed beam intensities for different chromaticities. Here, the black, red, green, blue, orange, magenta, and gray denote the cases of $N_B = 1.3 \times 10^{11}$, 2.6×10^{11} , 5.2×10^{11} , 1.0×10^{12} , 2.4×10^{12} , 4.2×10^{12} , and 8.6×10^{12} ppb, respectively. The black dashed line is the result of Eq. (157).

Appendix A: Betatron phase advance in the linear decoherence scenario

Let us derive the horizontal centroid $\bar{x}(n, z)$ for the respective part in the bunch by solving Eqs. (79) and (114). The solutions are expressed as

$$z = z_0 \cos \theta, \quad (\text{A1})$$

$$\delta = \frac{2\pi\nu_s}{\eta C} z_0 \sin \theta = \text{sgn}(\eta) \frac{\sigma_\delta}{\sigma_z} z_0 \sin \theta, \quad (\text{A2})$$

with $\theta = 2\pi\nu_s n + \theta_0$, where z_0 is the longitudinal amplitude of the single particle, θ is the synchrotron phase and θ_0 is the initial synchrotron phase of it, the synchrotron tune $\nu_s = 0.0024$, the circumference of the ring $C = 1567.5$ m, the slippage factor $\eta = -0.0578$, $\sigma_z = 10$ m, and $\sigma_\delta = 2\pi\nu_s\sigma_z/|\eta|C = 0.17\%$ (same as Eq. (9)).

Accordingly, the betatron phase advance can be calculated as

$$\begin{aligned} \phi(n) &= 2\pi \int dn(\nu_\beta + \xi\delta) \\ &= 2\pi\nu_\beta n - \text{sgn}(\eta) \frac{\sigma_\delta}{\sigma_z} \xi z_0 (\cos \theta - \cos(\theta - 2\pi\nu_s n)) \\ &= 2\pi\nu_\beta n - \chi_\sigma \frac{z}{\sigma_z} (1 - \cos(2\pi\nu_s n)) + \text{sgn}(\eta) \chi_\sigma \frac{\delta}{\sigma_\delta} \sin(2\pi\nu_s n), \end{aligned} \quad (\text{A3})$$

where $\chi_\sigma = 2\pi\xi\sigma_z/\eta C$ (same as Eq. (20)) is the rms chromatic phase.

The distribution $\rho(\phi, n, z)$ of the betatron phase ϕ along the bunch can be expressed by using the phase space beam distribution $\rho_\delta(\delta)$ as follows,

$$\rho(\phi, n, z) = \int_{-\infty}^{\infty} d\delta \rho_\delta(\delta) \delta(f(\delta)), \quad (\text{A4})$$

where $\delta(x)$ is the delta function, and

$$f(\delta) = \phi - 2\pi\nu_\beta n + \chi_\sigma \frac{z}{\sigma_z} (1 - \cos(2\pi\nu_s n)) - \text{sgn}(\eta) \chi_\sigma \frac{\delta}{\sigma_\delta} \sin(2\pi\nu_s n). \quad (\text{A5})$$

Assuming that the longitudinal phase space $\rho_\delta(\delta)$ is always Gaussian distribution

$$\rho_\delta(\delta) = \frac{1}{\sqrt{2\pi}\sigma_\delta} \exp\left(-\frac{\delta^2}{2\sigma_\delta^2}\right), \quad (\text{A6})$$

the betatron phase distribution $\rho(\phi, n, z)$ is expressed as

$$\rho(\phi, n, z) = \int d\delta \frac{1}{\sqrt{2\pi}\sigma_\delta} \exp\left(-\frac{\delta^2}{2\sigma_\delta^2}\right) \delta(f(\delta)) = \frac{1}{\sqrt{2\pi}|\chi_\sigma \sin(2\pi\nu_s n)|} \exp\left(-\frac{\delta'^2}{2\sigma_\delta^2}\right), \quad (\text{A7})$$

where

$$\delta' = \text{sgn}(\eta) \sigma_\delta \left[\frac{\phi - 2\pi\nu_\beta n}{\chi_\sigma \sin(2\pi\nu_s n)} + \frac{z}{\sigma_z} \tan(\pi\nu_s n) \right]. \quad (\text{A8})$$

As a result, the horizontal centroid in the Gaussian bunch is described as

$$\begin{aligned} \bar{x}(n, z) &= \int_{-\infty}^{\infty} d\phi X_0 \exp(-i\phi) \rho(\phi, n, z) \\ &= X_0 \frac{1}{\sqrt{2\pi}|\chi_\sigma \sin(2\pi\nu_s n)|} \int_{-\infty}^{\infty} d\phi \exp\left[-i\phi - \frac{1}{2} \left(\frac{\phi - 2\pi\nu_\beta n}{\chi_\sigma \sin(2\pi\nu_s n)} + \frac{z}{\sigma_z} \tan(\pi\nu_s n) \right)^2\right] \\ &= X_0 \exp\left[-\frac{1}{2} \chi_\sigma^2 \sin^2(2\pi\nu_s n)\right] \exp\left[-i(2\pi\nu_\beta n - 2\chi_\sigma \sin^2(\pi\nu_s n) \frac{z}{\sigma_z})\right]. \end{aligned} \quad (\text{A9})$$

This result is identical to Eq.(3.13) in Ref. [46].

Appendix B: Series expansion of the electric field in the elliptical chamber

Let us derive the electric fields due to an elliptic uniform beam that represents the direct and indirect space charge contributions in Eqs. (37) and (38). The horizontal component of the electric field in Eq. (33) is simplified and expanded for small x , when the witness particles are on the horizontal axis ($y = 0$) as

$$E_x^0 = \frac{\lambda}{2\pi\epsilon_0} \frac{KS}{\pi W} \left(\frac{D}{C - C_s} + \frac{D}{C - \overline{C}_s} - \frac{Ck^2}{D + D_s} - \frac{Ck^2}{D + \overline{D}_s} \right) = \frac{\lambda}{2\pi\epsilon_0} (B_0 + B_1x + B_2x^2 + O(x^3)), \quad (\text{B1})$$

where

$$\begin{aligned} B_0 &= -\frac{Kk'}{\pi f} \left(\frac{1}{C_s} + \frac{1}{\overline{C}_s} \right), \\ B_1 &= -\frac{2K^2k'^2}{\pi^2 f^2} \left(\frac{1}{C_s^2} + \frac{1}{\overline{C}_s^2} \right) - \frac{2K^2k^2k'}{\pi^2 f^2} \left(\frac{1}{k' + D_s} + \frac{1}{k' + \overline{D}_s} \right), \\ B_2 &= -\frac{Kk'}{2\pi^3 f^3} (\pi^2 + 4K^2k^2 - 4K^2k'^2) \left(\frac{1}{C_s} + \frac{1}{\overline{C}_s} \right) - \frac{4K^3k'^3}{\pi^3 f^3} \left(\frac{1}{C_s^3} + \frac{1}{\overline{C}_s^3} \right), \end{aligned} \quad (\text{B2})$$

with $k' = \sqrt{1 - k^2}$. These coefficients B_0, B_1 , and B_2 are further expanded for small x_s and y_s as

$$\begin{aligned} B_0 &= B_{000}x_s^{-1} + B_{001}x_s + B_{002}x_s^3 + B_{010}x_s^{-3}y_s^2 + B_{011}x_s^{-1}y_s^2 + B_{012}x_sy_s^2 + O(x_s^5) + O(x_s^3y_s^2) + O(y_s^4), \\ B_1 &= B_{100}x_s^{-2} + B_{101} + B_{102}x_s^2 + B_{110}x_s^{-4}y_s^2 + B_{111}x_s^{-2}y_s^2 + B_{112}y_s^2 + O(x_s^4) + O(x_s^2y_s^2) + O(y_s^4), \\ B_2 &= B_{200}x_s^{-3} + B_{201}x_s^{-1} + B_{202}x_s + B_{210}x_s^{-5}y_s^2 + B_{211}x_s^{-3}y_s^2 + B_{212}x_s^{-1}y_s^2 + O(x_s^3) + O(x_sy_s^2) + O(y_s^4), \end{aligned} \quad (\text{B3})$$

whose coefficients are calculated as

$$\begin{aligned} B_{000} &= -1, \\ B_{001} &= \frac{1}{6f^2} \left(1 - \frac{4(1 - 2k^2)K^2}{\pi^2} \right), \\ B_{002} &= \frac{1}{3} \frac{1}{120f^4} \left(17 - \frac{40(1 - 2k^2)K^2}{\pi^2} - \frac{16(7 + 8k^2 - 8k^4)K^4}{\pi^4} \right), \\ B_{010} &= 1, \\ B_{011} &= 0, \\ B_{012} &= -\frac{1}{120f^4} \left(17 - \frac{40(1 - 2k^2)K^2}{\pi^2} - \frac{16(7 + 8k^2 - 8k^4)K^4}{\pi^4} \right), \\ B_{100} &= -1, \\ B_{101} &= \frac{1}{6f^2} \left(2 - \frac{4(2 - k^2)K^2}{\pi^2} \right), \\ B_{102} &= \frac{1}{120f^4} \left(8 - \frac{16(8 - 8k^2 - 7k^4)K^4}{\pi^4} \right), \\ B_{110} &= 3, \\ B_{111} &= 0, \\ B_{112} &= -\frac{1}{120f^4} \left(8 - \frac{16(8 - 8k^2 - 7k^4)K^4}{\pi^4} \right), \\ B_{200} &= -1, \\ B_{201} &= 0, \\ B_{202} &= \frac{1}{120f^4} \left(17 - \frac{40(1 - 2k^2)K^2}{\pi^2} - \frac{16(7 + 8k^2 - 8k^4)K^4}{\pi^4} \right), \\ B_{210} &= 6, \\ B_{211} &= 0, \\ B_{212} &= 0. \end{aligned} \quad (\text{B4})$$

Finally, the horizontal component of the electric field of Eq. (33) can be summarized as follows

$$\begin{aligned}
E_x^0 &= E_{x,DS}^0 + E_{x,im}^0 \\
&\simeq \frac{\lambda}{2\pi\epsilon_0} \left(B_{000} \frac{1}{x_s} + B_{100} \frac{x}{x_s^2} + B_{200} \frac{x^2}{x_s^3} + B_{010} \frac{1}{x_s^3} y_s^2 + B_{110} \frac{x}{x_s^4} y_s^2 + B_{210} \frac{x^2}{x_s^5} y_s^2 \right) \\
&+ \frac{\lambda}{2\pi\epsilon_0} (B_{001} x_s + B_{101} x + B_{002} x_s^3 + B_{012} x_s y_s^2 + B_{102} x_s^2 x + B_{112} y_s^2 x + B_{202} x_s x^2),
\end{aligned} \tag{B5}$$

where the first and second terms represent the direct space charge contribution from $E_{x,DS}^0$ and the indirect space charge contribution from $E_{x,im}^0$, respectively.

Appendix C: Longitudinal wake potential

As we have already seen in Sec. III, the recoherence time and synchrotron frequency are closely related. In accordance with it, the resistive wall impedance may deform the RF bucket, which can in turn lengthen the synchrotron period. In this section, we examine the possibility that the longitudinal resistive wall effect could modulate the recoherence time.

To take into account the nonlinearity of the RF acceleration to the longitudinal amplitude, Eq. (7) is replaced by

$$\delta_{n+1,i} = \delta_{n,i} - \frac{eV_{RF}}{\beta^2 E_0} \sin\left(\frac{2\pi h}{C} z_{n+1,i}\right) \frac{\Delta T}{T_0}. \tag{C1}$$

The MR, with a circumference of $C(=1567.5 \text{ m})$, utilizes SUS316L stainless steel cylindrical chambers with an inner radius of $h_C(=0.065 \text{ m})$ and a thickness of $d_w(=0.002 \text{ m})$. The longitudinal resistive wall wake is given by [47]

$$W_{L0}(s) = \frac{4cZ_0 C}{\pi h_C^2} \left(\frac{e^{-\frac{s}{s_0}}}{3} \cos \frac{\sqrt{3}s}{s_0} - \frac{\sqrt{2}}{\pi} \int_0^\infty dx \frac{x^2 e^{-x^2 \frac{s}{s_0}}}{x^6 + 8} \right), \quad \text{for } s > 0 \text{ m}, \tag{C2}$$

where $s_0 = (2h_C^2 \rho)^{1/3} = 250 \text{ } \mu\text{m}$.

The potential well distortion is excited by the wake potential as

$$W_{L0}(s) = \int_{-\infty}^\infty ds' W_{L0}(s-s') \rho_z(s'), \tag{C3}$$

where we assume a Gaussian beam as

$$\rho_z(z) = eN_B \frac{1}{\sqrt{2\pi}\sigma} e^{-\frac{z^2}{2\sigma^2}}. \tag{C4}$$

Figure 40 shows the longitudinal wake potential divided by the total charge of bunch : eN_B , in the case of $\sigma=2.72 \text{ m}$, which is used as the initial parameter in the simulation in this section.

To compromise this impedance with the space charge calculations in the code, we calculate the wake potential only on the mesh grid points in advance and subsequently interpolate it to estimate the kick on the witness particle located between the mesh grid points. The longitudinal kick $kick_z^{(k)}$ at the mesh grid point k is calculated as

$$kick_z^{(k)} = \sigma_\Delta \sum_j W_{L0}(z_j - z^{(k)}) \lambda^{(j)}, \tag{C5}$$

where the charge density $\lambda^{(j)}$ of j -th segment is given by Eq. (17).

Subsequently, the longitudinal kick $kick_{z,i}$ on i -th macroparticle between k -th and $k+1$ -th grid points are calculated as

$$kick_{z,i} = \left(1 - \frac{z_i - z^{(k)}}{\sigma_\Delta} \right) kick_z^{(k)} + \frac{z_i - z^{(k)}}{\sigma_\Delta} kick_z^{(k+1)}. \tag{C6}$$

Finally, the longitudinal kick at each time step is implemented into the code as

$$\Delta\delta_i = -\frac{1}{E_0} kick_{z,i} \frac{\Delta T}{T_0}. \tag{C7}$$

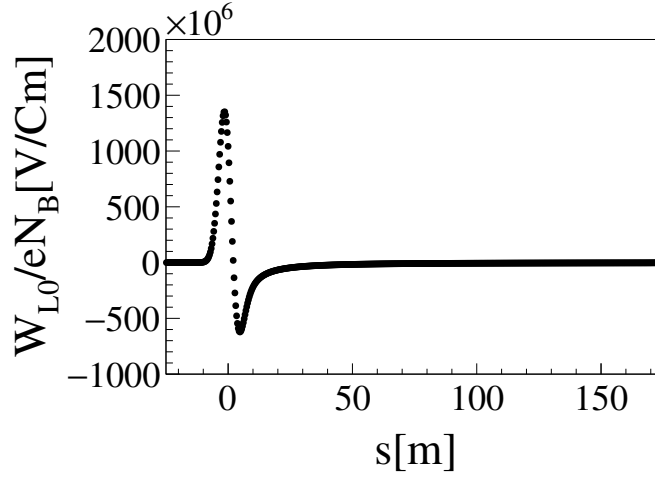


FIG. 40: Longitudinal resistive wall wake potential divided by the total charge of bunch for $\sigma=2.72$ m.

Notice that the long-range wake effect is neglected in this calculation.

On the other hand, the Hamiltonian formalism theoretically provides the deformation of synchrotron tune through the potential well distortion as follows

$$\nu_s(H_0) = C \left[\oint \frac{d\phi}{2\sqrt{H_0 - U(\phi)}} \right]^{-1}, \quad (\text{C8})$$

where

$$H_0 = \frac{1}{2} \left(\frac{2\pi h\eta}{C} \right)^2 \delta_i^2 + U(\phi). \quad (\text{C9})$$

Here, the potential $U(\phi)$ is assumed to be fixed for the given beam distribution as

$$U(\phi) = \frac{2\pi h\eta e V_{\text{RF}}}{C^2 E_0} (\cos \phi - 1) - \frac{2\pi h\eta}{C^2 E_0} \int_{-\infty}^{\phi} d\phi'' \int_{-\infty}^{\infty} d\phi' W_{\text{L0}}(\phi' - \phi'') \lambda(\phi'), \quad (\text{C10})$$

neglecting the deformation effect on the bunch shape due to the wake, where $\phi = 2\pi h z / C$ is the longitudinal phase and $\lambda(\phi)$ is charge density.

Figure 41 shows the theoretical and simulation results only with the longitudinal wake potential with $N_B = 3 \times 10^{14}$ ppb for different particle energy represented by H_0 . The theoretical and the simulations are in good agreement. The outcome demonstrates that this synchrotron tune distribution is confined in $0.002 < \nu_s < 0.00245$.

On the contrary, we find a significant discrepancy between the theoretical/simulation results only dealing with the wakefields, and the experimental one in the MR : $\nu_s \approx 0.0005$ which is obtained by assuming the recoherence time is determined solely by the synchrotron tune. Finally, we conclude that the observed longitudinal resistive wall impedance alone cannot explain the lengthened recoherence time, even when the amplitude modulation period due to the wake effect is taken into consideration [40].

Appendix D: Consistency check with the linear decoherence scenario

Linear decoherence scenario described in Sec. III is useful for benchmark tests of our code. Let us investigate the time evolution of the transverse oscillation amplitude of the centroid, of the transverse dipole moment, and of the intra-bunch frequency within the linear approximation of the RF bucket around the bunch.

The transverse amplitude (Courant-Snyder invariant) is calculated as

$$\overline{A_n} = \sqrt{\overline{x_n^2} + \beta_x^2 \overline{x_n'^2}}, \quad (\text{D1})$$

by assuming the Twiss parameter γ is zero for simplicity, where $\overline{x_n'} = \sum_i x_{n,i}' / N_{\text{particle}}$.

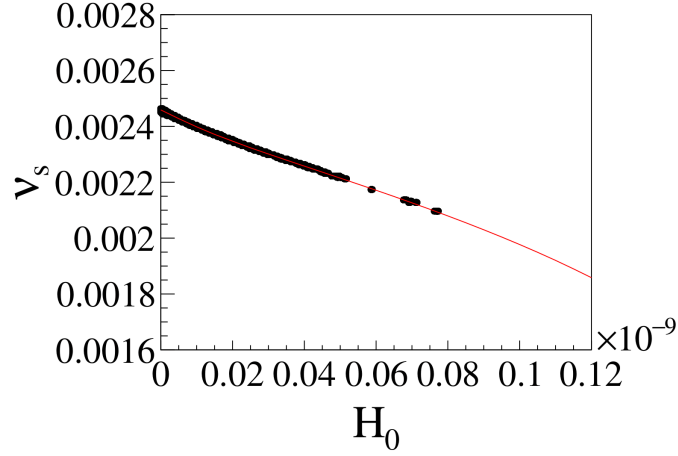


FIG. 41: Theoretical result of synchrotron tune deviation due to the potential $U'(\phi)$ (red line) and the simulation results (point) in the case of $N_B = 3 \times 10^{14}$ ppb and $\sigma_z = 2.72$ m.

Tracking simulations are performed under the RF voltages : $V_{\text{RF}} = 110, 263,$ and 400 kV and the fixed chromaticity $\xi = -2$. Figure 42 compares the theoretical result by Eq. (25) of transverse amplitude \bar{A}_n for each turn (Fig. 42a) with the simulations (Fig. 42b), where the blue, black, and red lines show the cases of $V_{\text{RF}} = 110, 263,$ and 400 kV, respectively. Amplitude modulation occurs synchronously with the synchrotron period of $N_s = 330$ (red), 410 (black), and 630 (blue) turns, determined by the RF voltages.

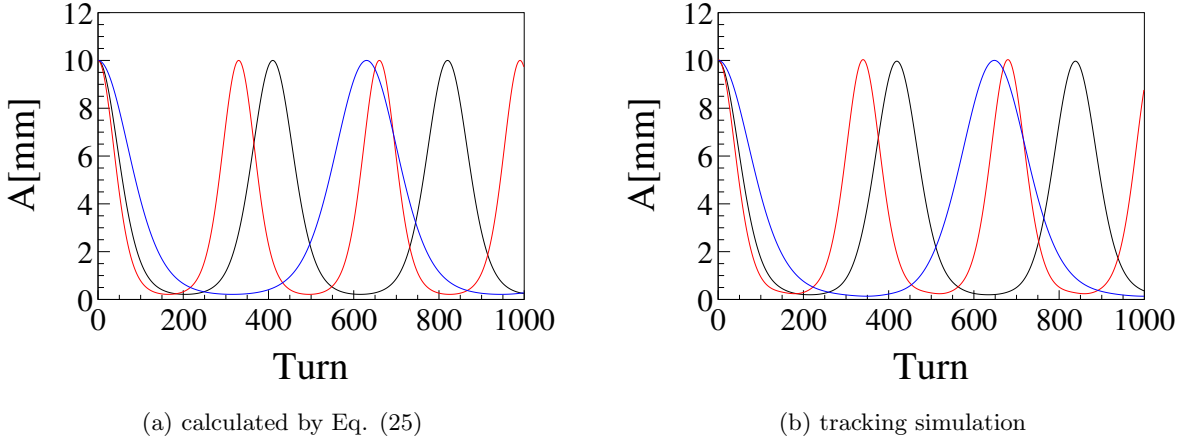


FIG. 42: Transverse amplitudes of the bunch oscillation calculated by Eq. (25) and tracking simulations for $V_{\text{RF}} = 110$ kV (blue), $V_{\text{RF}} = 263$ kV (black), and $V_{\text{RF}} = 400$ kV (red).

For various chromaticity conditions $\xi = -1, -2, -3,$ and -8 with fixed $V_{\text{RF}} = 263$ kV, tracking simulations are performed and compared to the theoretical result (Eq. (25)). Figures 43a and 43b show the theoretical and the simulation results, respectively, where the black, red, blue, and green represent the result for $\xi = -1, -2, -3,$ and -8 , respectively. The simulations reproduce the theoretical results with great accuracy and demonstrate the reliability of our code. Notice that the decoherence becomes more clearly identified as the chromaticity increases in the negative direction.

Now, let us observe the frequency component of the bunch per turn after Fourier transforming the dipole moment for each segment. Figures 44 and 45 represent the simulations illustrating the dipole moments within the bunch and the Fourier components during the beam's circulation in the ring. As the chromaticity increases, the amplitude modulation is suppressed, with the intra-bunch frequency enhanced, which aligns well with theoretical expectations (Eqs. (19) and (21)).

More closely, let us analyze the maximum intra-bunch frequency f_{max} against the chromaticity. As illustrated in

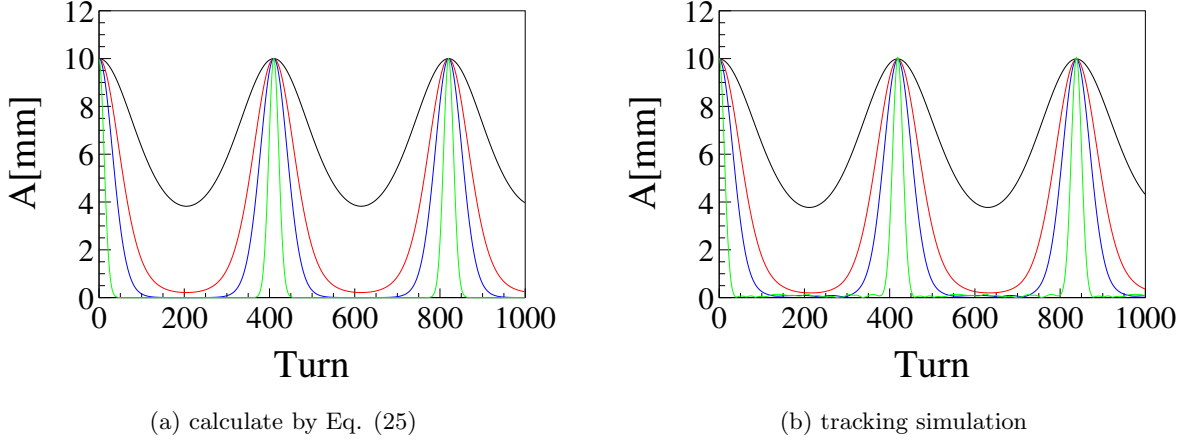


FIG. 43: Transverse amplitudes of the bunch oscillation calculated by Eq. (25) and tracking simulations for $\xi = -1$ (black), $\xi = -2$ (red), $\xi = -3$ (blue), and $\xi = -8$ (green).

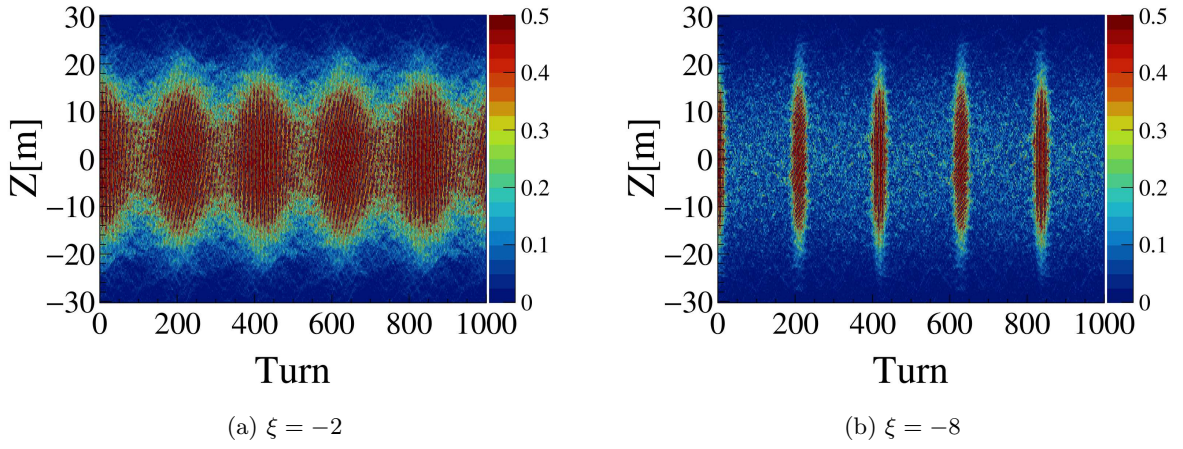


FIG. 44: The dipole moment $|\Delta^{(k)}\sigma_{\Delta}/q|$ in the bunch by the tracking simulations.

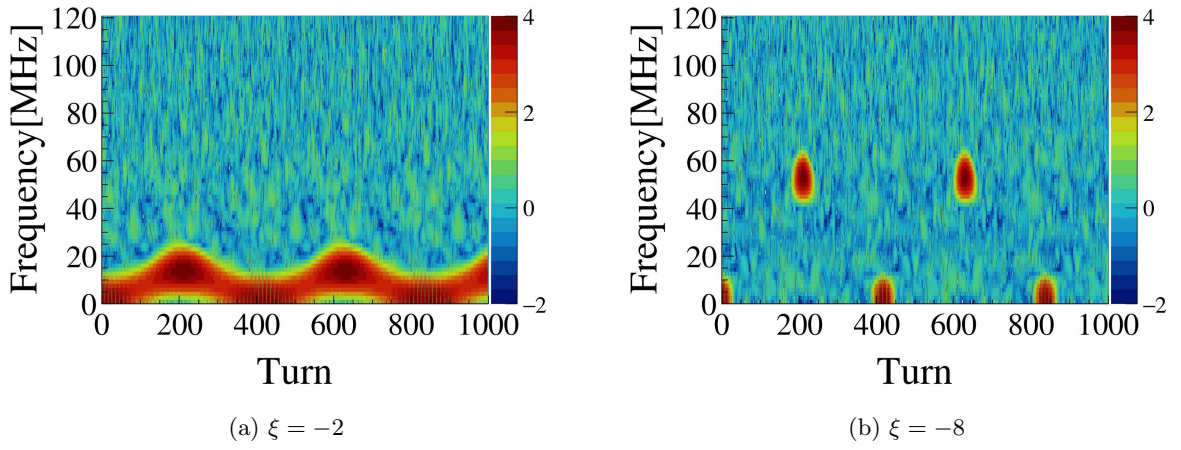


FIG. 45: Frequency components of the dipole moment in the bunch by the tracking simulations.

Fig. 46, the simulation's maximum intra-bunch frequency f_{\max} is in good agreement with the theoretical result by

Eq. (22), showcasing a linear response of the maximum intra-bunch frequency to the chromaticity ξ when excluding the impedance and space charge effects.

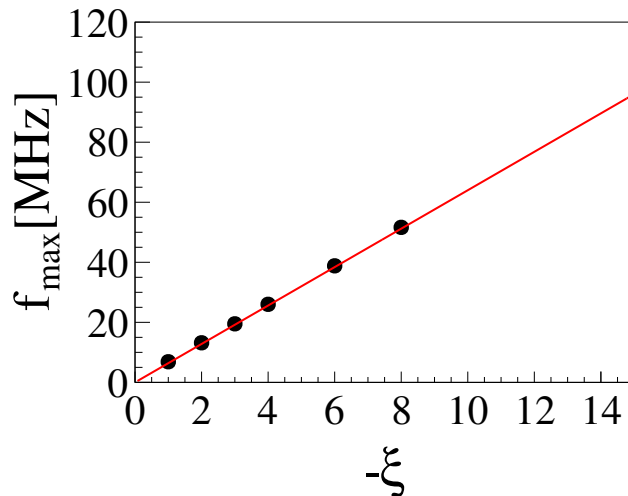


FIG. 46: The simulations (dots) and the theoretical results by Eq. (22) (red line) of the maximum intra-bunch frequency f_{\max} for each chromaticity condition.

Appendix E: Validity of simulation parameters

The critical parameters in our code dealing with the space charge effects are the number of macroparticles N_{particle} , the advance time per step relative to the revolution time $\Delta T/T_0$, and the longitudinal mesh size σ_{Δ} . In this section, the required conditions to get reliable simulations are investigated by scanning these three parameters with fixed $\xi = -12.5$ and $N_B = 8.6 \times 10^{12}$ ppb, where the constant wake $W_{T1} = 4 \times 10^{12}$ V/Cm is adopted to streamline the calculation efficiency just for this purpose. This chromaticity is chosen as the worst condition in our simulation because a sufficiently tiny mesh size is necessary to obtain reliable simulation results for higher chromaticity.

Figures 47, 48a, and 49 represent $\overline{A_n}$ by Eq. (D1) (the average transverse amplitudes of all macroparticles) on a turn-by-turn basis in the following cases : (1) scanning N_{particle} with $T_0/\Delta T = 100$ and $\sigma_{\Delta} = 0.17$ m fixed, (2) scanning $T_0/\Delta T$ with $N_{\text{particle}} = 50000$ and $\sigma_{\Delta} = 0.17$ m fixed, and (3) scanning σ_{Δ} with $N_{\text{particle}} = 50000$ and $T_0/\Delta T = 100$ fixed.

The areas marked as \mathcal{A} in Fig. 47, \mathcal{B} in Fig. 48a, and \mathcal{C} in Fig. 49, respectively, illustrate the modulation of the transverse amplitudes caused by the space charge effects, characterizing the intra-bunch motion. The simulations provide a sufficient number of N_{particle} , a sufficiently small step size ΔT , and a sufficiently fine mesh size σ_{Δ} to accurately reproduce the phenomena. Figures 47, 48, and 49 seem to require the condition that $N_{\text{particle}} > 5000$, $T_0/\Delta T > 85$, and $C/(h\sigma_{\Delta}) > 512$ to excite the modulation of the transverse amplitudes correctly, because we observe the irregular reductions in the transverse amplitude at $T_0/\Delta T = 14, 17, 21, 42, 43$, and 85 , as shown in Fig. 48a.

Figure 48b illustrates the horizontal rms beam size σ_x as a function of $T_0/\Delta T$. We find that the irregular beam size expansion occurs in Fig. 48b under the same conditions depicted in Fig. 48a. This supports the conclusion that the irregular transverse amplitude reduction in Fig. 48a is caused by the beam losses at $T_0/\Delta T = 14, 17, 21, 42, 43$, and 85 , resulting from collisions of the macroparticles with the horizontal chamber boundary.

Accordingly, we examined the conditions under which the transverse amplitudes and the beam sizes remain stable up to $T_0/\Delta T = 300$. This analysis determined that $T_0/\Delta T > 85$ is the necessary condition for stability.

After all conditions are taken into consideration, we select $N_{\text{particle}} = 50000$, $\Delta T = T_0/100$, and $\sigma_{\Delta} = 0.17$ m as the suitable parameter set in the simulations with space charge effects.

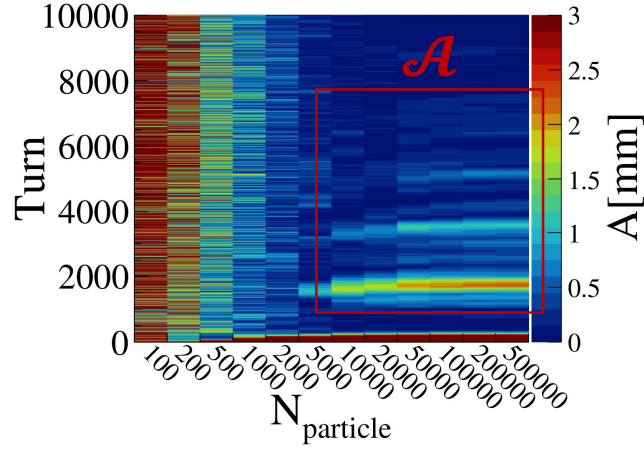


FIG. 47: Transverse amplitude $\overline{A_n}$ scanned by varying the number of macroparticles N_{particle} .

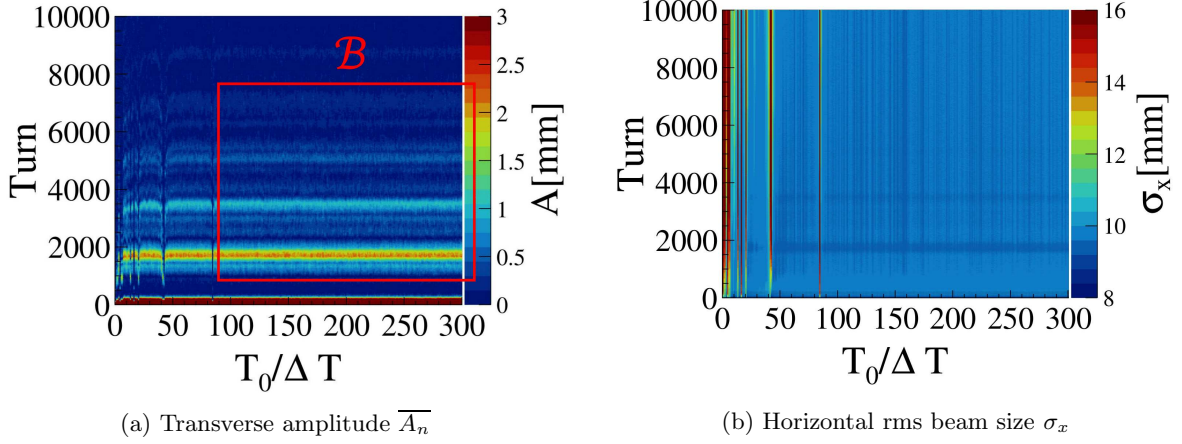


FIG. 48: The result of tracking simulation scanned by varying time steps relative to the revolution time $T_0/\Delta T$.

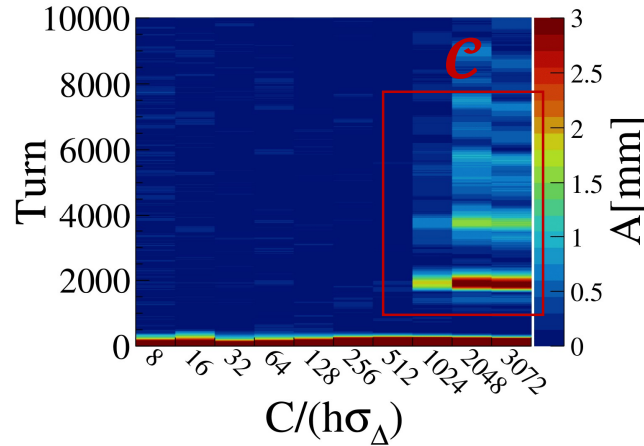


FIG. 49: Transverse amplitude $\overline{A_n}$ with constant wake by varying the size of the mesh that divides the bunch longitudinally as $C/(h\sigma_\Delta)$.

-
- [1] S. Igarashi, et al. Accelerator design for 1.3 MW beam power operation of the J-PARC Main Ring. *Progress of Theoretical and Experimental Physics*, Vol. 2021, No. 3, p. 033G01, 2021.
- [2] T. Koseki, et al. Beam commissioning and operation of the J-PARC main ring synchrotron. *Progress of Theoretical and Experimental Physics*, Vol. 2012, No. 1, p. 02B004, 2012.
- [3] S. Igarashi, et al. High-power beam operation at J-PARC. In *Proceedings of the 61st ICFA Advanced Beam Dynamics Workshop on High-Intensity and High-Brightness Hadron Beams*, pp. 147–152, Daejeon, Korea, 2018.
- [4] T. Koseki, et al. Upgrade plan of J-PARC MR-toward 1.3 MW beam power. In *Proceedings of the 9th International Particle Accelerator Conference*, pp. 966–969, Vancouver, BC, Canada, 2018.
- [5] T. Yasui. J-PARC MR operation with the high repetition rate upgrade. In *Proceedings of the 14th International Particle Accelerator Conference*, pp. 1294–1298, Venice, Italy, 2023.
- [6] T. Yasui, S. Igarashi, Y. Sato, and H. Hotchi. First Result of the High Repetition Operation in J-PARC MR. In *Proceedings of the 23rd International Workshop on Neutrinos from Accelerators*, Vol. 8, p. 23, Salt Lake City, UT, USA, 2023.
- [7] K. Abe, et al. Indication of electron neutrino appearance from an accelerator-produced off-axis muon neutrino beam. *Physical Review Letters*, Vol. 107, No. 4, p. 041801, 2011.
- [8] K. Abe, et al. Observation of electron neutrino appearance in a muon neutrino beam. *Physical Review Letters*, Vol. 112, No. 6, p. 061802, 2014.
- [9] K. Abe, et al. Constraint on the matter-antimatter symmetry-violating phase in neutrino oscillations. *Nature*, Vol. 580, No. 7803, pp. 339–344, 2020.
- [10] K. Abe, et al. Updated T2K measurements of muon neutrino and antineutrino disappearance using 3.6×10^{21} protons on target. *Physical Review D*, Vol. 108, No. 7, p. 072011, 2023.
- [11] K. Abe, et al. Hyper-Kamiokande design report. 2018.
- [12] A. W. Chao. *Physics of Collective Beam Instabilities in High Energy Accelerators*. John Wiley & Sons, Inc., New York, 1993.
- [13] K. Y. Ng. *Physics of Intensity Dependent Beam Instabilities*. World Scientific, Singapore, 2002.
- [14] M. Blaskiewicz. Fast head-tail instability with space charge. *Physical Review Special Topics-Accelerators and Beams*, Vol. 1, No. 4, p. 044201, 1998.
- [15] Y. H. Chin. Analysis of transverse instabilities observed at J-PARC MR and their suppression using feedback systems. In *Proceedings of the 25th North American Particle Accelerator Conference*, pp. 27–31, Pasadena, CA, USA, 2013.
- [16] O. Konstantinova, Y. H. Chin, Y. Kurimoto, T. Obina, M. Okada, K. Takata, M. Tobiyama, T. Toyama, and Y. Shobuda. Bunch by bunch intra-bunch feedback system for curing transverse beam instabilities at the J-PARC MR. In *Proceedings of the 4th International Particle Accelerator Conference*, pp. 1739–1741, Shanghai, China, 2013.
- [17] K. Nakamura, T. Toyama, M. Okada, M. Tobiyama, Y. H. Chin, T. Obina, T. Koseki, and Y. Shobuda. Intra-bunch feedback system for the J-PARC main ring. In *Proceedings of the 5th International Particle Accelerator Conference*, pp. 2786–2788, Dresden, Germany, 2014.
- [18] K. Nakamura, Makoto T., T. Toyama, M. Okada, Y. H. Chin, T. Obina, T. Koseki, H. Kuboki, and Y. Shobuda. Performance evaluation of the intra-bunch feedback system at J-PARC main ring. In *Proceedings of the 3rd International Beam Instrumentation Conference*, pp. 727–730, Monterey, CA, USA, 2014.
- [19] Y. Kurimoto, M. Tobiyama, Y. H. Chin, T. Obina, and T. Toyama. The bunch by bunch feedback system in J-PARC Main Ring. In *Proceedings of the 10th European Workshop on Beam Diagnostics and Instrumentation for Particle Accelerators*, pp. 482–484, Hamburg, Germany, 2011.
- [20] T. Toyama, M. Okada, and A. Kobayashi. Analysis and upgrade plan of the transverse intra-bunch feedback system in the J-PARC MR. In *Proceedings of the 16th Annual Meeting of the Particle Accelerator Society of Japan*, pp. 1130–1133, 2019, (Japanese).
- [21] T. Toyama, A. Kobayashi, T. Nakamura, M. Okada, Y. Shobuda, and M. Tobiyama. Beam instability issue and transverse feedback system in the MR of J-PARC. In *Proceedings of the 64th ICFA Advanced Beam Dynamics Workshop on High-Intensity and High-Brightness Hadron Beams*, pp. 208–212, Batavia, IL, USA, 2022.
- [22] N. Yoshimura, T. Toyama, A. Kobayashi, T. Nakamura, M. Okada, Y. Shobuda, and T. Nakaya. Evaluation for updating the intra-bunch feedback at J-PARC Main Ring. In *Proceedings of the 19th Annual Meeting of the Particle Accelerator Society of Japan*, pp. 936–941, 2022, (Japanese).
- [23] T. Nakamura, K. Satou, T. Toyama, M. Okada, A. Kobayashi, I. Yamada, and Y. Shobuda. Development of new RFSoc based intra-bunch transverse feedback system at J-PARC MR : design and initial evaluation. In *Proceedings of the 21th Annual Meeting of the Particle Accelerator Society of Japan*, pp. 881–886, 2024, (Japanese).
- [24] T. Nakamura, S. Daté, K. Kobayashi, and T. Ohshima. Transverse bunch-by-bunch feedback system for the SPring-8 storage ring. In *Proceedings of the 9th European Particle Accelerator Conference*, pp. 2649–2651, Lucerne, Switzerland, 2004.
- [25] T. Nakamura. Transverse and Longitudinal Bunch-by-Bunch Feedback for Storage Rings. In *Proceedings of the 9th International Particle Accelerator Conference*, pp. 1198–1203, Vancouver, BC, Canada, 2018.
- [26] I. Karpov, V. Kornilov, and O. Boine-Frankenheim. Early transverse decoherence of bunches with space charge. Vol. 19, No. 12, p. 124201, 2016.
- [27] V. Kornilov and O. Boine-Frankenheim. Head-tail instability and Landau damping in bunches with space charge. *Physical Review Special Topics-Accelerators and Beams*, Vol. 13, No. 11, p. 114201, 2010.

- [28] R. Singh, O. Boine-Frankenheim, O. Chorniy, P. Forck, R. Haseitl, W. Kaufmann, P. Kowina, K. Lang, and T. Weiland. Interpretation of transverse tune spectra in a heavy-ion synchrotron at high intensities. *Physical Review Special Topics-Accelerators and Beams*, Vol. 16, No. 3, p. 034201, 2013.
- [29] V. Kornilov and O. Boine-Frankenheim. Simulation studies & code validation for the head-tail instability with space charge. In *Proceedings of the 10th International Computational Accelerator Physics Conference*, Vol. San Francisco, CA, USA, pp. 58–63, 2010.
- [30] V. Kornilov and O. Boine-Frankenheim. Transverse decoherence and coherent spectra in long bunches with space charge. *Physical Review Special Topics-Accelerators and Beams*, Vol. 15, No. 11, p. 114201, 2012.
- [31] O. Boine-Frankenheim and V. Kornilov. Transverse Schottky noise spectrum for bunches with space charge. *Physical Review Special Topics-Accelerators and Beams*, Vol. 12, No. 11, p. 114201, 2009.
- [32] O. Boine-Frankenheim and V. Kornilov. Implementation and validation of space charge and impedance kicks in the code PATRIC for studies of transverse coherent instabilities in FAIR rings. In *Proceedings of the 9th International Computational Accelerator Physics Conference*, pp. 267–270, Chamonix, France, 2006.
- [33] G. L. Sabbi. Simulation of single-bunch collective effects in LEP by linear expansion of the distribution moments. Technical Report CERN SL/95-25(AP), 1995.
- [34] G. L. Sabbi. TRISIM user’s guide. Technical Report CERN SL/94-73(AP), 1994.
- [35] R. E. Meller, A. W. Chao, J. M. Peterson, S. G. Peggs, and M. Furman. Decoherence of kicked beams. Technical Report SSC-N-360, 1987.
- [36] I. M. Kapchinskij and V. V. Vladimirskij. Limitations of proton beam current in a strong focusing linear accelerator associated with the beam space charge. In *Proceedings of the International Conference on High Energy Accelerators and Instrumentation*, p. 274, 1959.
- [37] B. Zotter. Tune shifts of excentric beams in elliptic vacuum chambers. *IEEE Transactions on Nuclear Science*, Vol. 22, No. 3, pp. 1451–1455, 1975.
- [38] M. Abramowitz and I. A. Stegun. *Handbook of Mathematical Functions With Formulas, Graphs, and Mathematical Tables*. Dover, New York, 1974.
- [39] L. J. Laslett. On intensity limitations imposed by transverse space-charge effects in circular particle accelerators. In *Proceedings of the 1963 Summer Study on Storage Rings, Accelerators and Experimentation at Super-High Energies, eConf C630610*, pp. 324–367, 1963.
- [40] N. Yoshimura, T. Toyama, Y. Shobuda, T. Nakamura, K. Omi, A. Kobayashi, M. Okada, Y. Sato, and T. Nakaya. Study on simulation code for transverse instabilities for the J-PARC MR. In *Proceedings of the 20th Annual Meeting of the Particle Accelerator Society of Japan*, pp. 260–264, 2023, (Japanese).
- [41] Y. Shobuda and K. Yokoya. Resistive wall impedance and tune shift for a chamber with a finite thickness. *Physical Review E*, Vol. 66, No. 5, p. 056501, 2002.
- [42] K. Yokoya. Resistive wall impedance of beam pipes of general cross section. *Particle Accelerators*, Vol. 41, pp. 221–248, 1993.
- [43] R. L. Gluckstern, J. van Zeijts, and B. Zotter. Coupling impedance of beam pipes of general cross section. *Physical Review E*, Vol. 47, No. 1, p. 656, 1993.
- [44] A. Kobayashi, T. Toyama, Y. Sato, S. Igarashi, M. Yoshii, and Y. Sugiyama. The investigation on the time structure of the wake field at the J-PARC MR. In *Proceedings of the 16th Annual Meeting of the Particle Accelerator Society of Japan*, pp. 223–227, 2019, (Japanese).
- [45] Y. Shobuda, Y. H. Chin, K. Takata, T. Toyama, and K. Nakamura. Triangle and concave pentagon electrodes for an improved broadband frequency response of stripline beam position monitors. *Physical Review Accelerators and Beams*, Vol. 19, No. 2, p. 021003, 2016.
- [46] I. Karpov. *Damping of coherent oscillations in intense ion beams*. PhD thesis, Darmstadt, Tech. U., 2017.
- [47] K. L. F. Bane and M. Sands. The short-range resistive wall wakefields. Technical Report SLAC/AP-87, Stanford Linear Accelerator Center, Stanford University, Stanford, CA, USA, 1991.